Title	Study on dynamical spin injection, transport and conversion in germanium and graphene
Author(s)	Dushenko, Sergey
Citation	大阪大学, 2016, 博士論文
Version Type	VoR
URL	https://doi.org/10.18910/55885
rights	
Note	

Study on dynamical spin injection, transport and conversion in germanium and graphene

SERGEY DUSHENKO

MARCH 2016

Study on dynamical spin injection, transport and conversion in germanium and graphene

A dissertation submitted to
THE GRADUATE SCHOOL OF ENGINEERING SCIENCE
OSAKA UNIVERSITY
in partial fulfillment of the requirements for the degree of
DOCTOR OF PHILOSOPHY IN SCIENCE

BY

SERGEY DUSHENKO

MARCH 2016

Abstract of the dissertation

Study on dynamical spin injection, transport and conversion in germanium and graphene

by

Sergey Dushenko

In this dissertation author focused on the spintronics study of the two elements from Group 14 of periodic table: carbon (C), in the form of graphene, and germanium (Ge). Graphene attracts large attention from spintronics community due to its long spin diffusion length and novel two dimensional structure with massless Dirac fermions, in contrast to usual bulk materials. Ge, on the other hand, has the same crystal structure as silicon, but has mobility ten times higher. While spin transport was established in silicon, non-local spin transport in Ge at room temperature was still unachievable goal for spintronics researchers prior to the author's study.

In introductory Chapter 1 the author gave short overview of the spintronics topics related to the research presented in the dissertation. However, in the beginning of the chapters 2-4 the author shortly reintroduced and discussed situation in the topics directly related to the results presented in the chapters.

In Chapter 2 the author reported the first experimental demonstration of room-temperature spin transport in n-type Ge epilayers grown on a Si(001) substrate. By utilizing spin pumping under ferromagnetic resonance, which inherently endows a spin battery function for semiconductors connected with a ferromagnet, a pure spin current was generated in the n-Ge at room temperature. The pure spin current was detected by using the inverse spin Hall effect of either a Pt or Pd electrode on top of n-Ge. From a theoretical model that included a geometrical contribution the spin diffusion length in n-Ge at room temperature was estimated to be 660 nm. Moreover, the spin relaxation time decreased with increasing temperature, in agreement with a recently proposed theory of donor-driven spin relaxation in multivalley semiconductors.

The small spin-orbit interaction of carbon atoms in graphene promises a long spin diffusion length and potential to create a spin field-effect transistor. However, for this reason, graphene was largely overlooked as a possible spin-charge conversion material. In Chapter 3 the author reported electric gate tuning of the spin-charge conversion voltage signal in a single-layer graphene. Using spin pumping from yttrium iron garnet ferrimagnetic insulator and ionic liquid top gate the author determined that the inverse spin Hall effect is the dominant spin-charge conversion mechanism in a single-layer graphene. From the gate dependence of the electromotive force the author showed dominance of the intrinsic over Rashba spin-orbit interaction, and estimated its strength to be ~1 meV: a long-standing question in graphene-related research.

To pursue goal of temperature investigation of the spin-charge conversion in the yttrium iron garnet/single-layer graphene system, the author first studied temperature behavior of the spin pumping. In Chapter 4, the author presented an analysis of yttrium iron garnet-based systems, highly exploited in spin pumping experiments, and demonstrated proper normalization procedure for the inverse spin Hall effect in such systems. The author explained the discrepancy between experiment and theory recently observed in spin pumping experiments. Thus, the author’s result finally allowed for quantitative analysis of the inverse spin Hall effect in various yttrium iron garnet-based experiments, including temperature dependent measurements.

Table of contents

Chapter 1

1.1 Abstract

In introductory Chapter 1 the author gave short overview of the spintronics topics related to the research presented in the dissertation.

1.2 Spintronics

In 1922 experiment of O. Stern and W. Gerlach, together with the spin concept and theory from W. Pauli and P. Dirac a few years later (and contribution from many other excellent scientists), a new field of science—spintronics was created. Spintronics uses angular momentum of the carriers—spin, rather than their charge (in contrast to electronics where charge of the carrier is used). The interested reader—who wants to learn this fascinating field in details—is encouraged to check excellent overview books written on the topic by the leading researchers in the field of spintronics, for example[1–6]. In the next sections the author gave short overview of the two spintronics effects necessary to understand his study: an inverse spin Hall effect and spin pumping.

When 50 years ago students of doctoral courses were writing their dissertations about physics of semiconductors using pen and paper, it was hard to imagine the progress that semiconductor field—and our life together with it—will undergo in the next half century. Today the author writes his dissertation on the Si transistors-based laptop, thanks to the previous generations of doctoral course students. It is the author's hope that when next generations of students will write their dissertations—some 50 years down the line—they will do it using spintronics-based devices. Author is happy to make a contribution to the development of germanium and graphene spintronics—the topics of this dissertation—and hopes that they will find their prominent place in science and technology in the future.

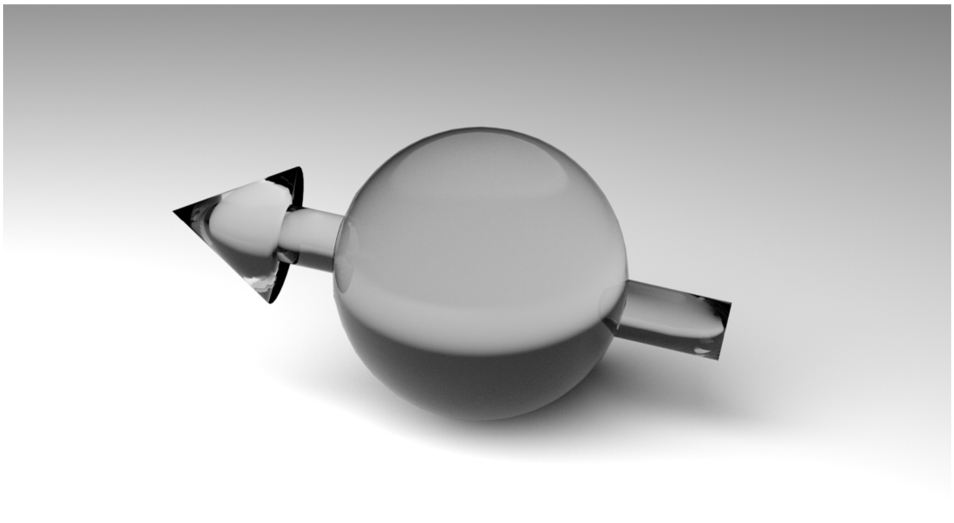

Figure 1-1. ~~Scanning electron microscopy image of a spin~~ A schematic image of a spin.

1.3 Spin Hall and inverse spin Hall effects

The term “spin Hall effect” was introduced by J. Hirsch in 1999 [8]. In his theoretical work Hirsch proposed that charge current will induce a transverse spin current and vice versa. These two reciprocal effects originate from the presence of spin-orbit interaction in materials. When carriers scatter in the presence of the spin-orbit interaction, the deflection direction during scattering event depends on the spin

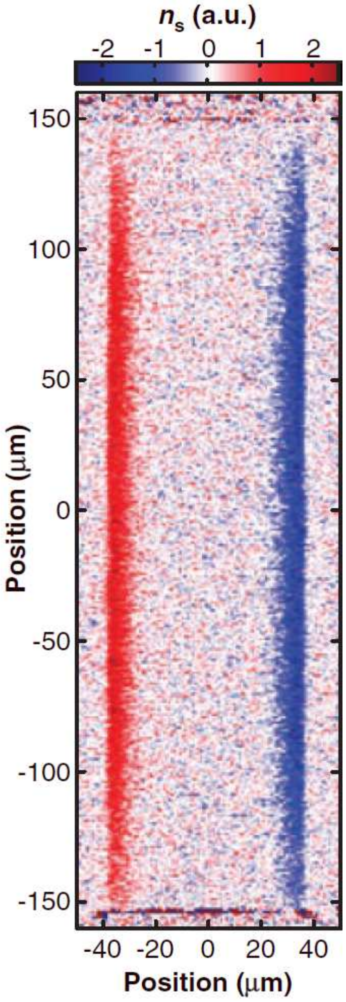

Figure 1-2. Image of the spin density n_s (for the out-of-plane spin polarization) in the unstrained GaAs measured using Kerr rotation at temperature T = 30 K by Kato *et al*. Electric field $E = 10\ \mathrm{mV/\mu m}$ was applied along long side of the sample ($l = 300$ μm). Charge current generated transverse spin current along short side of the sample ($w = 77$ μm) via spin Hall effect, which resulted in the induced out-of-plane spin polarization. **Figure adapted from**: Y. K. Kato. R. C. Myers, A. C. Gossard, and D. D. Awschalom. Observation of the Spin Hall Effect in Semiconductors. *Science* **306,** 1910–1913 (2004) [7].

of the carrier and its momentum. It was first pointed out in theoretical paper by N. Mott, who used the Dirac equation to calculate how spin direction affects the scattering of the electron beam by atomic nuclei[9]. Carriers with the opposite spins are deflected to the opposite sides, and thus produce transverse spin current. A reciprocal effect—when spin polarized current induces a transverse charge current—was named an inverse spin Hall effect.

Despite that name "spin Hall effect" was only proposed in 1999, the effect itself was theoretically predicted much earlier by M. Dyakonov and V. Perel in 1971 [11,12]. However, it took more than 30 years to experimentally observe the effect[7]. In 2004 Kato *et al.* used scanning Kerr rotation to measure spin polarization induced by charge current in different semiconductor channels (2 μm-thick unstrained n-type GaAs channel and 500 nm-thick strained n-type $In_{0.07}Ga_{0.93}As$ channel) at low temperature (T = 30 K) (Fig. 1-2). They found clear out-of-plane spin polarization at the edge of the samples, with opposite spin direction for opposite edges of the sample, as expected from the spin Hall effect. After the study by Kato *et al*. multiple other groups obtained similar results in both semiconductors and metals[13–19]. After 30 years

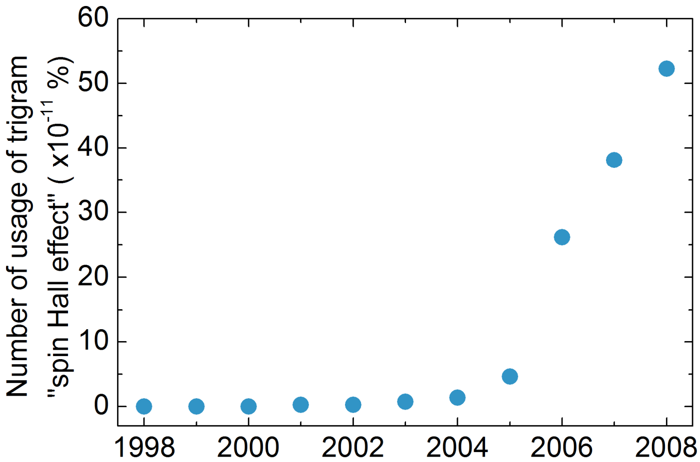

Figure 1-3. Percentage of the trigram "spin Hall effect" amongst all other trigrams in the books written in English from the Google books library. **Data in the graph are taken from**: Google Books Ngram Viewer (http://books.google.com/ngrams) J.-B. Michel, Y. K. Shen, A. P. Aiden, A. Veres, M. K. Gray, J. P. Pickett, D. Hoiberg, D. Clancy, P. Norvig, J. Orwant, S. Pinker, M. A. Nowak & E. L. Aiden. Quantitative Analysis of Culture Using Millions of Digitized Books. *Science* **331,** 176–182 (2011) [10].

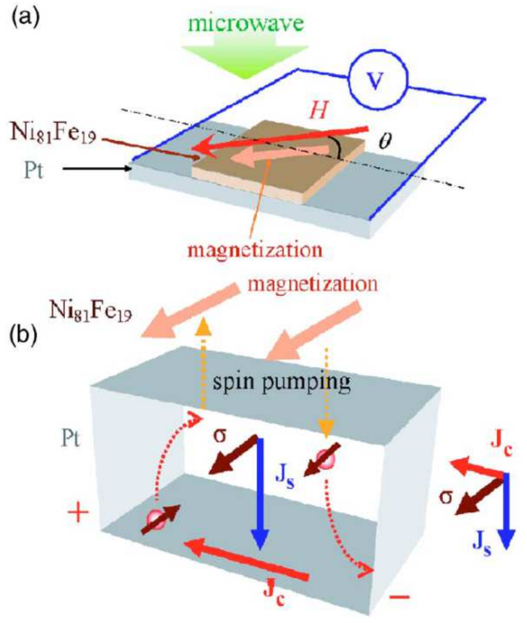

Figure 1-4. A schematic layout of the experiment carried out to measure inverse spin Hall effect induced by spin pumping under ferromagnetic resonance in $Ni_{81}Fe_{19}$/Pt system. **Figure adapted from:** E. Saitoh, M. Ueda, H. Miyajima & G. Tatara. Conversion of spin current into charge current at room temperature: Inverse spin-Hall effect. *Appl. Phys. Lett.* **88,** 182509 (2006) [20].

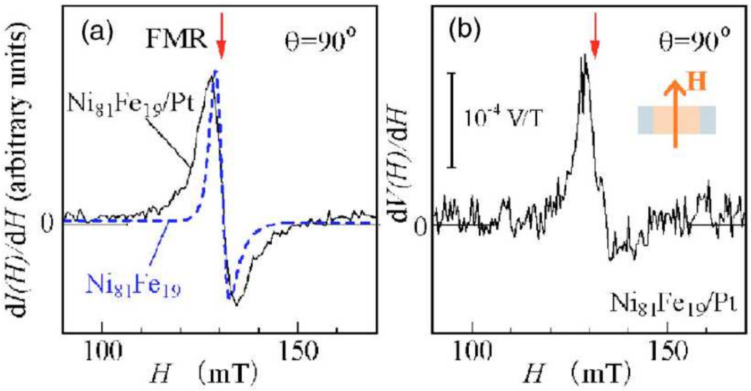

Figure 1-5. (a) Derivative ferromagnetic resonance absorbance spectrum of $Ni_{81}Fe_{19}$/Pt structure. **(b)** Electromotive force generated in $Ni_{81}Fe_{19}$/Pt structure due to the inverse spin Hall effect in Pt layer under the ferromagnetic resonance (FMR). **Figure adapted from:** E. Saitoh, M. Ueda, H. Miyajima & G. Tatara. Conversion of spin current into charge current at room temperature: Inverse spin-Hall effect. *Appl. Phys. Lett.* **88,** 182509 (2006) [20].

of small interest from scientific community in the spin Hall effect since the initial discovery, Kato's study triggered an avalanche of the studies (note the sharp rise after 2004 year in Fig. 1-3), and nowadays spin Hall effect is one of the hottest topics in the spintronics field.

The reciprocal effect to the spin Hall effect, namely the inverse spin Hall effect, describes conversion of spin current into charge current during spin-dependent scattering in the presence of spin-orbit interaction. It was theoretically predicted by N. Averkiev and M. Dyakonov in 1983 [21], and experimentally confirmed by A. Bakun *et al.* in 1984 [22]. In 2006 E. Saitoh *et al.* successfully measured inverse spin Hall effect in 10 nm Pt layer at room temperature[20]. Figure 1-4 shows layout of their experiment, and Figure 1-5 shows detected electromotive force due to inverse spin Hall effect in Pt layer. Their study triggered multiple other studies of the inverse spin Hall effect in the variety of materials: metals—Pt [23–37], Pd [24,32,38], W [37], Ag [37], Au [24,25,37], Mo [24,25], Cu [37], Ta [33,37]; semiconductors—p-Si [39], p-Ge [40], n-Ge [41], p-GaAs [42]; and even organic materials—PEDOT:PSS [43].

While it was unclear for a long while whether spin Hall effect and inverse spin Hall effect will find their application in real devices, in the 2012 study Liu *et al.* achieved switching of the ferromagnet magnetization using spin currents generated via spin Hall effect at room temperature. Using $Co_{40}Fe_{40}B_{20}$ (4 nm)/Ta (8 nm) devices they showed spin-torque switching of both out-of-plane and in-plane magnetized layers[33]. It has finally opened the route for practical application of the spin Hall effect in magnetic memory devices.

1.4 Spin pumping

The term "spin pumping" was introduced by Y. Tserkovnyak, A. Brataas and G. Bauer in their theoretical 2002 study[44,45]. In their paper they explained effect of the increased Gilbert damping constant in Pt/Py/Pt and Pd/Py/Pd trilayer structures comparing to the Cu/Py/Cu structure, observed one year earlier in the experimental study by S. Mizukami, Y. Ando and T. Miyazaki[46,47]. Figure 1-6 shows the Py thickness dependence of the Gilbert damping constant measured in Mizukami *et al.* studies[46,47]. Trilayer structures with metals with large periodic table numbers (Pd, Pt) showed clear enhancement of Gilbert damping constant comparing to the Cu/Py/Cu structures. Tserkovnyak *et al.* theoretically showed that magnetization precession in the ferromagnetic layer under the ferromagnetic resonance leads to the transfer of the angular momentum, hence, the generation of the pure spin in the adjacent layer, and the

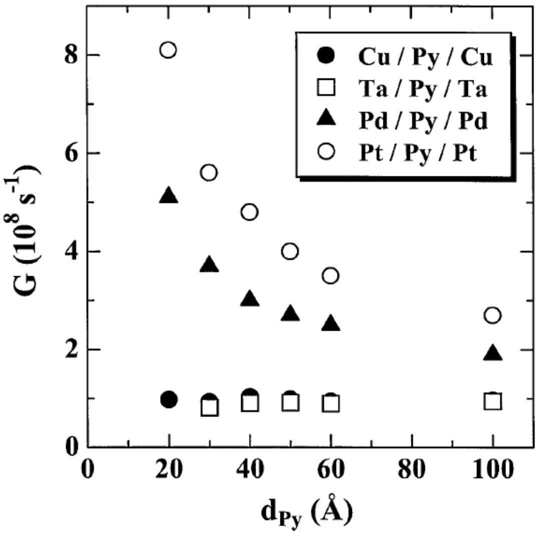

Figure 1-6. Experimentally measured permalloy thickness dependence of Gilbert damping constant for nonmagnetic/permalloy/nonmagnetic trilayer structures. **Figure adapted from:** S. Mizukami, Y. Ando & T. Miyazaki. Ferromagnetic resonance linewidth for NM/80NiFe/NM films (NM=Cu, Ta, Pd and Pt). *J. Magn. Magn. Mater.* **226-230,** 1640–1642 (2001) [47].

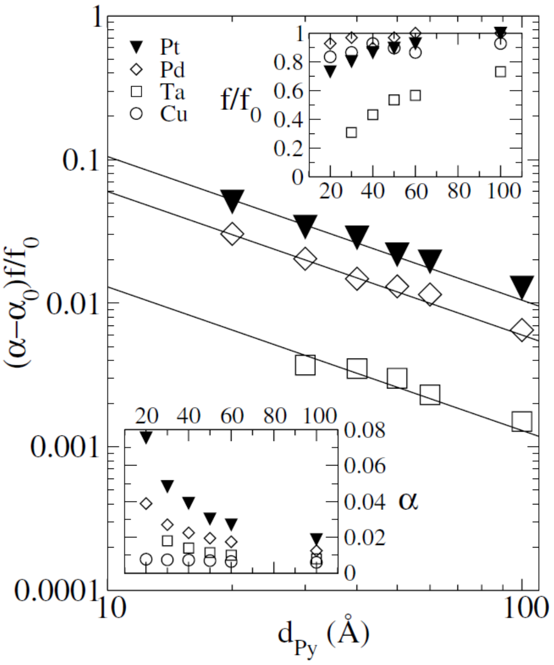

Figure 1-7. Theoretically calculated (lines) permalloy thickness dependence of Gilbert damping constant for nonmagnetic/permalloy/nonmagnetic trilayer structures. **Figure adapted from:** Y. Tserkovnyak, A. Brataas & G. E. W. Bauer. Enhanced Gilbert Damping in Thin Ferromagnetic Films. *Phys. Rev. Lett.* **88,** 117601 (2002) [44].

term "spin pumping". Total magnetic moment of the ferromagnetic layer decreases with its thickness, and magnetization precession becomes more sensitive to the loss of the angular momentum at the interface, leading to the increased Gilbert damping constant with the decreased thickness (Fig. 1-7). Layers that consisted of heavier metals (Pt, Pd) acted as better spin sink due to the large spin-orbit interaction and, thus, increased spin relaxation rate. As a follow up study S. Mizukami *et al*. confirmed predictions from the theoretical study of Y. Tserkovnyak *et al.,* for example correlation between spin diffusion length of the adjacent layer and Gilbert damping constant thickness dependence on its thickness (Figs. 1-8 and 1-9). After that confirmation spin pumping was recognized as a highly capable tool for spin injection. Since then spin pumping together with the inverse spin Hall effect were widely used as a spin injection and spin detection mechanism in various systems, as well as convenient way to measure spin diffusion length and spin Hall angle in multiple materials.

Electrical spin injection was successfully achieved in 1999, 3 years earlier than the spin pumping, in a breakthrough study by Y. Ohno *et al*[49], and was heavily dominating the spin injection scene for a while. However, the spin pumping introduced in 2002 is slowly catching up with electrical spin

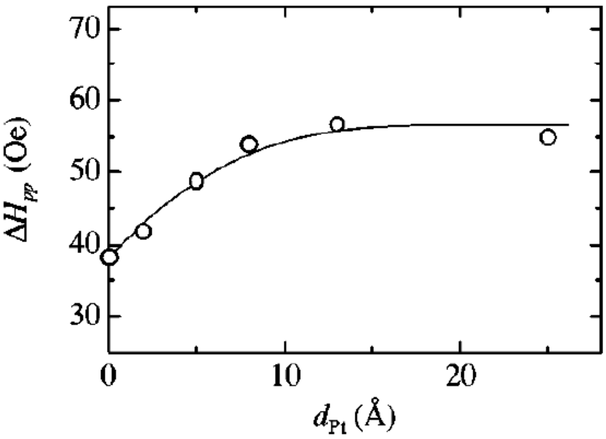

Figure 1-8. Ferromagnetic resonance peak-to-peak width dependence on the thickness of the Pt layer in Cu/Py (3 nm)/Cu (10 nm)/Pt (d_{Pt})/Cu multilayer structure (open black circles). Solid line is guide to the eye. **Figure adapted from:** S. Mizukami, Y. Ando & T. Miyazaki. Effect of spin diffusion on Gilbert damping for a very thin permalloy layer in Cu/permalloy/Cu/Pt films. *Phys. Rev. B* **66,** 104413 (2002) [48].

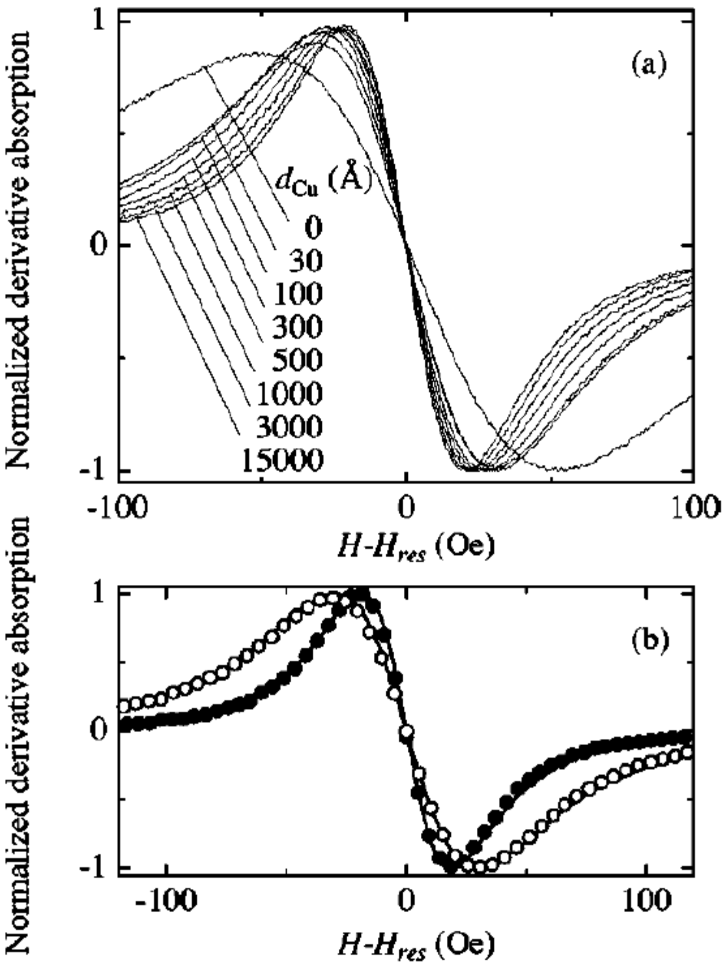

Figure 1-9. (a) Derivative ferromagnetic resonance spectrum dependence on the thickness of the Cu layer in Cu/Py (3 nm)/Cu (d_{Cu})/Pt multilayer structure. Peak-to-peak width of the ferromagnetic resonance spectrum increased together with the Cu thickness: thin Cu layer are less effective spin sink due the large spin diffusion length of Cu. **(b)** Derivative ferromagnetic resonance spectrum for the Cu/Py (3 nm)/Cu (10 nm)/Pt (open black circles) and Cu/Py (3 nm)/Cu (10 nm) (filled black circles) multilayer structures. Peak-to-peak width of the ferromagnetic resonance spectrum increased together with the addition of the Pt layer, which acted as effective spin absorber. **Figure adapted from:** S. Mizukami, Y. Ando & T. Miyazaki. Effect of spin diffusion on Gilbert damping for a very thin permalloy layer in Cu/permalloy/Cu/Pt films. *Phys. Rev. B* **66,** 104413 (2002) [48].

injection (Fig. 1- 10), and now also attracts great attention from the researchers—especially in a tandem with the inverse spin Hall effect.

Finally, the author notes that in the recent years it was discovered that NiFe (Py) layer itself can generate electromotive under the ferromagnetic resonance[50–52]. Figure 1-11 shows large symmetric in shape electromotive force generated under ferromagnetic resonance—the characteristic signature of the inverse spin Hall effect—in SiO_2/Py bilayer. Thus, care should be taken to separate contributions to the electromotive force from the inverse spin Hall effect in the studied material and spurious electromotive force that comes from the ferromagnetic spin source. Insulating spin source can be used to bypass this problem. In this light, ferrimagnetic insulator yttrium iron garnet became widely popular in the spin pumping experiments[37,53–60].

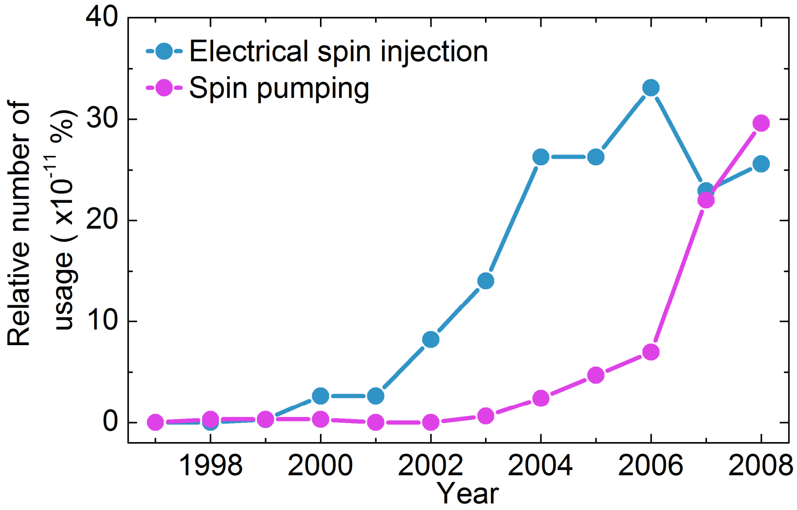

Figure 1-10. Percentage of the trigram “electrical spin injection” (blue filled circles) and bigram “spin injection” (purple filled circles) amongst all other trigrams and bigrams, respectively, in the books written in English from the Google books library. Lines are guide to the eye. **Data in the graph are taken from**: Google Books Ngram Viewer (http://books.google.com/ngrams) J.-B. Michel, Y. K. Shen, A. P. Aiden, A. Veres, M. K. Gray, J. P. Pickett, D. Hoiberg, D. Clancy, P. Norvig, J. Orwant, S. Pinker, M. A. Nowak & E. L. Aiden. Quantitative Analysis of Culture Using Millions of Digitized Books. *Science* **331,** 176–182 (2011) [10].

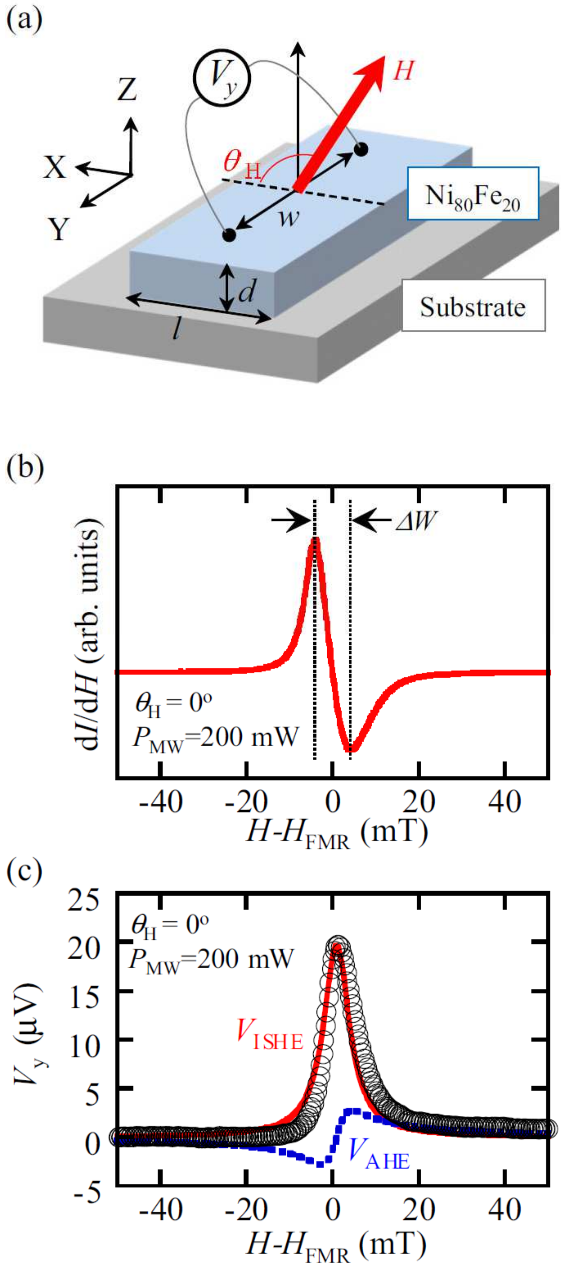

Figure 1-11. (a) A schematic layout of the experiment carried out to measure self-induced electromotive force in the SiO_2/Py (10 nm) structure during ferromagnetic resonance. **(b)** Derivative ferromagnetic resonance absorbance spectrum of SiO_2/Py structure. **(c)** Electromotive force generated in SiO_2/Py structure under the ferromagnetic resonance. Abbreviations on the figure stand for: FMR—ferromagnetic resonance, ISHE—inverse spin Hall effect, AHE—anomalous Hall effect. **Figure adapted from:** A. Tsukahara, Y. Ando, Y. Kitamura, H. Emoto, E. Shikoh, M. P. Delmo, T. Shinjo & M. Shiraishi. Self-induced inverse spin Hall effect in permalloy at room temperature. *Phys. Rev. B* **89,** 235317 (2014) [51].

1.5 Purpose of the author’s study

In this study the author focused on Group 14 of periodic table. Among unresolved questions that are left there, author chose the following two as the focus of the study: spin transport in Ge at room temperature, and origin of the spin-orbit interaction in single-layer graphene.

Despite recent progress in the Ge field, spin transport in Ge using non-local techniques has only been observed at low temperatures prior to the author’s study. In contrast, room-temperature spin transport in two lighter Group 14 elements—C and Si—was already achieved long time ago. Ge has the same crystal inversion symmetry as Si that precludes the spin relaxation of conduction electrons by the Dyakonov-Perel mechanism and should result in a long spin relaxation time. Additionally, carrier mobility in Ge is 10 times higher than in Si. Thus, Ge-based spin transport field effect transistors could overcome scaling limits of the Si-based devices. The author used methods introduced above—spin pumping for spin injection and the inverse spin Hall effect for spin detection—to achieve spin transport in Ge at room temperature for the first time in the world and pave a way for application of Ge-based spintronics devices.

One of the processes that suppress spin transport is the spin-charge conversion via spin-orbit interaction. It was shown that spin-charge conversion originates from the inverse spin Hall effect in Si and Ge. In contrast, origin and strength of spin-orbit interaction in single-layer graphene was still an open question prior to the author’s study. The author used spin pumping to inject spins into single-layer graphene and applied top gate voltage to distinguish between intrinsic-like (gives rise to inverse spin Hall effect) and Rashba-like (gives rise to inverse Rashba-Edelstein effect) spin-orbit interaction. Furthermore, the author demonstrated the correct normalization procedure for the inverse spin Hall effect voltages in spin pumping experiments in yttrium iron garnet/metal systems. Ferrimagnetic insulator yttrium iron garnet was widely used as the spin injector in spin pumping experiments in recent years as an alternative for conductive ferromagnets where spurious effects are always present. The author highlighted the factors that may lead to the incorrect analysis of inverse spin Hall effect in the previous studies and suggested a way to proper analyze of the ferromagnetic resonance and inverse spin Hall effect data in yttrium iron garnet-based systems.

Chapter 2. Room-temperature spin transport and spin relaxation mechanism in n-type germanium epilayers

2.1 Abstract

In this chapter the author reports the first experimental demonstration of room-temperature spin transport in n-type Ge epilayers grown on a Si(001) substrate. By utilizing spin pumping under ferromagnetic resonance, which inherently endows a spin battery function for semiconductors connected with a ferromagnet, a pure spin current is generated in the n-Ge at room temperature. The pure spin current is detected by using the inverse spin-Hall effect of either a Pt or Pd electrode on top of n-Ge. From a theoretical model that included a geometrical contribution the spin diffusion length in n-Ge at room temperature was estimated to be 660 nm. Moreover, the spin relaxation time decreased with increasing temperature, in agreement with a recently proposed theory of donor-driven spin relaxation in multivalley semiconductors.

Results presented in this chapter were published in the paper:

S. Dushenko, M. Koike, Y. Ando, T. Shinjo, M. Myronov, and M. Shiraishi, Experimental Demonstration of Room-Temperature Spin Transport in n-Type Germanium Epilayers, Phys. Rev. Lett. **114**, 196602 (2015).

2.2 Introduction and motivation

Group 14 semiconductors, such as Si and Ge, continue to attract tremendous attention in spintronics due to their suppression of spin relaxation. Crystal inversion symmetry of Si and Ge precludes the spin relaxation of conduction electrons by the Dyakonov-Perel mechanism[61], resulting in a long spin relaxation time. Although the spin-orbit interaction (SOI) of Ge is not negligibly small (0.29 eV), the SOI affects electrons much less than holes in Ge, making n-type Ge a promising material for spin transport. Furthermore, compared with Si, Ge possesses much higher carrier mobility[62]. Thus, it is possible for Ge-based spin transport field effect transistors with small gate lengths to overcome the scaling limits of Si-based devices. Additionally, in recent years, significant success has been achieved in the production of high-quality GeO_2 layer with gate function in the n-channel Ge-based metal oxide semiconductor field effect transistor[63]. Moreover, spin injection and spin relaxation in Ge have been extensively studied using electron spin resonance[64–69] and optical techniques[70–73]. However, in spite of all recent progress in the Ge field and in contrast to Si, spin transport in Ge using non-local 4-terminal techniques has only been observed at low temperatures to date[74–76]. Spin transport has been reported through a Ni/Ge/AlGaAs junction; however, optical spin injection lacks the scalability needed for nanoelectronic applications[77]. Some electrical studies[41,78,79] reported spin injection into highly doped n-Ge at room temperature, raising the possibility that room-temperature Ge-spintronics can be realized. Unfortunately, these studies used a 3-terminal local method, the reliability of which is now being called into question. Many recent studies demonstrated that signals in 3-terminal geometry originate *not* from spin accumulation in nonmagnetic channels but from magnetic field-dependent tunneling through localized states[80–86]. Other studies revealed that NiFe itself generates electromotive forces by the inverse spin-Hall effect (ISHE)[51] and the planar Hall effect[52]. Careful control experiments are indispensable to eliminate the self-induced electromotive forces from NiFe. Thus, realization of room-temperature spin transport in Ge is still an open challenge, and is long-awaited for further progress in semiconductor spintronics. The spin-pumping-induced generation of pure spin current originates from magnetization $\boldsymbol{M}(t)$ precession in the ferromagnetic layer under ferromagnetic resonance (FMR) conditions[26,44,87,88]. Using this highly promising tool, successful spin transport has been achieved at room temperature in single-layer graphene[89] and in semiconducting conjugated polymers[90]. In the author’s experiment, the magnetic moment was transferred through the interface of the ferromagnet and the adjacent n-Ge layer, creating pure spin current in the latter (Fig. 2-1(a)). After propagation through the n-Ge channel, the spins are absorbed in the metal electrode with strong SOI $\mathrm{Me}^{\mathrm{SOI}}$ [37,91,92] (Pt and Pd in the author's study). The SOI in $\mathrm{Me}^{\mathrm{SOI}}$ converts the spin current into charge current via ISHE[17,21,22,24,38], which is described by the following equation[20]: $\boldsymbol{J}_{\mathrm{C}} = D_{\mathrm{ISHE}}\, \boldsymbol{J}_{\mathrm{S}} \times \sigma$, where D_{ISHE} represents the ISHE efficiency of the material. The generated charge current can be detected as voltage at the end of the $\mathrm{Me}^{\mathrm{SOI}}$ strip.

Although the electronic properties of Ge are superior to those of Si, Ge wafers are heavier, less durable and much more expensive than their Si analogs. Thus, it is desirable to combine the high mobility of Ge channels with the durability and low cost of Si wafers. However, the 4.2% lattice mismatch between Si and Ge precludes direct epitaxial growth of high-quality relaxed Ge layers on top of Si wafers. Efforts to overcome this difficulty are still ongoing in Ge-related research[93–96]. In the author's study, high-quality Ge channels were successfully grown on top of Si (001) substrates using a two-temperature method. Additionally, in contrast to the usual use of solid-source molecular beam epitaxy and low-energy plasma-enhanced chemical vapor deposition for the production of high-quality channels, Ge channel in the author's study was produced using the reduced pressure chemical vapor deposition technique that is highly suitable for industrial production. The process described in this study is therefore readily translatable for commercial applications.

2.3 Experimental details

2.3.1 Fabrication of the samples

Figure 2-1(a) shows the structure of the n-Ge-based spin transport device used in the author's study. The Ge epilayers were grown on standard p^{-}-Si(001) substrates using the two-temperature growth method by reduced pressure chemical vapor deposition[94,96]. The structure consisted of a 1-μm-thick undoped Ge epilayer and 50 nm-thick heavily doped n-type Ge epilayer with a phosphorous doping concentration of $\sim 1.0\times10^{19}$ cm^{-3} and a degree of strain relaxation of 104%, calculated from the analysis of measured high-resolution X-ray diffraction symmetrical (004) and asymmetrical (224) reciprocal space maps. Over-relaxation of the Ge channel is attributed to the difference in the thermal expansion coefficients between Ge and Si, i.e., the Ge channel is 100% relaxed during the temperature growth,

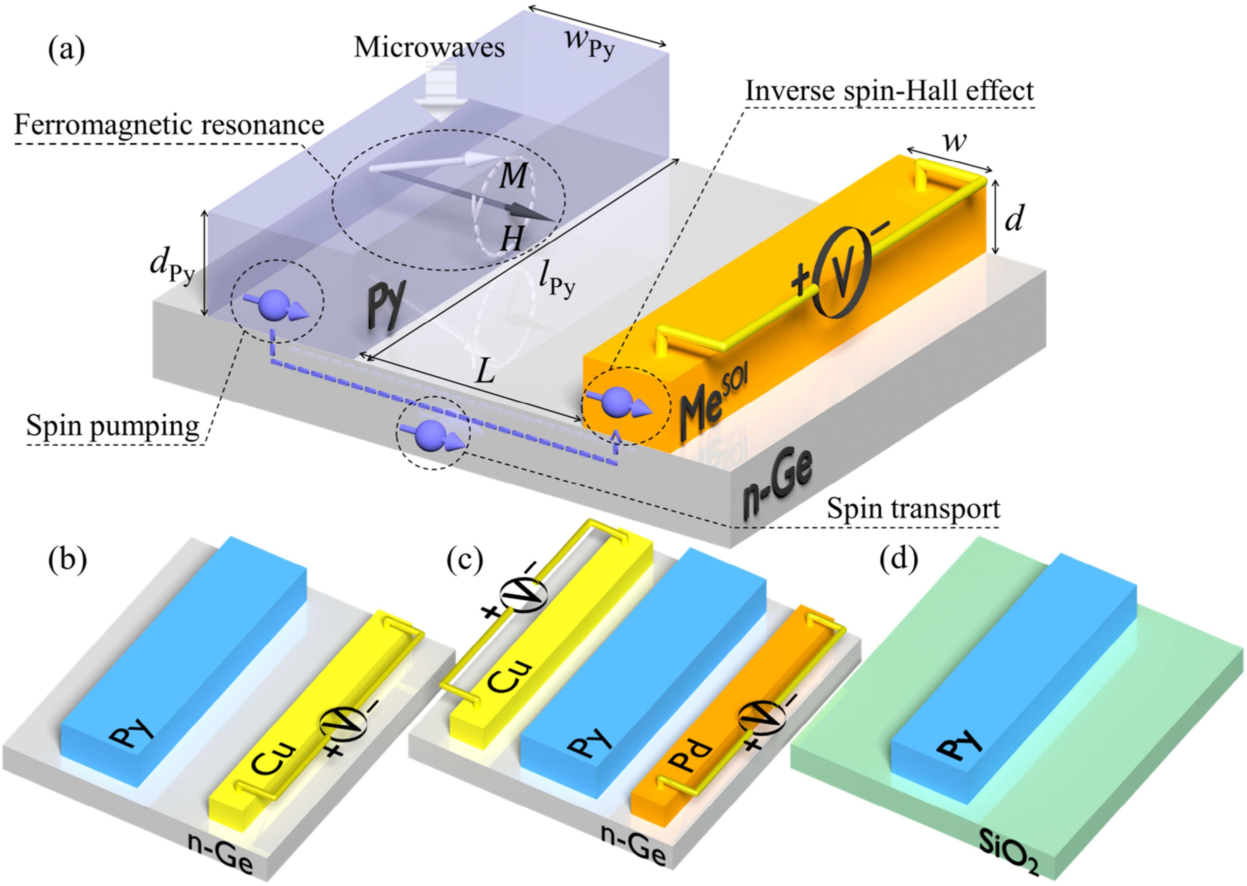

Figure 2-1. A schematic illustration of **(a)** the spin transport experiment in the Py/n-Ge/Me^{SOI} device, **(b)** Py/n-Ge/Cu and **(c)** Cu/n-Ge/Py/n-Ge/Pd samples used in the control experiments, and **(d)** Py/SiO$_2$ samples used for the spin current density estimation.

but is under slight tensile strain after cooling down to room temperature[94,95,97,98]. The Ge epilayers were measured to have a root mean square roughness below 1 nm by atomic force microscopy and had a threading dislocation density[94,99] of ~5×10^{6} cm^{-2} (Note: Ge channel was grown and analyzed by the author's collaborator: principal growth scientist Dr. M. Myronov from Nano-Silicon Group, Univ. of Warwick, United Kingdom). Me^{SOI} and $Ni_{80}Fe_{20}$ (Py) strips were formed on top of the n-Ge epilayers by electron beam lithography and electron beam evaporation. The samples were etched in 10% hydrofluoric acid solution and washed in deionized water prior to the evaporation of Me^{SOI} to remove the natural Ge oxide layer. Hereafter, the author's refers to this sample type as Py/n-Ge/Me^{SOI}.

2.3.2 Measurement procedure

Samples were placed in the center of a TE$_{102}$ cavity inside an electron spin resonance system with a microwave frequency f = 9.58 GHz. Ag paste was used to attach one Cu wire at each end of the Me^{SOI}

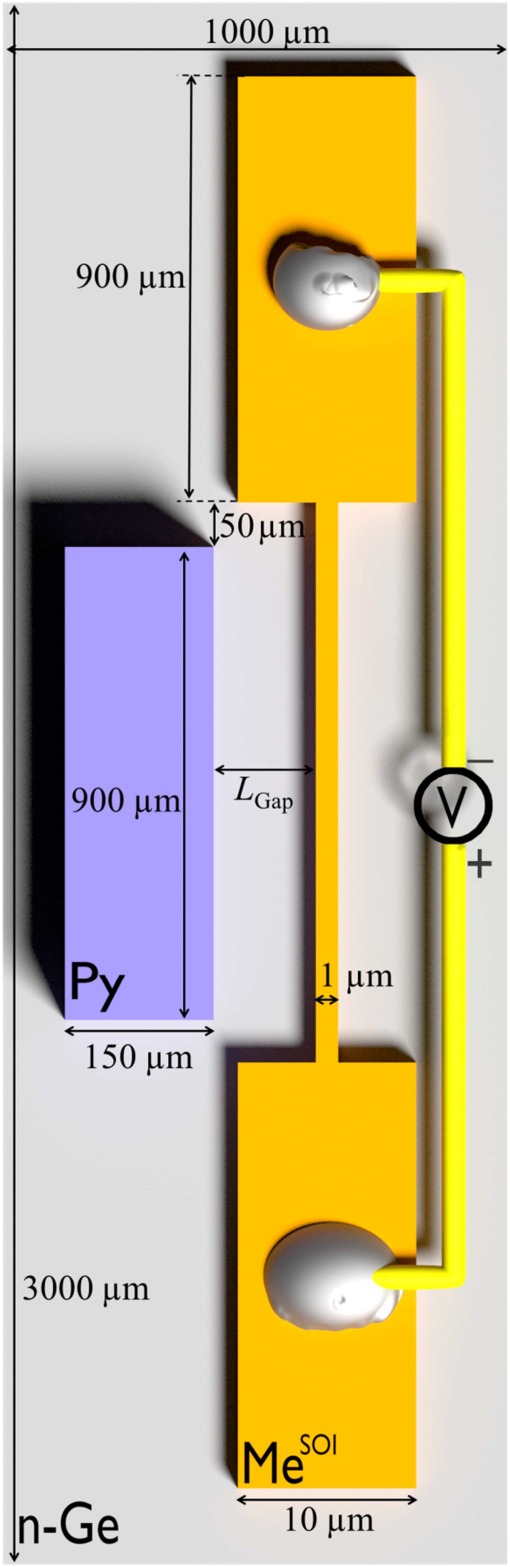

Figure 2-1. (e) A schematic layout of the Py/n-Ge/Me^{SOI} device with the sizes of the Py and Me^{SOI} electrodes, which were produced using electron beam lithography and electron beam evaporation.

strip to detect the voltage signal. The electromotive force from the sample was detected using a KEITHLEY 2182A Nanovoltmeter. Using identical sample fabrication and measurement procedures as described above, three different sample types were prepared, that is, Py/n-Ge/Cu (Fig. 2-1(b)), Cu/n-Ge/Py/n-Ge/Pd (Fig. 2-1(c)) and Py/SiO_2 (Fig. 2-1(d)). The first two sample types were used for the control experiments, whereas the third was used to calculate the spin current density at the Py/n-Ge interface, as explained in detail in the 2.4.3 section. Measurements, when not mentioned explicitly, were carried out at room temperature.

2.4 Experimental results and discussion

2.4.1 Electromotive force generated under the ferromagnetic resonance

The author now proceeds to describe the experimental results. Figure 2-3(a) shows the first derivative of the FMR spectrum, dI/dH. The blue and purple lines represent the spectra for Py/SiO_2 and Py/n-Ge/Pd, respectively. The enhanced peak-to-peak width of the FMR signal in the second case is due to the presence of spin pumping from Py into n-Ge under FMR conditions. When layer with available carriers (electrons in case of n-Ge) is adjacent to the ferromagnetic layer, under ferromagnetic resonance angular momentum from the ferromagnet is transferred through the interface to the adjacent layer, creating a pure spin current in the latter. However, if there are no carriers available (like in case of SiO_2), there is no transfer of angular momentum, hence no additional broadening of the ferromagnetic resonance spectrum (see Fig. 2-2 for schematic image).

The ISHE voltage is proportional to the generated spin current, the amplitude of which is proportional to the microwave absorption, which is maximized at the resonance field H_{FMR}. Hence, the voltage signal from the ISHE takes the shape of a symmetric peak with respect to H_{FMR}. The detected electromotive force was fitted using the function[20]

$$V(H) = V_{\mathrm{ISHE}} \frac{\Gamma^2}{\mu_0^2 (H - H_{\mathrm{FMR}})^2 + \Gamma^2} + V_{\mathrm{asym}} \frac{-2\Gamma \mu_0 (H - H_{\mathrm{FMR}})}{\mu_0^2 (H - H_{\mathrm{FMR}})^2 + \Gamma^2} + a\mu_0 H + b,$$

where the first term describes the symmetric contribution to the voltage signal from the ISHE. The second term describes the asymmetric contribution to the voltage from different spurious effects, including anomalous Hall effect, for which the voltage sign is reversed at the H_{FMR}; additionally, the last

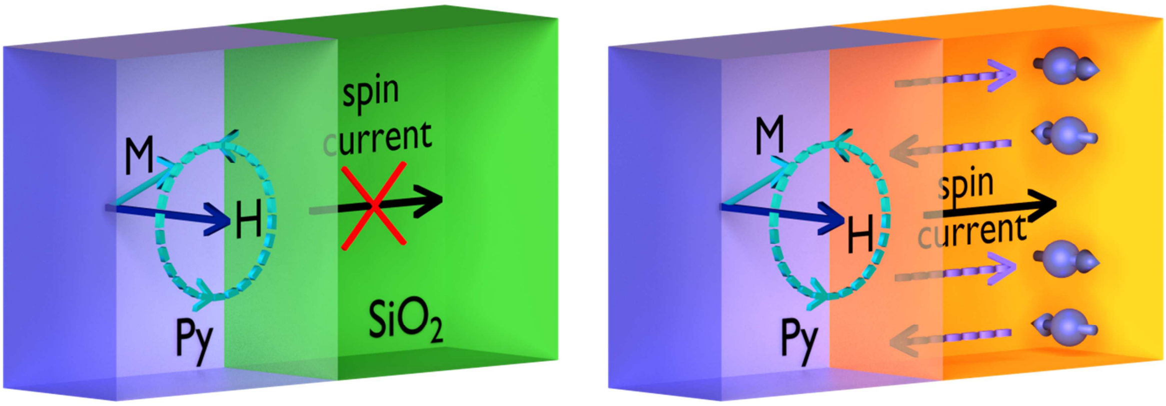

Figure 2-2. A schematic image of the dependence of the spin current generated under FMR on the adjacent layer in the ferromagnetic/nonmagnetic bilayer.

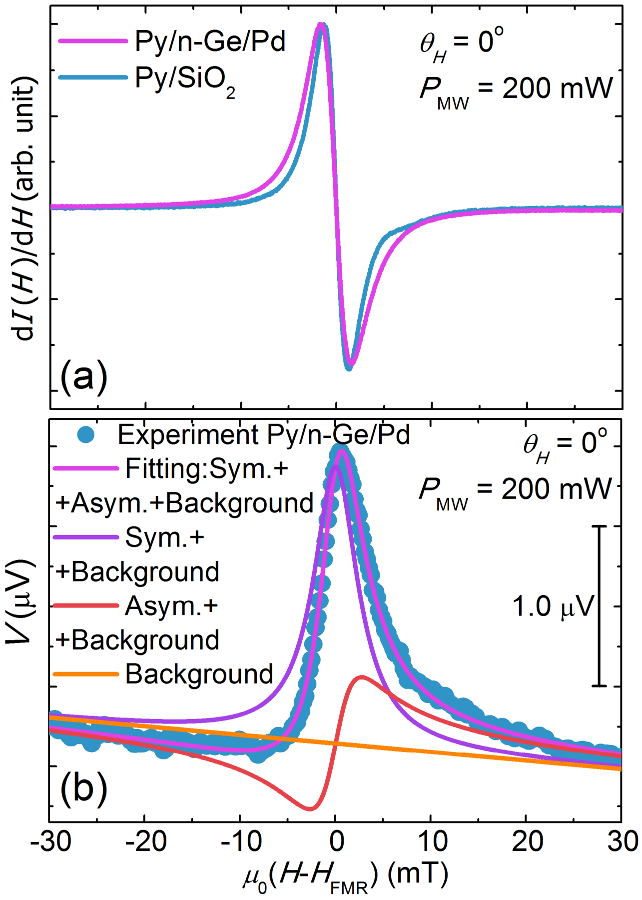

Figure 2-3. (a) FMR signal dI/dH dependence on the in-plane external magnetic field $\boldsymbol{H}$ for the Py/n-Ge/Pd (purple line) and Py/SiO$_2$ (blue line) samples at θ_H = 0°. H_{FMR} and I denote the resonance field and the microwave absorption intensity, respectively. **(b)** The electromotive force V detected from the Pd strip dependence on the in-plane external magnetic field $\boldsymbol{H}$ for the Py/n-Ge/Pd at θ_H = 0°. Filled blue circles denote the experimental data, and the colored lines show the fitting result.

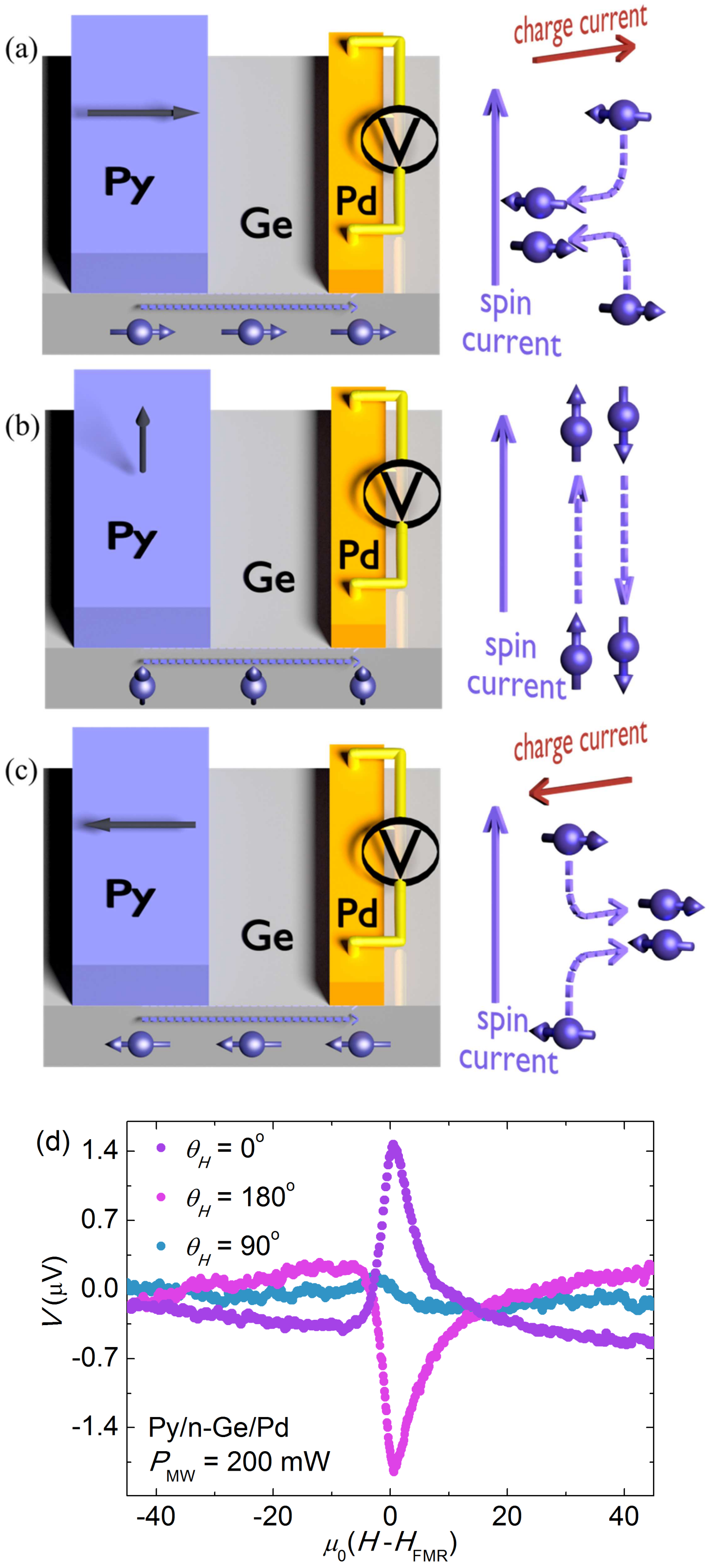

Figure 2-4. (a)-(c) A schematic illustration of the spin transport experiment in the Py/n-Ge/Pd structure with different direction of external magnetic field ***H***. **(a)** θ_H = 0°, **(b)** θ_H = 90°,**(c)** θ_H = 180°. **(d)** The electromotive force V detected from the Pd strip dependence on the in-plane external magnetic field ***H*** direction in the Py/n-Ge/Pd structure.

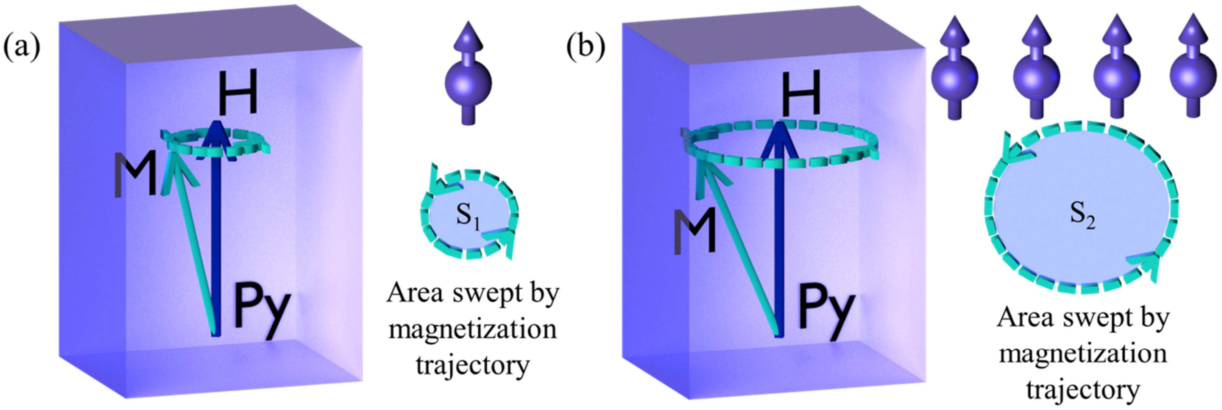

Figure 2-5. A schematic image of the dependence of the spin current generated under FMR on the area swept by magnetization trajectory

two terms represent the offset voltage (Fig. 2-3(b)). Fitting the experimentally detected voltage yielded the values of V_{ISHE} = 1.73 μV and V_{asym} = -0.43 μV. Finally, to eliminate any heating effects, the average of V_{ISHE} for opposing orientations of the external magnetic field $\boldsymbol{H}$ $\theta_H = 0°$ (shown on Fig. 2-1(a)) and $\theta_H = 180°$, was calculated as $V_{\mathrm{ISHE}} = (V_{\mathrm{ISHE}}|_{\theta_H=0°} - V_{\mathrm{ISHE}}|_{\theta_H=180°})/2$ giving a value of V_{ISHE} = 1.62 μV. Figures 2-7(a),2-7(b) show that a similar symmetrical voltage signal was detected from the Py/n-Ge/Pt sample.

2.4.2 Power dependence of the ferromagnetic resonance and electromotive force

Generated spin current is proportional to the area swept by the magnetization trajectory under the FMR (Fig. 2-5). Cone angle of the magnetization precession is given by $\theta_M = 2h/\Delta H_{\mathrm{FWHM}}$, where ΔH_{FWHM} is full width at half maximum of the FMR spectrum, and h is the microwave magnetic field. ΔH_{FWHM} was independent of power for both Py/n-Ge/Pd and Py/n-Ge samples (Fig. 2-6). Thus, V_{ISHE} should be proportional to the square of the microwave magnetic field h, making V_{ISHE} linearly proportional to the microwave power P_{MW}, as $V_{\mathrm{ISHE}} \propto h^2 \propto P_{\mathrm{MW}}$[38,100]. Consistent with this prediction, V_{ISHE} increased linearly with the P_{MW} for both the Py/n-Ge/Pt and Py/n-Ge/Pd samples (Figs. 2-7(a)–2-7(f)). The reversal of $\boldsymbol{H}$ to the opposite direction causes $\boldsymbol{\sigma}$ to change sign, which in turn leads to a change in the sign of the ISHE electric field $E_{\mathrm{ISHE}} \propto J_{\mathrm{C}}$. Figure 2-4(d) demonstrates the change in sign of the electromotive force upon the reversal of the magnetic field $\boldsymbol{H}$ to the opposite direction, thus demonstrating that the relation $J_{\mathrm{C}} = D_{\mathrm{ISHE}}\, J_{\mathrm{S}} \times \sigma$ for the ISHE holds in studied Py/n-Ge/Pd system.

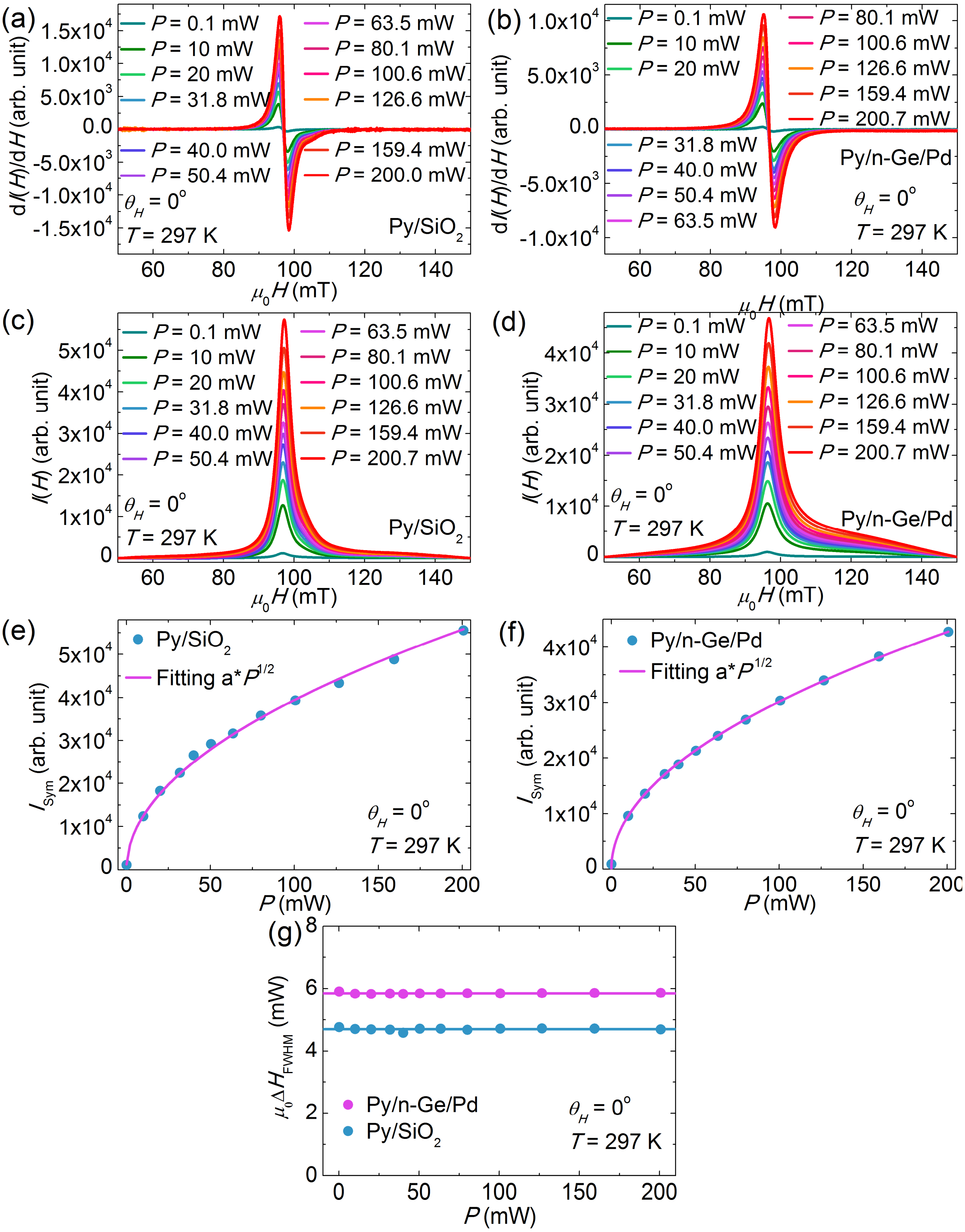

Figure 2-6. Power dependence of the derivative FMR spectra dI/dH for Py/SiO$_2$ **(a)** and Py/n-Ge/Pd **(b)**, FMR spectra $I(H)$ for Py/SiO$_2$ **(c)** and Py/n-Ge/Pd **(d)**, FMR amplitude I_{Sym} for Py/SiO$_2$ **(e)** and Py/n-Ge/Pd **(f)**, and FMR full width at half maximum **(g)**.Dependence $I_{\mathrm{Sym}} \propto \sqrt{P}$ shows absence of the FMR saturation effects in the range of applied microwave power.

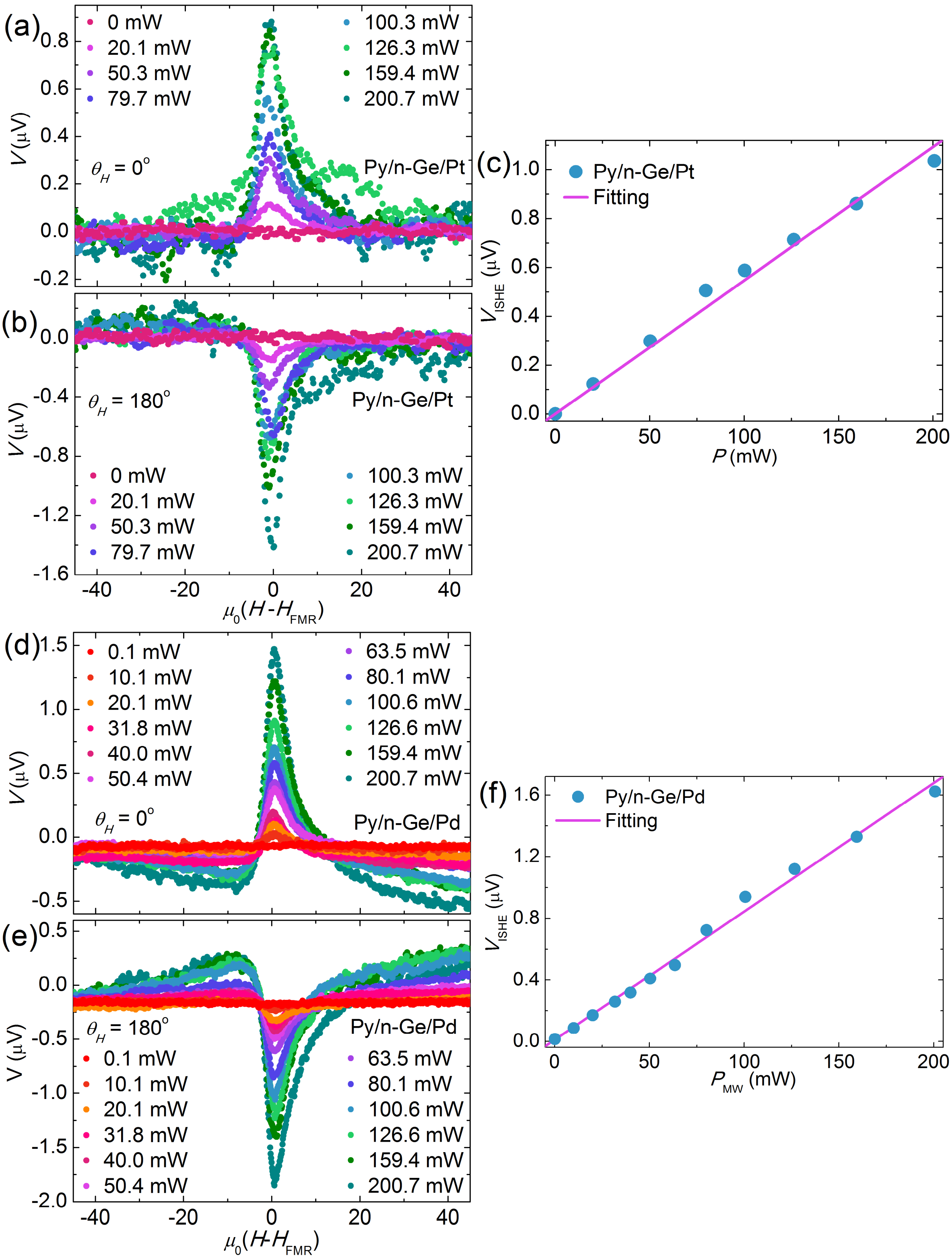

Figure 2-7. The electromotive force V detected at different microwave powers from the Me^{SOI} strip of the Py/n-Ge/Me^{SOI} sample under the FMR for the two external magnetic field $\boldsymbol{H}$ orientations **(a,d)** $\theta_H = 0°$ and **(b,e)** $\theta_H = 180°$. **(c,f)** Microwave power dependence of V_{ISHE} (filled blue circles) contribution to the electromotive force V detected from the Me^{SOI} strip of the Py/n-Ge/Me^{SOI}, where the solid lines denote the linear fit. **(a,b,c)** Me^{SOI} = Pt, **(d,e,f)** Me^{SOI} = Pd.

2.4.3 Calculation of the spin current density at the Py/n-Ge interface

Next, the author theoretically calculated the amplitude of V_{ISHE} for the Py/n-Ge/Pd sample. The estimation of the real part of the mixing conductance $g_{\mathrm{r}}^{\uparrow\downarrow}$ and spin current density at the ferromagnet/nonferromagnet interface is well established in a number of papers[24,38]. Under an effective magnetic field $\boldsymbol{H}_{\mathrm{eff}}$ the dynamics of the magnetization $\boldsymbol{M}(t)$ of the Py strip is described by the Landau-Lifshitz-Gilbert equation, given as

$$\frac{\mathrm{d}\boldsymbol{M}(t)}{\mathrm{d}t} = -\gamma \boldsymbol{M}(t) \times \boldsymbol{H}_{\mathrm{eff}} + \frac{\alpha}{M_{\mathrm{s}}} \boldsymbol{M}(t) \times \frac{\mathrm{d}\boldsymbol{M}(t)}{\mathrm{d}t},$$

where, γ, M_{s} and α are the gyromagnetic ratio, saturation magnetization and Gilbert damping constant, respectively. The resonance field H_{FMR} for the in-plane magnetic field is determined by the Kittel's formula[101] $(\omega/\gamma)^2 = H_{\mathrm{FMR}}\,(H_{\mathrm{FMR}} + 4\pi M_{\mathrm{S}})$, where $\omega = 2\pi f$ is the cyclic frequency of the magnetization precession. The precession of the magnetic moment of the Py leads to spin pumping from the Py into the n-Ge with the spin current density[26,38] of

$$j_{\mathrm{S}}^{\mathrm{Py/n-Ge}} = \frac{\omega}{2\pi} \int_0^{\frac{2\pi}{\omega}} \frac{\hbar}{4\pi} g_{\mathrm{r}}^{\uparrow\downarrow} \frac{1}{M_{\mathrm{s}}^2} \left[\boldsymbol{M}(t) \times \frac{\mathrm{d}\boldsymbol{M}(t)}{\mathrm{d}t}\right]_z \mathrm{d}t;$$

where $\hbar$ is the reduced Planck constant. The real part of the mixing conductance $g_{\mathrm{r}}^{\uparrow\downarrow}$ in equation above can be calculated from the difference in the FMR spectral width $W_{\mathrm{Py/n\text{-}Ge}}$ of the Py/n-Ge/Pd sample relative to W_{Py} of the Py/SiO$_2$ sample[24]:

$$g_{\mathrm{r}}^{\uparrow\downarrow} = \frac{2\sqrt{3}\pi M_S \gamma d_{\mathrm{Py}}}{g\mu_{\mathrm{B}}\omega}\left(W_{\mathrm{Py/n-Ge}} - W_{\mathrm{Py}}\right),$$

where g, μ_{B} and d_{Py} are the g-factor, Bohr magneton and thickness of the Py layer, respectively. Using the parameters $\mu_0 H_{\mathrm{FMR}}$ = 96.5 mT, g = 2.12[26], $\omega = 6.02\times10^{10}$ s^{-1}, $\gamma = 1.86\times10^{11}$ (Ts)$^{-1}$, $4\pi M_{\mathrm{S}}$= 0.984 T, d_{Py} = 25 nm, $W_{\mathrm{Py/n\text{-}Ge}}$ = 3.19 mT, W_{Py} = 2.55 mT, the real part of the mixing conductance was calculated to be $g_{\mathrm{r}}^{\uparrow\downarrow} = 2.15\times10^{19}$ m^{-2}. Py for Py/n-Ge/Me$^{\mathrm{SOI}}$ and Py/SiO$_2$ samples was always evaporated at the same time and chamber load to obtain the same Py quality for compared samples. Difference in the FMR full width at half maximum for samples produced on the same substrate was within ± 0.05 mT. Using the aforementioned parameters, the spin current density at the Py/n-Ge interface was obtained to be

$$j_{\mathrm{S}}^{\mathrm{Py/n-Ge}} = \frac{g_{\mathrm{r}}^{\uparrow\downarrow}\gamma^2 h^2 \hbar\left[4\pi M_{\mathrm{S}}\gamma + \sqrt{(4\pi M_{\mathrm{S}})^2\gamma^2 + 4\omega^2}\right]}{8\pi\alpha^2\left[(4\pi M_{\mathrm{S}})^2\gamma^2 + 4\omega^2\right]},$$

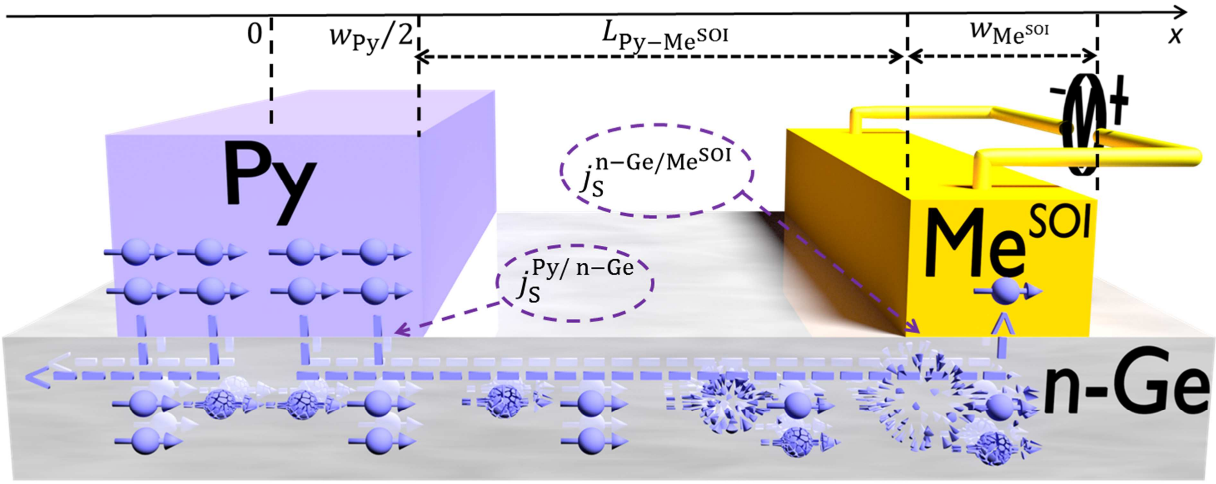

Figure 2-8. A schematic illustration of the spin current damping during propagation through the n-Ge channel.

where h was equal to 0.061 mT at a microwave power of 200 mW. Using the equation above, $j_{\mathrm{S}}^{\mathrm{Py/n-Ge}}$ was calculated to be 1.33×10^{-9} $\mathrm{Jm^{-2}}$.

2.4.4 Calculation of the spin current damping in the n-Ge channel

Furthermore, the author proposed a simple geometrical model to take into account spin current dissipation in the n-Ge channel (Fig. 2-8). During spin transport from Py to Pd through the n-Ge channel, the spin current density $j_{\mathrm{S}}^{\mathrm{Py/n-Ge}}$ is exponentially damped on the spin diffusion length $\lambda_{\text{n-Ge}}$ of n-Ge. Taking into account device geometry, the author assumed that half of the Py strip contributes to the spin current in the direction of the Pd strip. Integrating over this half gives the spin current density at the n-Ge/Pd interface as

$$j_{\mathrm{S}}^{\mathrm{n-Ge/Pd}} = j_{\mathrm{S}}^{\mathrm{Py/n-Ge}} \frac{1}{w_{\mathrm{Pd}}} \int_{0}^{\frac{w_{\mathrm{Py}}}{2}} e^{-\frac{L_{\mathrm{Py-Pd}}+x}{\lambda_{\mathrm{n-Ge}}}} \mathrm{d}x = j_{\mathrm{S}}^{\mathrm{Py/n-Ge}} e^{\frac{-L_{\mathrm{Py-Pd}}}{\lambda_{\mathrm{n-Ge}}}} \frac{\lambda_{\mathrm{n-Ge}}}{w_{\mathrm{Pd}}} \left(1 - e^{-\frac{w_{\mathrm{Py}}}{2\lambda_{\mathrm{n-Ge}}}}\right),$$

where $w_{\mathrm{Pd}} = 1.5$ μm is the width of the Pd strip. The gap length $L_{\text{Py-Pd}}$ was measured to be 620 nm using atomic force microscopy. The conductivity of the Pd $\sigma_{\mathrm{Pd}} = 1.97\times10^{6}$ $(\Omega\mathrm{m})^{-1}$ [38] is over one order of magnitude higher than that of the n-Ge channel used in the study $\sigma_{\text{n-Ge}} = 8.22\times10^{4}$ $(\Omega\mathrm{m})^{-1}$; this fact and the calculated value of $j_{\mathrm{S}}^{\mathrm{n-Ge/Pd}}$ allowed the author to modify the commonly used expression[38], and write down the voltage of the ISHE from the Pd strip as

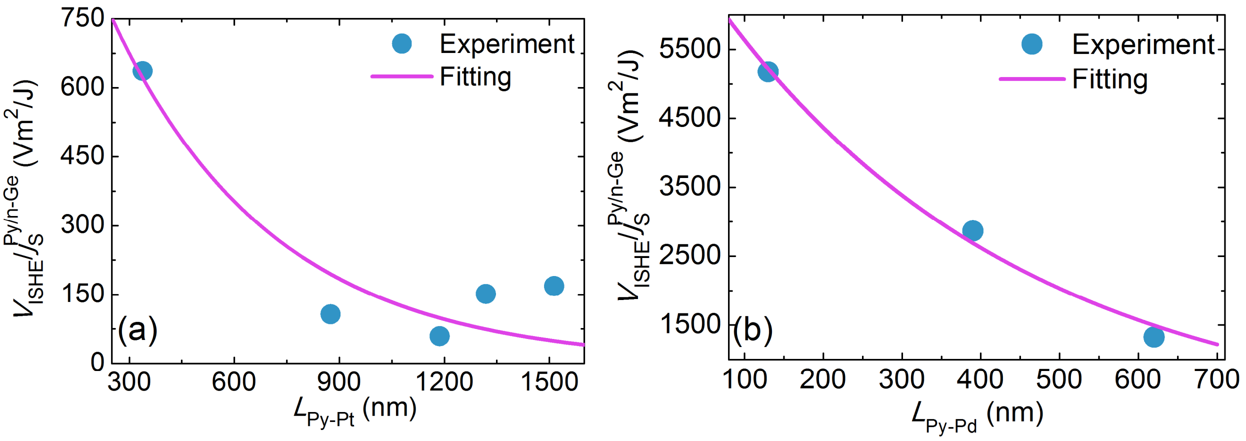

Figure 2-9. The gap length ($L_{\mathrm{Py-Me^{SOI}}}$) dependence of the normalized V_{ISHE} contribution to the electromotive force V detected from the **(a)** Pt strip of the Py/n-Ge/Pt samples and **(b)** Pd strip of the Py/n-Ge/Pd samples under the FMR. The filled blue circles represent V_{ISHE} normalized by spin current density at the Py/n-Ge interface $j_{\mathrm{S}}^{\mathrm{Py/n-Ge}}$, whereas the purple line is the fitting curve as described in the 2.4.5 section.

$$V_{\text{ISHE}} = \frac{l_{\text{Py}} \theta_{\text{SHE}} \lambda_{\text{Pd}} \tanh(d_{\text{Pd}}/2\lambda_{\text{Pd}})}{d_{\text{Pd}} \sigma_{\text{Pd}}} \left(\frac{2e}{\hbar}\right) j_{\mathrm{S}}^{\mathrm{n-Ge/Pd}},$$

where l_{Py} = 900 μm is the length of the Py strip, d_{Pd} = 10 nm is the thickness of the Pd strip, and θ_{SHE} = 0.01 [38] and λ_{Pd} = 9 nm[102] are the spin-Hall angle and the spin diffusion length of the Pd, respectively. Using the experimentally measured V_{ISHE} = 1.62 μV and the equations above, the author calculated the value of the spin diffusion length in the n-Ge to be $\lambda_{\text{n-Ge}}$ = 680 nm.

2.4.5 Estimation of the spin diffusion length in n-Ge channel from the gap length dependence

Formation of germanide at the n-Ge/Me$^{\text{SOI}}$ interface can take place at comparatively low temperatures, which can be achieved during the metal evaporation process: it may have led to the changes in spin transport properties of the n-Ge/Me$^{\text{SOI}}$ interface. However, these changes do not depend on the gap distance $L_{\mathrm{Py-Me^{SOI}}}$ between the Py and Me$^{\text{SOI}}$ strips. To confirm the $\lambda_{\text{n-Ge}}$ estimation, the dependence of the gap length $L_{\mathrm{Py-Me^{SOI}}}$ was measured. The V_{ISHE} behavior over changes in $L_{\mathrm{Py-Me^{SOI}}}$ is governed through spin current density damping in the n-Ge layer. Figure 2-9(a) shows the fitting of the gap length $L_{\text{Py-Pt}}$ dependence of the normalized V_{ISHE} with the function

$$V_{\text{ISHE}}/j_{\text{S}}^{\text{Py/n-Ge}} = A\lambda_{\text{n-Ge}}e^{-L/\lambda_{\text{n-Ge}}}\left(1-e^{-\frac{w_{\text{Py}}}{2\lambda_{\text{n-Ge}}}}\right)$$

Using the above fitting function, the spin diffusion length $\lambda_{\text{n-Ge}}$ was estimated to be 460 nm. From the dependence of the normalized V_{ISHE} in the Py/n-Ge/Pd samples (Fig. 2-9(b)) on the gap length $L_{\text{Py-Pd}}$, $\lambda_{\text{n-Ge}}$ was estimated to be 580 nm.

Finally, taking the data from all samples into account, the author estimated the spin diffusion length in the n-Ge channel at room temperature to be $\lambda_{\text{n-Ge}} = 660 \pm 200$ nm. The spin diffusion length in highly doped n-Ge (with a doping concentration of $n = 2\times10^{19}$ cm^{-3}) was reported to be 580 nm at 4 K[74]. An important step forward was made 3 years later, when $\lambda_{\text{n-Ge}} = 590$ nm was realized at 150 K in n-Ge channel ($n = 10^{18}$ cm^{-3}) [76]. The author made a final step towards room temperature Ge spintronics by achieving $\lambda_{\text{n-Ge}} = 660 \pm 200$ nm at room temperature.

2.4.6 Control experiments

As a part of the control experiment, a sample of Py/n-Ge/Cu was prepared with a Cu strip (Fig. 2-1(b)), instead of a Me$^{\text{SOI}}$ strip. The gap distance $L_{\text{Py-Cu}}$ was measured to be 490 nm. Figs. 2-10(g) and 2-10(h) show the detected electromotive force under a microwave excitation of 200 mW for two sample orientations. In contrast to the Py/n-Ge/Pt and Py/n-Ge/Pd samples, the electromotive force possesses an asymmetric shape that reverses its sign over H_{FMR}. This fact strongly indicates that the origin of the symmetric part of the electromotive force signal in the Py/n-Ge/Pt and Py/n-Ge/Pd samples is the ISHE in Pt and Pd, which have significantly stronger SOI than Cu (SOI scales approximately as Z^4, where Z is atomic number of the material[37]). As a second part of the control experiment, the sample of Cu/n-Ge/Py/n-Ge/Pd (Fig. 2-1(c)) was produced with both Pd and Cu strips, which were located on different sides of the Py strip. The gap distance between Py and Pd was measured to be $L_{\text{Py-Pd}} = 320$ nm, whereas that between Py and Cu was measured to be $L_{\text{Py-Cu}} = 420$ nm; the microwave power was set to 40 mW. From the Cu strip, similar to the previous case, an asymmetric electromotive force shape was detected (Figs. 2-10(i) and 2-10(j)), which is in contrast to the electromotive force from the Pd strip; the latter did not change sign over H_{FMR}, but instead acquired a symmetric shape (Figs. 2-10(k) and 2-10(l)), as

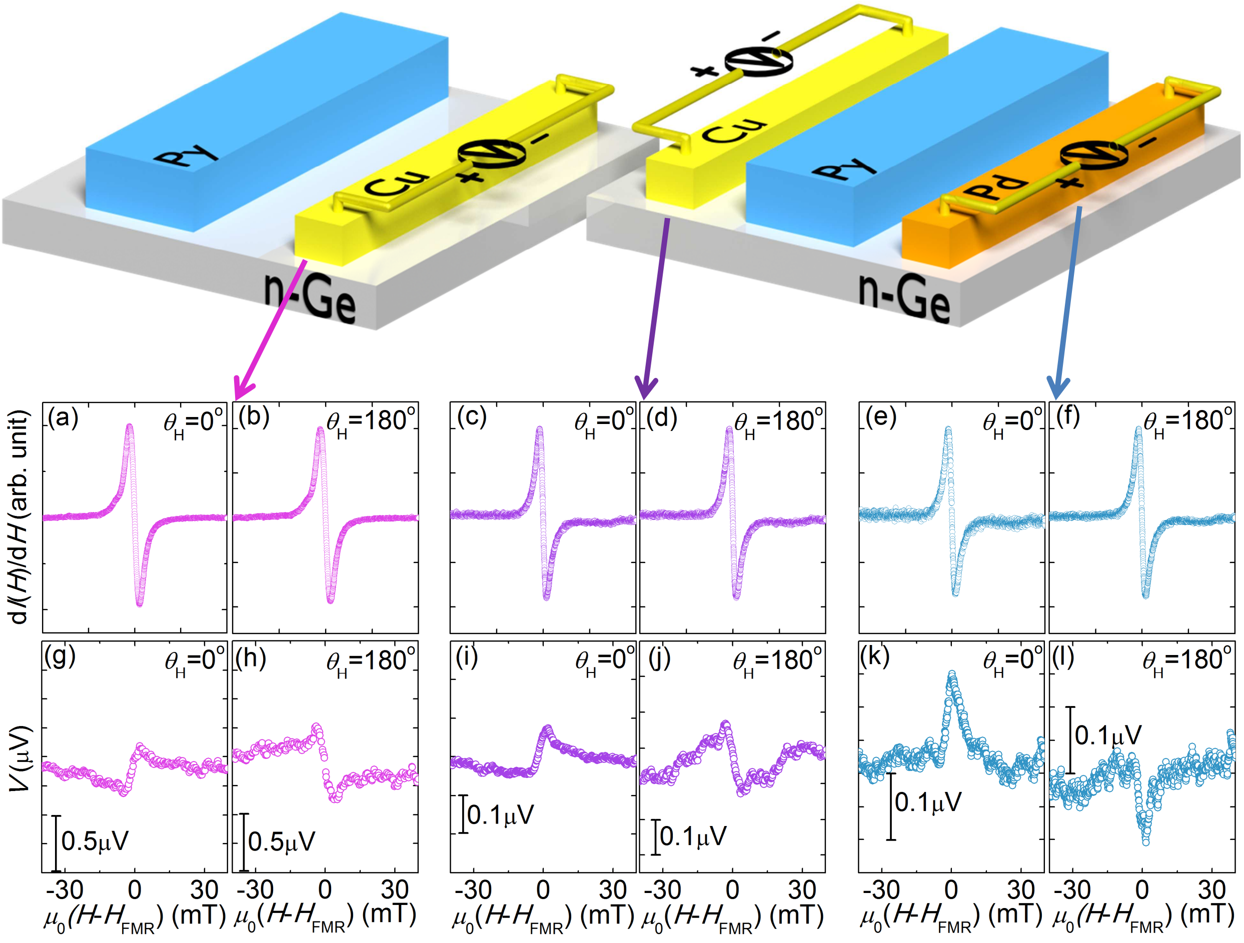

Figure 2-10. The FMR signal d*I*/d*H* dependence on the in-plane external magnetic field ***H*** for Py/n-Ge/Cu **(a)** θ_H = 0° and **(b)** θ_H = 180°, for Cu/n-Ge/Py/n-Ge/Pd **(c,e)** θ_H = 0° and **(d,f)** θ_H = 180°. The electromotive force *V* detected under FMR from the Cu strip of the Py/n-Ge/Cu sample **(g)** θ_H = 0° and **(h)** θ_H = 180°, from the Cu strip of the Cu/n-Ge/Py/n-Ge/Pd sample **(i)** θ_H = 0° and **(j)** θ_H = 180°, from the Pd strip of the Cu/n-Ge/Py/n-Ge/Pd sample **(k)** θ_H = 0° and **(l)** θ_H = 180°.

expected from the ISHE. It should be noted that this result provides direct evidence of successful spin transport in n-Ge at room temperature because an asymmetric signal was detected from Cu, whereas a distinctly symmetric electromotive force was detected from Pt and Pd.

2.4.7 Determination of the temperature dependence of the carrier mobility in the n-Ge channel using maximum-entropy mobility spectrum analysis

To determine the mobility in the n-Ge channel samples for magnetoresistance measurements were prepared. Contact pads (5 nm-thick Ti/45 nm-thick Au) were formed on top of the n-Ge epilayers by electron beam evaporation. The samples were etched in 10% hydrofluoric acid solution and washed in

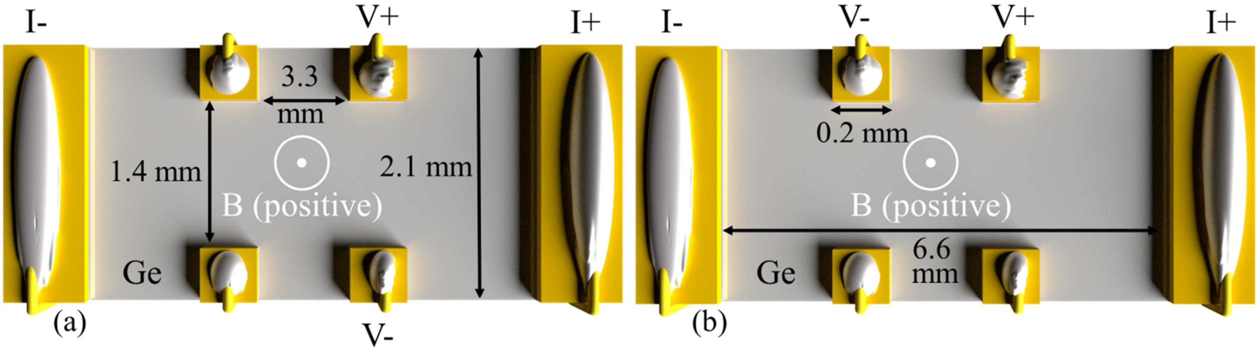

Figure 2-11. A schematic layout of the (a) Hall resistance and (b) magnetoresistance measurements of the n-Ge channel

deionized water prior to the evaporation of contact pads to remove the natural Ge oxide layer. The Hall resistance (Fig. 2-11(a)) and magnetoresistance (Fig. 2-11(b)) of the n-Ge channel were measured in the magnetic field range from 0 to 9 T at certain temperatures. Afterwards, the mobility $\mu_{\text{n-Ge}}$ was determined by a maximum-entropy mobility spectrum analysis of the magnetic field dependence of the Hall resistance and magnetoresistance (Note: while the author himself carried out all magnetoresistance and Hall resistance measurements, maximum-entropy mobility spectrum analysis—using data measured by the author—was done by Dr. Maksym Myronov from Nano-Silicon, Univ. of Warwick, United Kingdom). The entire procedure was repeated for all needed temperatures, and the obtained $\mu_{\text{n-Ge}}(T)$ is shown in Fig. 2-12. In the maximum-entropy mobility spectrum analysis components of the magnetoconductivity tensor, $\sigma_{xy}(B)$ and $\sigma_{xx}(B)$ are calculated from the sheet values of the Hall resistivity $\rho_{\text{xy}}(B)$ and magnetoresistivity $\rho_{xx}(B)$ and then converted into a mobility-dependent conductivity tensor $s(\mu)$ (also called mobility spectrum) using the following equations[103,104]:

$$\sigma_{xx}(B) = \int_{-\infty}^{\infty} \frac{s(\mu)}{1+(\mu B)^2} d\mu,$$

$$\sigma_{xy}(B) = \int_{-\infty}^{\infty} \frac{s(\mu)\mu B}{1+(\mu B)^2} d\mu$$

Then, the mobility spectrum $s(\mu)$ that provides the best fit to $\sigma_{xx}(B)$ and $\sigma_{xy}(B)$ is found using the entropy maximization approach (Fig. 2-13). For the detailed explanation of the maximum-entropy mobility spectrum analysis, please see[104].

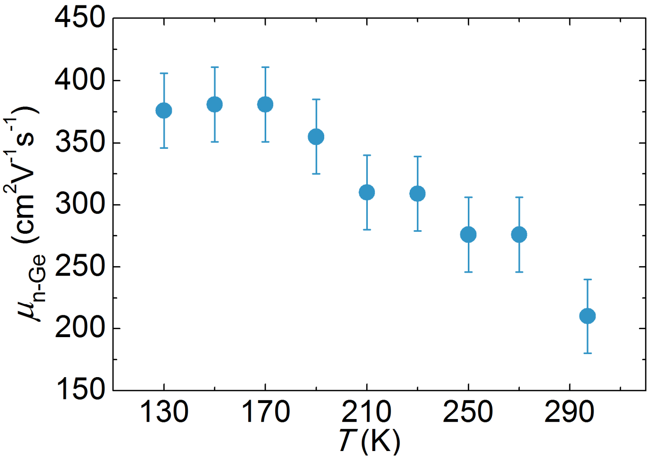

Figure 2-12. Temperature dependence of the mobility of the n-Ge epilayer obtained from the maximum-entropy mobility spectrum analysis. Error bars are defined by the maximum-entropy mobility spectrum analysis fitting parameters.

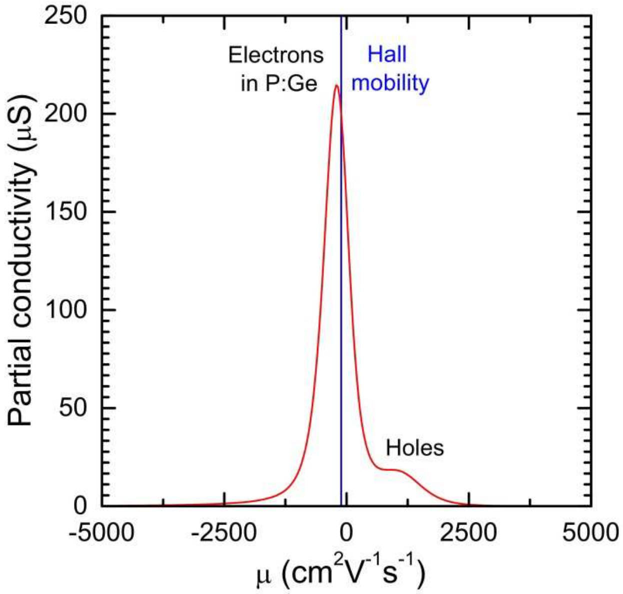

Figure 2-13. Characteristic mobility spectrum obtained for the n-Ge channels used in author's study. Peak in conductivity at negative mobility corresponds to the electron carriers in the 50 nm heavily n-type doped Ge epilayer (phosphorous doping concentration of ~1.0×10^{19} cm^{-3}). Additional small peak at positive mobility corresponds to the hole carriers in the 1 μm-thick undoped Ge epilayer under main channel.

2.4.8 Temperature dependence of spin transport properties and spin relaxation mechanism

The author measured the temperature dependence of the ISHE voltage in the Py/n-Ge/Pt sample to shed light on the spin relaxation mechanism in the n-Ge epilayers used in the study. The author assumed the Elliott-Yafet mechanism[105,106] of spin Hall conductivity of Pt, i.e., $\lambda_{\mathrm{Pt}}(T) \propto \sigma_{\mathrm{Pt}}(T)$, and constant spin Hall conductivity with changing temperature[18,107,108]. Additionally, spin pumping efficiency, determined by $\Delta H_{\mathrm{FWHM}}^{\mathrm{Py/n-Ge/Pd}} - \Delta H_{\mathrm{FWHM}}^{\mathrm{SiO_2}}$, was independent of temperature (Figs. 2-14 and 2-15). This is in agreement with the linear *I*-*V* curves observed using two terminal measurements, and the fact that spin pumping was reported to be free of the impedance mismatch problem[100]. Using the aforementioned, the author extracted $\lambda_{\mathrm{n\text{-}Ge}}(T)/\lambda_{\mathrm{n\text{-}Ge}}$ (297 K) (Fig. 2-16(a)). Furthermore, the temperature dependence of the mobility of the n-Ge channel $\mu_{\mathrm{n\text{-}Ge}}$ was determined using maximum-entropy mobility spectrum analysis[103,104]. Mobility in the n-Ge channel changed from 210±30 cm^{2}V^{-1}s^{-1} at room temperature to 376±30 cm^{2}V^{-1}s^{-1} at 130 K (Fig. 2-12). Mobility value of the Ge channel was smaller than in bulk Ge crystals (up to 1000 cm^{2}V^{-1}s^{-1}), however, it was still larger than in Si with doping concentration of 10^{19} cm^{-3} (up to 100 cm^{2}V^{-1}s^{-1})[62,109,110]. The spin relaxation time $\tau_{\mathrm{n\text{-}Ge}}$ is related to spin diffusion length by the equation $\lambda_{\mathrm{n\text{-}Ge}} = \sqrt{D\tau_{\mathrm{n-Ge}}}$, where *D* is the diffusion constant directly proportional to the mobility $\mu_{\mathrm{n\text{-}Ge}}$. This allowed the author to plot the ratio $\tau_{\mathrm{n\text{-}Ge}}(\mathrm{T})/\tau_{\mathrm{n\text{-}Ge}}$ (297 K) as a function of temperature (Fig. 2-16(b)). The lowest conduction band in germanium consists of four L valleys, with the center Γ valley located 0.14 eV above it. The spin relaxation time due to intravalley scattering between lower conduction and upper valence bands follows $T^{-7/2}$ dependence[106]. However, due to spatial inversion and time reversal symmetries of the L-point in Ge, the intravalley spin-flip matrix elements for both phonon-induced scattering[111] and impurity-induced scattering[112] are very small. Thus, intravalley-induced spin scattering can only be dominant at low temperatures ($T < 20$K[111]), rendering intervalley spin scattering to be the main spin relaxation mechanism in this work ($T > 130$ K). Recently, a novel spin relaxation mechanism by intervalley scattering in the presence of magnetic field originating from *g*-factor anisotropy was discovered in Ge[113]. However, in the author's case, due to degenerate doping and ultrafast spin-conserving momentum relaxation time at temperatures close to room temperature, this mechanism is suppressed. Using the amplitude of the external magnetic field $B \sim 0.1$T and intervalley momentum relaxation time < 1 ps[111] in Eq. 4 from[113], one can find that the contribution to the spin relaxation from the

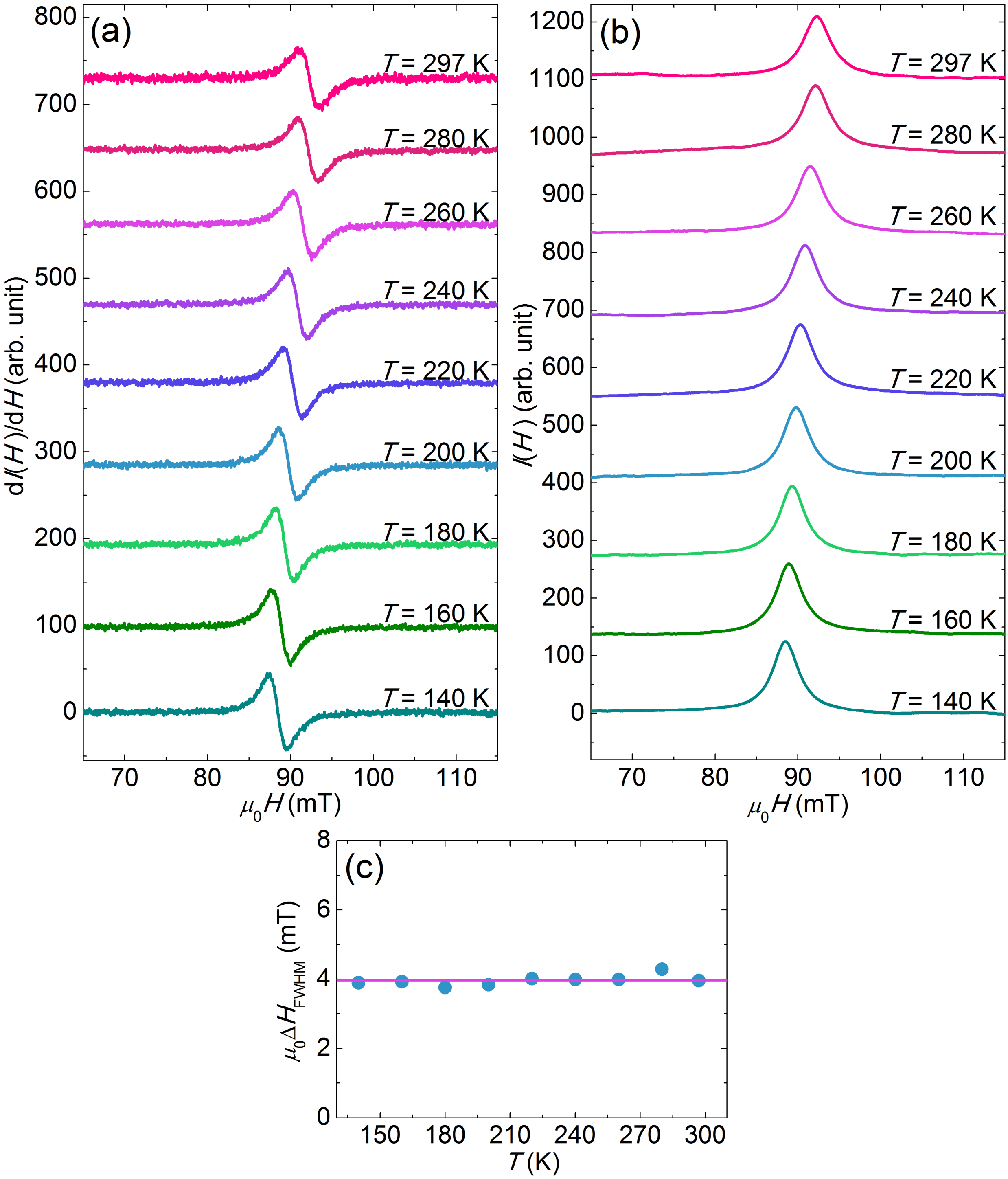

Figure 2-14. Temperature dependence of the **(a)** derivative FMR spectrum d*I*/d*H*, (b) FMR spectrum *I*(*H*) and full width at half maximum ΔH_{FWHM} of FMR spectrum for Py/SiO$_2$ structure. In **(c)** filled blue circles are experimental data, purple line is fitting by the constant.

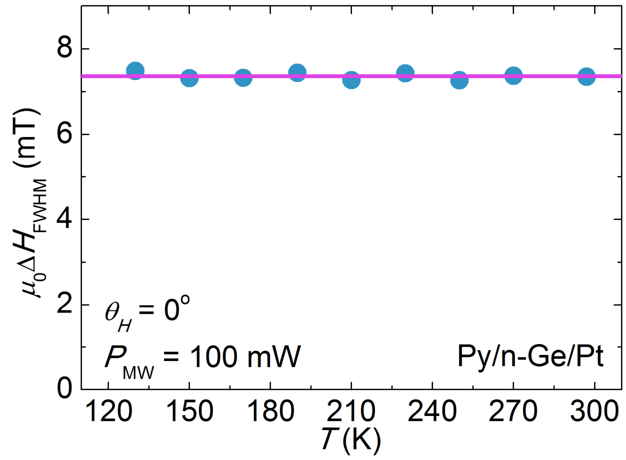

Figure 2-15. Temperature dependence of the full width at half maximum ΔH_{FWHM} of FMR spectrum for Py/n-Ge/Pt structure. Filled blue circles are experimental data, purple line is fitting by the constant.

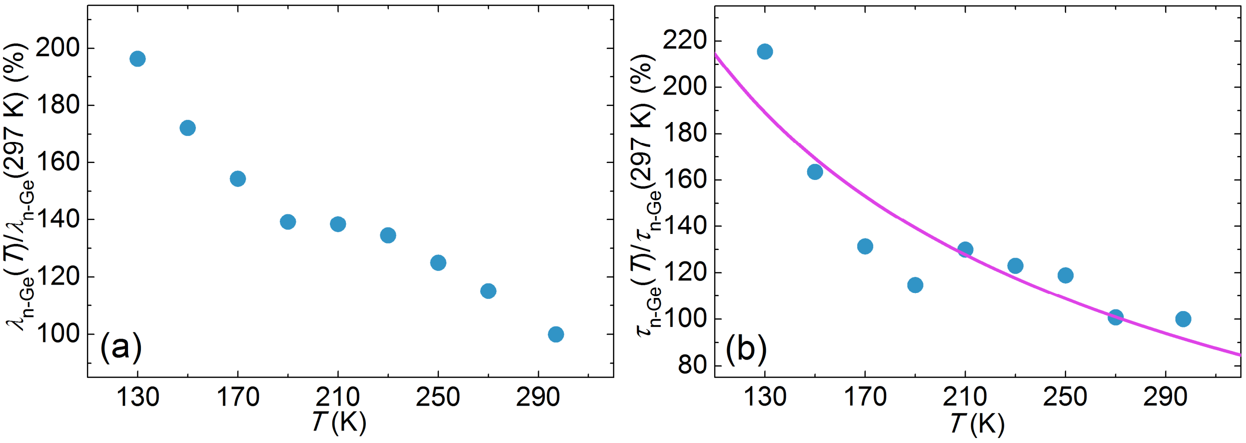

Figure 2-16. Temperature dependence of the **(a)** spin diffusion length and **(b)** spin relaxation time of electrons in the n-Ge channel normalized by room-temperature values. Purple line is inverse square root fitting, as discussed in the text.

g-factor anisotropy mechanism is negligible compared to intervalley scattering with phonons. Spin relaxation due to intervalley electron-phonon scattering is governed by X phonons, which connect the centers of two different L-valleys[73]. These phonons have an energy of approximately 30 meV[73,111,114] and obey the Bose-Einstein temperature distribution. It results in a strong exponential behavior of spin relaxation time around room temperature[111]. By contrast, the spin relaxation time showed weak temperature dependence and increased only by a factor 2.2 from room temperature to T = 130 K. Therefore, the author ruled out intervalley spin relaxation due to phonon scattering as a dominant mechanism in the studied n-Ge channels. Indeed, the author observed saturation of the carrier mobility below 170 K, which indicates dominance of the ionized impurity over phonon scattering in the highly doped n-Ge channel at least at low temperatures. A recent theory[112] showed that in Ge, impurity scattering spin relaxation is governed by an intervalley short range scattering off the central-cell potential of impurities. In this theory, in strong degenerate regimes, the spin relaxation time exhibits $1/\sqrt{T}$ behavior (see Eq. (4) in[112]), which is similar to the weak dependence of $\tau_{\text{n-Ge}}(T)$ observed in this work. Thus, in the highly doped n-Ge used in the study, impurity spin scattering is dominant over other spin relaxation mechanisms. Finally, in addition to considered bulk spin relaxation mechanisms, the author cannot exclude a possible contribution from interface spin scattering. However, the donor-driven spin relaxation mechanism discussed above holds also for the interface spin relaxation, if the scattering centers at the interface allow for scattering between two valleys residing on different crystallographic axes. From spin transport experiments, the Elliott-Yafet mechanism was reported to be dominant in highly doped n-Ge, but the data range was only up to 100 K[74,75], with no correlation of $\tau_{\text{n-Ge}}$ with temperature in the range from 150 K to 225 K[76]. Thus, for the first time, the author covered the important range from 130 K to room temperature and provided experimental evidences for impurity-driven spin relaxation mechanism in highly doped n-Ge.

2.5 Conclusion

In summary, the author was the first to directly demonstrate spin transport at room temperature in epitaxial n-Ge with a doping concentration of ~1.0×10^{19} cm^{-3} using a spin pumping method and ISHE. The spin diffusion length in Ge at room temperature was estimated to be $\lambda_{\text{n-Ge}}$ = 660 ± 200 nm. The spin diffusion length was comparable to the reported values for Si channels with similar doping concentration

(λ_{Si} = 600 nm at doping concentration n = 5×10^{19} cm^{-3}) [115]. However, limit for the electron mobility in bulk Ge is 5 times larger than mobility observed in the Ge channels used in the author's study. Thus, spin diffusion length can be further increased with improving quality of the Ge channel. Additionally, author showed that the spin relaxation time increased with decreasing temperature, in agreement with recently proposed theory of donor-driven spin relaxation in multivalley semiconductors[112]. Strain control over spin relaxation at L-point can further improve spin relaxation time and spin diffusion length. As a result of the author's study, room-temperature Ge spintronics was established. Room-temperature spin transport has now been shown in both pivotal semiconductor materials, Ge and Si, providing new opportunities for the future of semiconductor spintronics.

Chapter 3. Gate-tunable spin-charge conversion and a role of spin-orbit interaction in a single-layer graphene

3.1 Abstract

The small spin-orbit interaction of carbon atoms in graphene promises a long spin diffusion length and potential to create a spin field-effect transistor. However, for this reason, graphene was largely overlooked as a possible spin-charge conversion material. In this chapter the author reports electric gate tuning of the spin-charge conversion voltage signal in a single-layer graphene. Using spin pumping from yttrium iron garnet ferrimagnetic insulator and ionic liquid top gate the author determined that the inverse spin Hall effect is the dominant spin-charge conversion mechanism in a single-layer graphene. From the gate dependence of the electromotive force the author showed dominance of the intrinsic over Rashba spin-orbit interaction, and estimate its strength to be ~1 meV: a long-standing question in graphene research.

Results presented in this chapter submitted to:

S. Dushenko, H. Ago, K. Kawahara, T. Tsuda, S. Kuwabata, T. Takenobu, T. Shinjo, Y. Ando, and M. Shiraishi, Gate-tunable spin-charge conversion and a role of spin-orbit interaction in graphene, Phys. Rev Lett, submitted.

3.2 Introduction and motivation

Spintronics promises salvation from the scaling limitations of electronics. However, to create spin-logic devices, long spin transport and control of the spin current must be achieved. In this light, single-layer graphene (SLG)[116]—a two-dimensional sheet of carbon atoms bound together by sp^2 hybridized orbitals in a honeycomb lattice—has received tremendous attention as a potential material for spintronic devices. Graphene has a long spin relaxation time and spin diffusion length[117,118], and, due to its two-dimensional nature, its electronic properties can be easily modulated by gate voltage[119]. Another important requirement to create spintronic devices is the ability to convert spin current into charge current and vice versa. The spins of the carriers are coupled to the angular momentum of the lattice atoms through the spin-orbit interaction (SOI). However, SOI is not restricted to the lattice atoms and fundamentally originates from the coupling between the electric field and the moving spin, and enables the conversion of the pure spin current into the charge current (inverse spin Hall effect[21,22], inverse Rashba-Edelstein effect[120,121]) and reciprocally (spin Hall effect[7,11] Rashba-Edelstein effect[122–124]). In this recently-emerged experimental spin-charge conversion branch of spintronics, graphene was largely overlooked due to the very small intrinsic spin-orbit interaction of carbon atoms, with only a few experimental studies performed[125,126]. Despite many theoretical studies, there is still no agreement in the literature today on the strength and type of the spin-charge conversion and underlying spin-orbit interaction mechanism in graphene (dependent or independent on electric field). The author’s aim in this study was to experimentally distinguish between spin-orbit interaction mechanisms in SLG. By measuring the gate voltage dependence of the spin-charge conversion in SLG on top of ferrimagnetic insulator yttrium iron garnet (YIG), the author determined the dominant type of spin-charge conversion mechanism. It allowed the author to estimate spin-orbit interaction strength in pristine SLG, which itself was a long-standing question in graphene research.

The author used spin pumping[44,48] to generate a pure spin current in the SLG. In spin pumping, precession of the magnetization in the ferromagnetic layer drives pure spin current through the ferromagnetic interface. Spin current transfers the spin-angular momentum from the ferromagnetic layer to the adjacent layer, thus leading to enhanced relaxation of the magnetization precession under ferromagnetic resonance (FMR) conditions. Spin pumping was shown to overcome the conductance mismatch problem[100], and has recently been widely used for spin injection in semiconductors[127], conjugated polymers[90] and SLG[89]. As a ferrimagnetic insulator, YIG has great potential as a spin source due to its low magnetic damping and band gap of 2.7 eV at room temperature. The large band gap at room temperature prevents spurious voltage signals from the ferrimagnetic layer, which are present in the case of common metallic ferromagnets[51]. Spin injection into graphene using spin pumping recently received attention both from theoretical[128] and experimental[89,125] studies. In this chapter—using spin injection from the YIG substrate via spin pumping—the author studied spin-orbit interaction in SLG and achieve spin-charge conversion tuning using gate voltage application.

3.3 Experimental details

3.3.1 Layout of the experiment

A schematic layout of the experiment is shown in Fig. 3-1. Precession of the magnetic moment in the YIG layer under FMR conditions led to the flow of the angular momentum into the adjacent SLG (Fig. 3-1(a)). In the SLG, due to the spin-charge conversion, the spin current was converted into a charge current. The generated charge current was detected as a voltage at the Ti/Au contact pads on the opposite sides of the sample (Fig. 3-1(c)). The carrier density and carrier type were controlled via an ionic liquid electric gate on top of the SLG (Fig. 3-1(b)).

3.3.2 Fabrication of the samples

The YIG (2 μm in thickness, lateral sizes 1.5 mm × 4 mm) was grown on gadolinium gallium garnet substrate by liquid phase epitaxy and is commercially available (GRANOPT, Akita, Japan). The top YIG surface was polished using agglomerate-free alumina polishing suspension, with a particle size of 0.05 μm for 6 min and was afterwards annealed in air atmosphere at 800°C for 2 hours. SLG was grown using atmospheric pressure chemical vapor deposition on top of an epitaxial Cu(111) film at 1075°C[129]. Spin coated poly(methyl methacrylate) and Fe-free etchant ammonium persulfate $(NH_4)2S_2O_8$ were used to transfer SLG onto the gadolinium gallium garnet/YIG substrate to avoid magnetic impurities in the SLG (Note: single-layer graphene was grown by the author’s collaborators Prof. H. Ago and K. Kawahara from the Carbon Electronics Group, Institute for Materials and Chemical Research, Kyushu University, Japan). Ti (5 nm)/Au (100 nm) pads were formed by electron beam evaporation on top of the

SLG, with a width of 0.5 mm and a channel length between pads of 2 mm. Wiring was performed using Cu wire with a diameter of 100 µm and Ag paste. The ionic liquid top gate was prepared using a mixture of 60 vol% PVdF-HFP (solution of poly(vinylidene fluoride-co-hexafluoropropylene) in acetone, with 1 g of polymer per 30 ml of acetone) and 40 vol% BF_4 ($C_8H_{15}BF_4N_2$ 1-butyl-3-methylimidazolium tetrafluoroborate).

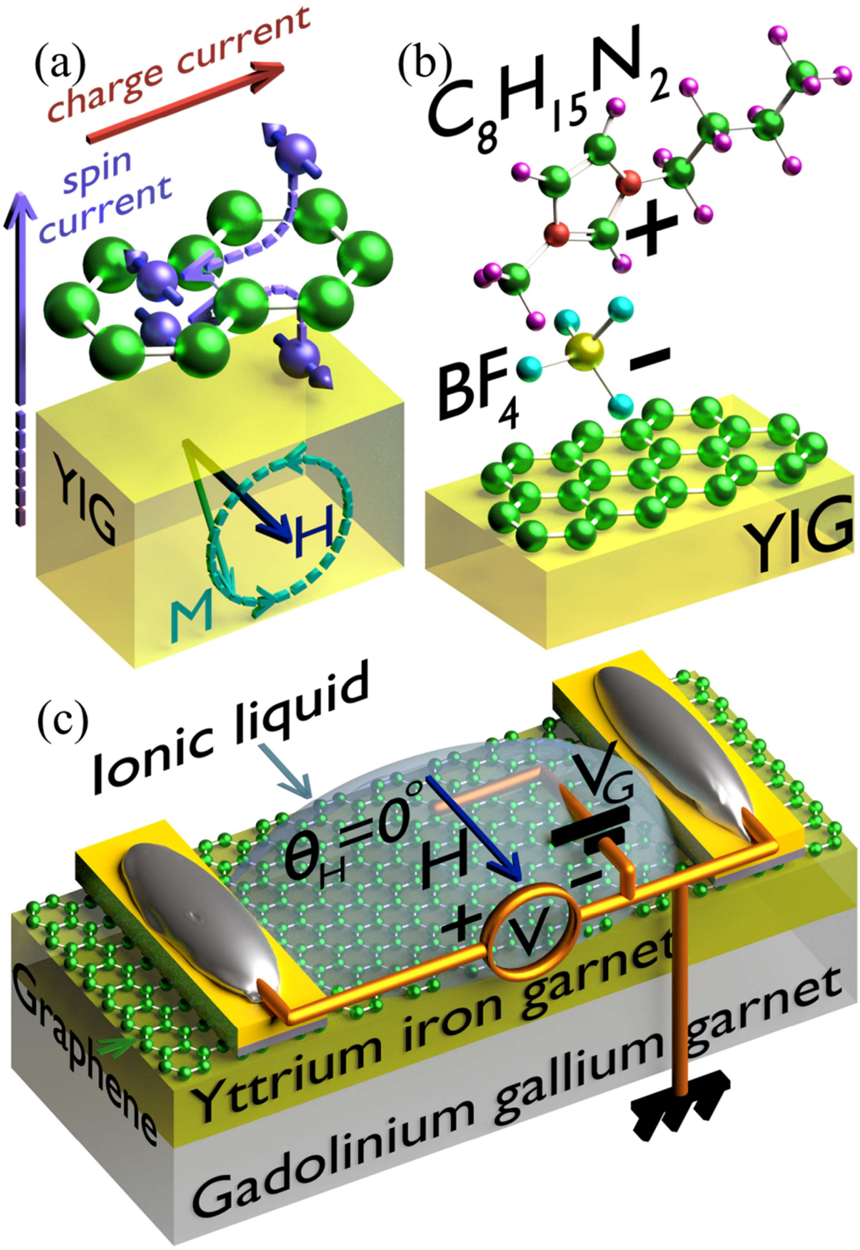

Figure 3-1. (a) Under the FMR pure spin current was transferred through the YIG/SLG interface. The pure spin current in the SLG was converted into an in-plane charge current. **(b)** Schematic view of an electric gate using ionic liquid placed on top of the SLG. **(c)** Layout of the spin-charge conversion experiment in the YIG/SLG sample. The generated voltage was detected from the Ti/Au contact pads.

3.3.3 Measurement procedure

For the measurement sample was placed on a quartz rod using double-side adhesive tape and mounted inside the TE_{011} cavity of a JES-FA200 electron spin resonance spectrometer with a microwave frequency f = 9.12 GHz. The electromotive force from the sample was detected using a KEITHLEY 2182A Nanovoltmeter. A gate voltage V_G was applied using a KEITHLEY 2400 SourceMeter. The measurement procedure was as follows. The sample was cooled to 250 K, and V_G value was set. After waiting for 10 min for the development of the electric double layer at the SLG/ionic liquid interface (with gate current I_G becoming less than 1 nA, signifying the end of the polarization process in the ionic liquid), the system was cooled to 200 K. At 200 K, spin pumping measurements at microwave power P_{MW} = 4 mW were performed. Temperature was controlled via a liquid nitrogen variable temperature unit ES-DVT 4 with an accuracy of ± 0.5 K. To change V_G, the system was heated to 250 K, and the entire procedure was repeated. The I_D-V_G curve measurements were performed using an AGILENT 4156C Precision Semiconductor Parameter Analyzer. The temperature was maintained at T = 250 K, with a V_G sweeping rate of 0.5 mV/s. This allowed polarization of the electric double layer to follow the slow V_G sweeping. During the I_D-V_G measurements, I_G was below 10 nA and was at least 10^3 times smaller than I_D. Temperature dependence of the SLG resistivity was very weak, with resistivity decreasing by less than 2% from 250 K to 200 K. Raman spectra were measured with a confocal Raman spectroscope with 532 nm laser excitation (Tokyo Instruments, Nanofinder 30) (Note: Raman spectra were measured by the author's collaborators Prof. H. Ago and K. Kawahara from the Carbon Electronics Group, Institute for Materials and Chemical Research, Kyushu University, Japan; analysis of the Raman spectra data was carried by the author himself).

3.4 Experimental results and discussion

3.4.1 Raman spectroscopy

The author now proceeds to the experimental results. The author used high-quality SLG grown by chemical vapor deposition using an atomically flat epitaxial Cu(111) thin film[129]. Figure 3-2 shows the typical Raman spectra of the SLG after transfer on the SiO_2 (red line) and YIG (purple line) substrates. Blue and green lines show Raman spectrum of YIG before single layer graphene transfer and difference

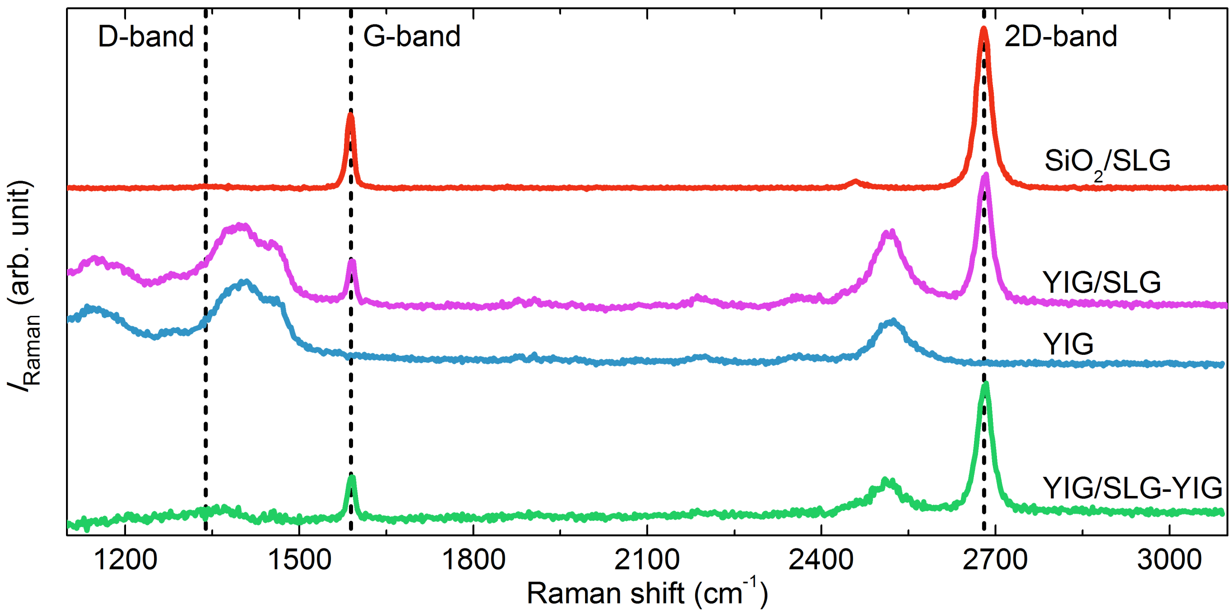

Figure 3-2. The Raman spectra of the YIG substrate without single layer graphene (blue line), YIG/SLG (purple line), difference Raman spectrum YIG/SLG–YIG (green line), and reference Si/SiO$_2$/SLG (red line) samples. Both SLG were grown in the same batch and were afterwards transferred to the designated substrates.

Raman spectrum YIG/SLG–YIG, respectively. The SiO$_2$/SLG and YIG/SLG–YIG Raman spectra showed sharp G and 2D-bands with a high relative intensity (I_{2D}/I_G) > 2. In addition, D-band at 1340 cm^{-1}, which originates in the structural defects and edges, was negligible. These results confirmed the growth and successful transfer of high-quality SLG. Residual peak from YIG substrate at 2520 cm^{-1} is present in the difference spectrum due to change in the intensity of the YIG bands between YIG and YIG/SLG samples.

3.4.2 Ferromagnetic resonance measurements

3.4.2.1 Ferromagnetic resonance spectra fitting

Experimentally detected derivative FMR spectra d$I(H)$/dH were integrated, and resulting $I(H)$ spectra were fitted using function:

$$I(H) = I_{\mathrm{Sym}} \frac{G_{\mathrm{Sym}}^2}{\mu_0^2 (H - H_{\mathrm{FMR}})^2 + G_{\mathrm{Sym}}^2} + I_{\mathrm{Asym}} \frac{-2 G_{\mathrm{Asym}} \mu_0 \left(H - H_{\mathrm{Asym}}\right)}{\mu_0^2 \left(H - H_{\mathrm{Asym}}\right)^2 + G_{\mathrm{Asym}}^2} + \mathrm{a} \mu_0^2 (H - H_{\mathrm{FMR}})^2 + \mathrm{b} \mu_0 (H - H_{\mathrm{FMR}}) + \mathrm{c},$$

where the second term describes asymmetry in the spectrum caused by the magnetostatic surface waves at ($H < H_{\mathrm{FMR}}$) and magnetostatic backward volume waves at ($H > H_{\mathrm{FMR}}$), and last three terms are quadratic background term (comes from integrating of the linear background in the derivative FMR spectrum) (Figs. 3-3(a) and 3-3(b)).

However, fitting using standard function:

$$I(H) = I_{\mathrm{Sym}}\frac{G^2}{\mu_0^2(H-H_{\mathrm{FMR}})^2+G^2} + I_{\mathrm{Asym}}\frac{-2G\mu_0(H-H_{\mathrm{FMR}})}{\mu_0^2(H-H_{\mathrm{FMR}})^2+G^2} + \mathrm{a}\mu_0(H-H_{\mathrm{FMR}}) + \mathrm{b},$$

produced closely same results. If performed multiple times on the data, fitting results always converged to the same values. While spin waves can greatly affect the microwave absorption spectrum, their influence on electromotive force is lesser due to smaller spin pumping efficiency comparing to the uniform FMR mode, especially for backward volume modes[53,130].

3.4.2.2 Ferromagnetic resonance measurement under top gate voltage application

Figures 3-4(c) and 3-4(d) show the FMR spectrum with the external magnetic field applied in the plane of the sample surface. Microwave magnetic field *h* excited resonances in the FMR spectrum

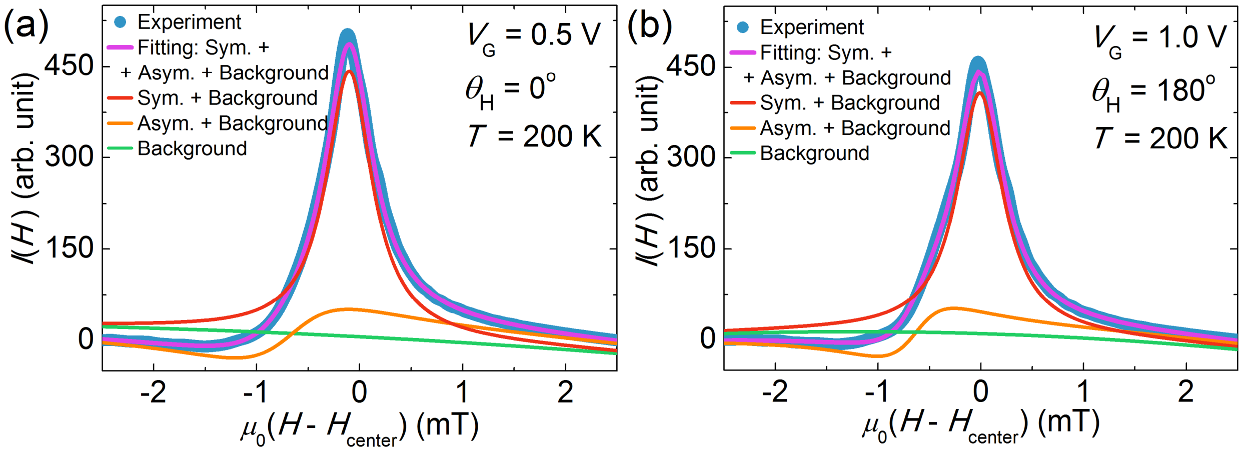

Figure 3-3. Fitting of the microwave absorption spectrum $I(H)$ measured at microwave power P = 4 mW, T = 200 K. **(a)** gate voltage V_{G} = 0.5 V, external magnetic field was applied in the θ_H = 0° direction, **(b)** gate voltage V_{G} = 1.0 V, external magnetic field was applied in the θ_H = 180°. Blue filled circles—experimental data, purple line—fitting by the equation described in the section 3.4.2.1. Orange line shows asymmetric contribution due to the presence of the magnetostatic surface and backward volume waves. Red and green lines show symmetric contribution and background, respectively.

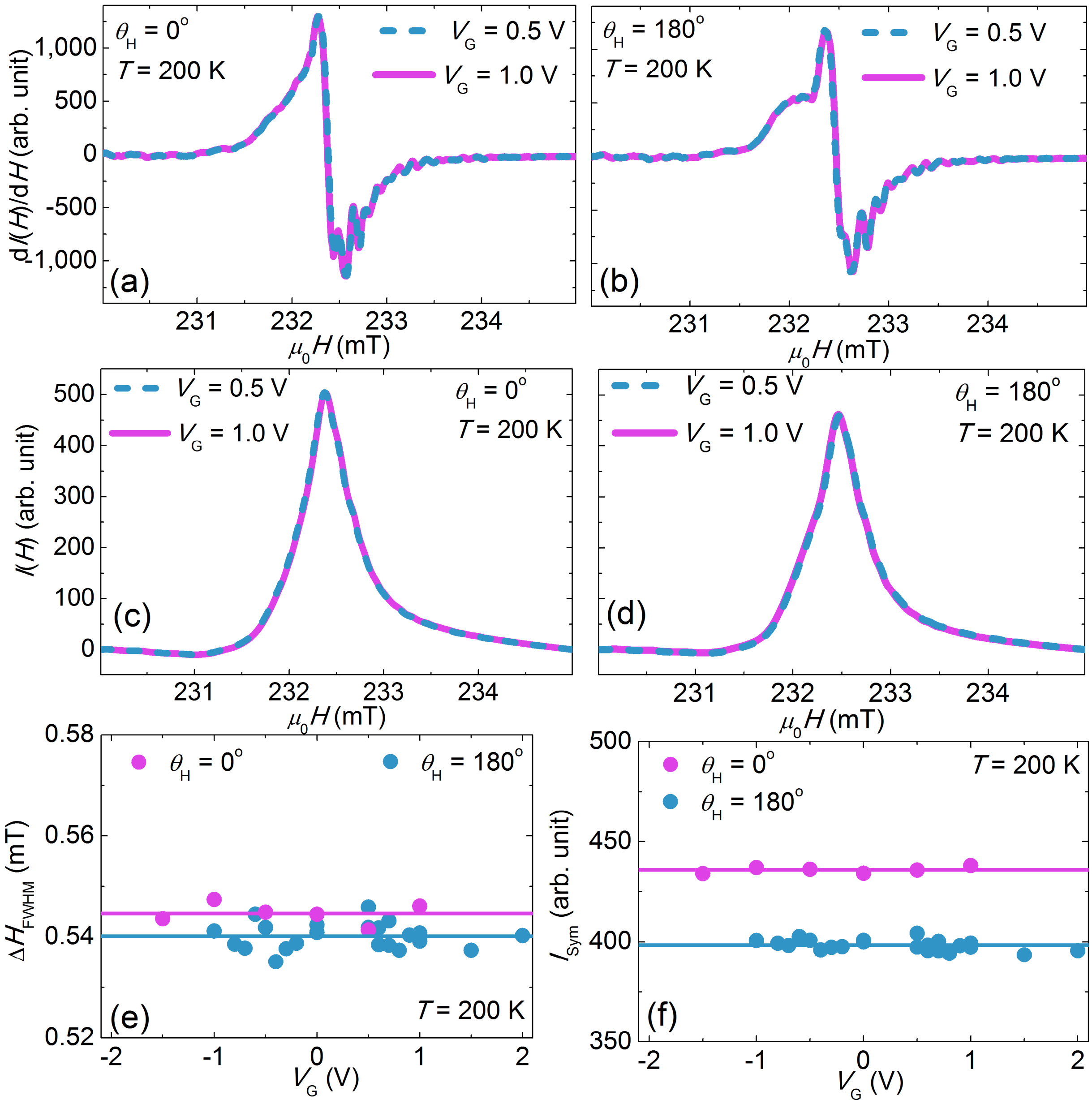

Figure 3-4. Derivative FMR spectra dI/dH **(a,b)** and FMR spectra $I(H)$ **(c,d)** under gate voltage application V_G = 0.5 V (blue dashed line) and V_G = 1.0 V (purple line) for θ_H = 0° **(a,c)** and θ_H = 180° **(b,d)**. The FMR full width at half maximum ΔH_{FWHM} **(e)** and the FMR amplitude I_{Sym} **(f)** dependence on the gate voltage V_G. Lines and solid circles represent the fitting by the constant and experimental data, correspondingly. Additional resonances in the derivative FMR spectra and asymmetry in the FMR spectra are caused by the magnetostatic surface waves at ($H < H_{FMR}$) and magnetostatic backward volume waves at ($H > H_{FMR}$).

through coupling to the magnetostatic spin-waves in the YIG layer. The peak of the absorbance spectrum at H_{FMR} corresponds to the fundamental wave mode with $k = 0$, which is equivalent to the uniform FMR mode in the ferromagnetic layers. Slight asymmetry of the absorbance spectrum in the in-plane external magnetic field configuration was caused by magnetostatic surface waves at $H < H_{\mathrm{FMR}}$ and magnetostatic backward volume waves at $H > H_{\mathrm{FMR}}$[131,132]. From the FMR spectrum, the saturation magnetization of YIG was $\mu_0 M = 0.169$ T at room temperature (using g-factor $g = 2.046$ [29]), which agrees well with the values reported for YIG films in the literature[29,132]. The saturation magnetization at the temperature of spin pumping measurements ($T = 200$ K) was $\mu_0 M = 0.204$ T, which was in accordance with a temperature dependence of $\mu_0 M$ from Neel's two-sublattice model[133]. Though in metallic ferromagnet systems the bias voltage can influence the spin pumping efficiency through the control of the depletion region and Schottky barrier height, spin pumping from the ferrimagnetic insulator with large 2.7 eV bang gap is free of this problem. Additionally, the author measured linear *I-V* curve at room and low temperatures, ruling out presence of any energy barriers at the Au/Ti/SLG interface. Thus, spin current injection and FMR spectrum are expected to be independent of gate voltage. Detected derivative FMR and FMR absorbance spectra (Figs. 3-4(a,b,c,d)) were identical for 0.5 V (dashed blue line) and 1.0 V (purple line). The drain current I_{D} showed strong V_{G} dependence, confirming the carrier density modulation and switching of the carrier type from holes to electrons (see Fig. 3-6(a)). In contrast, both the FMR full width at half maximum ΔH_{FWHM} (Fig. 3-4(e)) and the FMR amplitude I_{Sym} (Fig. 3-4(f)), obtained from the fitting of the FMR spectrum, were independent of V_{G} and lied in the range: $\mu_0 \Delta H_{\mathrm{FWHM}}^{0^\circ} = 0.545$ mT ($^{+0.5}_{-0.6}$ %), $\mu_0 \Delta H_{\mathrm{FWHM}}^{180^\circ} = 0.540$ mT ($^{+1.1}_{-0.9}$ %), $I_{\mathrm{Sym}}^{0^\circ} = 436$ arb. unit ($^{+0.5}_{-0.4}$ %), and $I_{\mathrm{Sym}}^{180^\circ} = 398$ arb. unit ($^{+1.5}_{-1.2}$ %). The small difference in the FMR at the opposite directions of external magnetic field was caused by differences in the spin wave resonances due to slightly different sample position at $\theta_{\mathrm{H}} = 0°$ and $\theta_{\mathrm{H}} = 180°$.

3.4.2.3 Spin pumping contribution to the Gilbert damping constant

Enhancement of the Gilbert damping due to the FMR mode spin pumping was predicted to be inversely proportional to the thickness of the magnetic insulator film[44,59]. This effect originates from the fact that total magnetic moment of ferromagnet decreases together with its thickness, thus it becomes more sensitive to the transfer of angular momentum at the interface. Peak-to-peak width ΔH_{pp} of derivative FMR spectrum $\mathrm{d}I(H)/\mathrm{d}H$ is proportional to the Gilbert damping α:

$$\Delta H_{\mathrm{pp}} = \frac{\Delta H_{\mathrm{FWHM}}}{\sqrt{3}} = \frac{4\pi}{\sqrt{3}}\frac{\alpha f}{\gamma},$$

where ΔH_{FWHM} is full width at half maximum of the FMR, f is microwave frequency, and γ is the gyromagnetic ratio. In agreement with theoretical prediction in YIG/Pt spin pumping experiments increase in the $\mu_0\Delta H_{\mathrm{pp}}^{\mathrm{YIG/Pt-YIG}} = \mu_0\Delta H_{\mathrm{pp}}^{\mathrm{YIG/Pt}} - \mu_0\Delta H_{\mathrm{pp}}^{\mathrm{YIG}}$ was measured to be 2.4 mT for d_{YIG} = 20 nm, f = 9.65 GHz[37], but only 0.12 mT for d_{YIG} = 96 nm, f = 10 GHz[134]. Thus, for the YIG/Pt one expects upper limit of FMR broadening due to spin pumping for d_{YIG} = 2 μm, f ~ 9-10 GHz to be $\mu_0\Delta H_{\mathrm{pp}} < 0.005$ mT. In contrast to other nonmagnetic materials, Pt layer thicker than 10 nm behaves as almost perfect spin sink. Thus, upper limit for ΔH_{pp} is expected to be even smaller in YIG/nonmagnetic systems where spin orbit interaction weaker than in Pt (including studied in this chapter case of SLG). Taking into account that microwave absorbance spectra of 2 μm YIG are complicated by the presence of the additional spin wave resonances, ΔH_{pp} broadening due to spin pumping on the order of 10^{-3} mT is below detection limit in electron spin resonance system used by the author. However, real part of spin mixing conductance $g_{\uparrow\downarrow}$, which governs spin current injection, is proportional to the $\Delta\alpha \cdot d_{\mathrm{YIG}}$, thus effective spin pumping is possible despite very small $\Delta\alpha$.

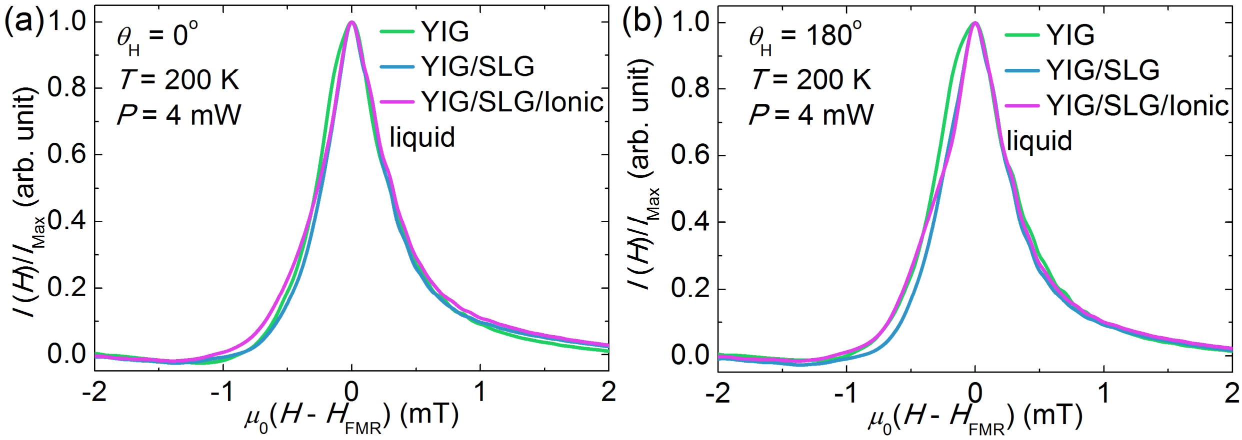

Figure 3-5. Normalized microwave absorbance spectra for the YIG, YIG/SLG and YIG/SLG/Ionic liquid samples (green, blue and purple lines, respectively). Contribution from magnetostatic surface waves caused difference in the spectra at $H < H_{\mathrm{FMR}}$. External magnetic field was applied in the **(a)** θ_H = 0° and **(b)** θ_H = 180° direction.

Figure 3-5 shows normalized FMR spectra for YIG, YIG/SLG and YIG/SLG/Ionic liquid (green, blue and purple lines, correspondingly). In agreement with the previous discussion, peak-to-peak widths of the FMR spectra obtained from the fitting were closely the same: $\mu_0\Delta H_{\mathrm{pp}}^{\mathrm{YIG}}$ = 0.32 mT, $\mu_0\Delta H_{\mathrm{pp}}^{\mathrm{YIG/SLG}}$ = 0.30 mT, $\mu_0\Delta H_{\mathrm{pp}}^{\mathrm{YIG/SLG/Ionic\ liquid}}$ = 0.31 mT. In contrast to backward volume and FMR modes, surface waves modes are sensitive to interface condition even for thick d_{YIG} = 2 μm films. In the in-plane external magnetic field configuration, right shoulder of the FMR ($H > H_{\mathrm{FMR}}$) is modulated by magnetostatic backward volume waves, while left shoulder ($H < H_{\mathrm{FMR}}$)—by the magnetostatic surface waves. Thus, at $H > H_{\mathrm{FMR}}$ YIG, YIG/SLG and YIG/SLG/IL spectra were nearly identical, but at $H < H_{\mathrm{FMR}}$ difference was more pronounced and caused by magnetostatic surface waves (Figs. 3-5(a) and 3-5(b)).

3.4.3 Electrical measurements

3.4.3.1 Electromotive force generated under ferromagnetic resonance

Next, the author discusses electrical response of the YIG/SLG under gate voltage application. It was shown that spin current generated through the spin Hall effect can be used to switch magnetization in spin-torque devices[33]. However, until the present, sign of the generated spin and charge current could only be changed by reversal of the magnetic field or source current. Fig. 3-6(a) shows the dependence of the drain current I_{D} between Ti/Au terminals under sweep of the gate voltage V_{G} for the YIG/SLG structure. The minimum of the I_{D} curve represents the position of the Dirac point in the V_{G} sweep. Figures 3-6(b) and 3-6(c) show the detected electromotive force under the FMR conditions and application of gate voltage. The generated spin current, i.e., transferred angular momentum from YIG to SLG, is proportional to the area swept by the YIG magnetization during the precession. Thus, spin current has maximum at the FMR field H_{FMR}: at which microwave power absorption and precession angle are the largest. As a result, electromotive force generated through the spin-charge conversion has a symmetrical shape with respect to the H_{FMR}. The measured voltage signals were deconvolved into symmetrical V_{Sym} and V_{Asym} contributions using the Lorentzian functions[20]. The small asymmetric contribution V_{Asym} to the voltage signal may have arisen from spurious effects, which include thermal effects. At V_{G} = 0.5 V (blue filled circles in figures 3-6(b) and 3-6(c)) the Fermi level in SLG was tuned below the Dirac point, where holes acted as a dominant carrier. When V_{G} was tuned to 1.0 V (purple filled circles in figures 3-6(b) and 3-6(c)) the

Fermi level crossed the Dirac point, and the carrier type was changed from holes to electrons. The change in the carrier type was accompanied by switching of the voltage signal sign for both $\theta_H = 0°$ and $\theta_H = 180°$ directions of the external magnetic field. Thus, a gate voltage can be used to switch sign of the charge current generated through SOI.

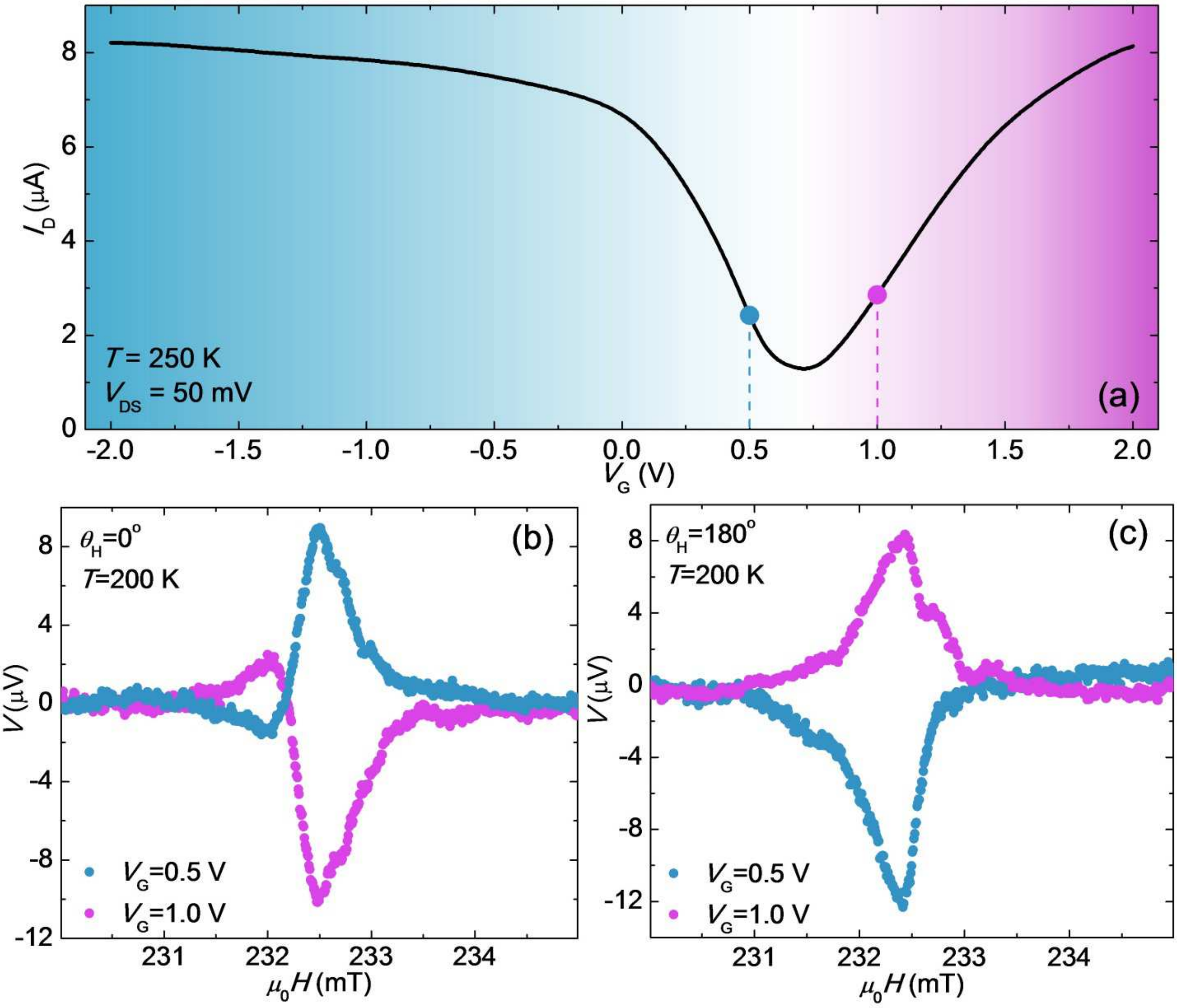

Figure 3-6. (a) I_D-V_G measurement at T = 250 K. In the blue area, the carrier type is holes; in the purple area, the carrier type is electrons. Generated voltage under the FMR and application of the gate voltage V_G = 0.5 V (blue filled circles) and V_G = 1.0 V (purple filled circles) for the direction of the external magnetic field ***H*** $\theta_H = 0°$ **(b)** and $\theta_H = 180°$ **(c)**.

3.4.3.2 Electromotive force fitting

Electromotive force was fitted with the standard Lorentzian function used in the ISHE experiments[20]:

$$V(H) = V_{\mathrm{Sym}}\frac{\Gamma^2}{\mu_0^2(H-H_{\mathrm{FMR}})^2+\Gamma^2} + V_{\mathrm{Asym}}\frac{-2\Gamma\mu_0(H-H_{\mathrm{FMR}})}{\mu_0^2(H-H_{\mathrm{FMR}})^2+\Gamma^2} + a\mu_0(H-H_{\mathrm{FMR}}) + b,$$

where the first term expresses electromotive force due to ISHE (even with respect to $H - H_{\mathrm{FMR}}$), second term—electromotive force due to spurious effects, including anomalous Hall effect (odd with respect to $H - H_{\mathrm{FMR}}$), last two terms—background voltage (Figs. 3-7(a) and 3-7(b)). For example, dip in the electromotive force in Fig. 3-7(a) at $\mu_0(H - H_{\mathrm{center}}) = -0.5$ mT in the fitting is included inside the second term for the spurious contributions (orange line in Fig. 3-7(a)). This is supported by the fact that dip is not reversed between $\theta_H = 0^{\circ}$ and $\theta_H = 180^{\circ}$ (see blue and purple filled circles in Figs. 3-6(b) and 3-6(c)). Thus, this dip doesn't possess the symmetry of the ISHE on the reversal of the external magnetic field direction.

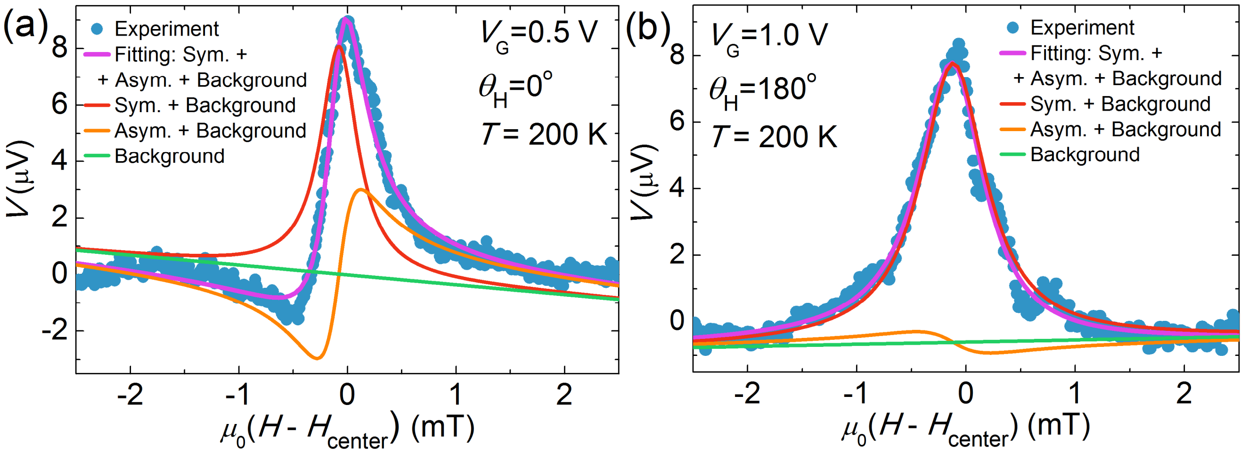

Figure 3-7. Fitting of the generated electromotive force at microwave power P = 4 mW, T = 200 K. **(a)** gate voltage V_G = 0.5 V, external magnetic field was applied in the θ_H = 0° direction, **(b)** gate voltage V_G = 1.0 V, external magnetic field was applied in the θ_H = 180° direction. Blue filled circles—experimental data, purple line—fitting by the equation from the section 3.4.3.2. Orange line shows asymmetric contribution due to due to spurious effects. Red and green lines show symmetric contribution and background, respectively.

Electromotive force without thermal contributions can be calculated by subtracting voltage for the opposite directions of external magnetic field ***H***. Figure 3-8 shows (V(θ_H = 0^o) – V(θ_H = 180^o))/2 for V_G = 0.5 V (purple filled circles) and V_G = 1.0 V (blue filled circles). Symmetrical shape of the signal means that ISHE in the studied system is dominant over other contributions, such as recently discovered anomalous Hall effect in the YIG/graphene system, which is caused by the magnetic proximity effect[135].

Finally, another common way to quantify ISHE—especially in cases when symmetrical shape of voltage signal is distorted and fitting is difficult—is to use peak height of the voltage signal. The author carried out same analysis using the height of voltage peak, instead of the voltage obtained from the fitting, and came to the same quantitative conclusions. The averaged (over all data) ISHE voltage difference between two methods was $\left\langle\left|\frac{V_{\mathrm{ISHE}}^{\mathrm{Peak\ height}}-V_{\mathrm{ISHE}}^{\mathrm{Fitting}}}{V_{\mathrm{ISHE}}^{\mathrm{Peak\ height}}}\right|\right\rangle$ = 6.1%. The author stresses that method used for analysis doesn't affect results reported in the chapter.

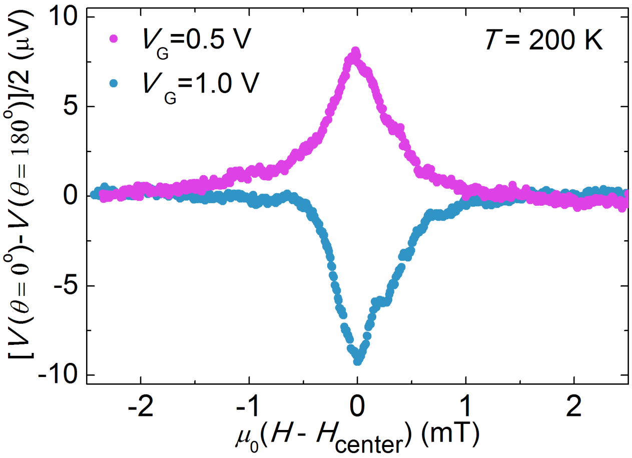

Figure 3-8. Electromotive force (V(θ_H = 0^o) – V(θ_H = 180^o))/2 at T = 200 K for V_G = 0.5 V and V_G = 1.0 V (purple and blue filled circles, respectively). After subtraction of the electromotive force for opposed direction of the external magnetic field, signal has clear symmetric shape as expected from the ISHE system.

3.4.3.3 Polarization hysteresis of the ionic liquid

Ionic liquid is a salt in a liquid state, meaning that it mostly consists of cations and anions, in contrast to ordinary liquids of electrically neutral molecules. Under application of gate voltage V_G, an electric double layer was formed near the YIG/SLG interface. Ionic liquid consisted of the positively charged $C_8H_{15}N_2^+$ and negatively charged ionic group BF_4^-, with the charged parts of the cation and anion separated by nonpolar alkyl chains (Fig. 3-9). Figure 3-10 shows the voltage sweeping hysteresis of the polarization process of the ionic liquid. The polarization process of ionic liquid for the voltage upsweep (from negative to positive V_G) and downsweep (from positive to negative V_G) was different due to the presence of the energy barriers during reorganization of the electric double layer structure (analogy can be made to the magnetic hysteresis under the sweeping of a magnetic field)[136,137]. This hysteresis resulted in the different position of the Dirac point for the up and down voltage sweeps, $V_{\mathrm{DP}}^{\mathrm{up}} \neq V_{\mathrm{DP}}^{\mathrm{down}}$. Switching of the signal sign followed this hysteresis, thus following Dirac point (Fig. 3-10). To avoid shifting of the Dirac point the author used only data from the upsweep measurements in the analysis.

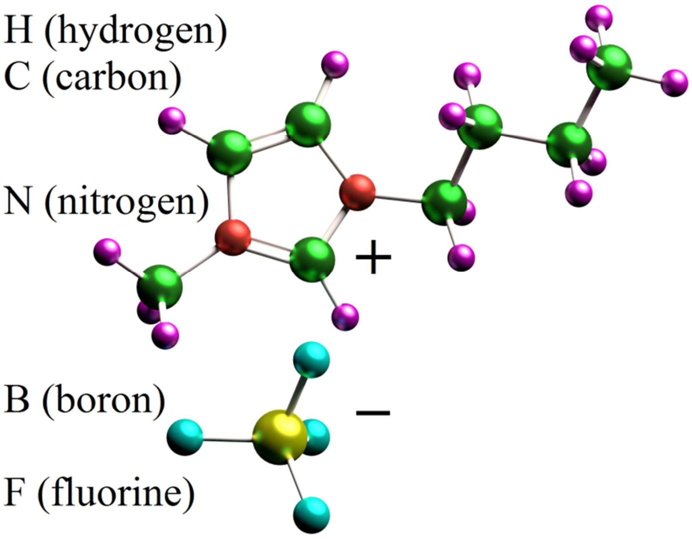

Figure 3-9. Structure of the ionic liquid: positively charged $C_8H_{15}N_2^+$ and negatively charged ionic group BF_4^-. Under application of the voltage ionic liquid acts as a gate on top of the SLG due to formation of the electric double layer near the YIG/SLG interface.

3.4.3.4 Electromotive force under top gate voltage application

One of the points of interest of the experimental system studied by the author was that the spin-charge conversion of the spin-pumped current allowed differentiation between device states with hole and electron conduction. In contrast to common field-effect transistor devices, where by using an electric gate, only one “on” state and one “off” state can be achieved, the device studied by the author showed three different states: two “on” states and one “off” state. The “off” state was achieved by tuning the Fermi level to the Dirac point using gate voltage V_G. The two “on” states were characterized by positive or negative voltage output, corresponding to a Fermi level below or above the Dirac point (Fig. 3-10). The achieved ratio between the “on” and “off” states was ~10 (it should be approximately 10^3 for implementation in real devices), however, it can readily be improved by implementing other than ionic liquid top gate layer, which will allow more precise tuning to the Dirac point.

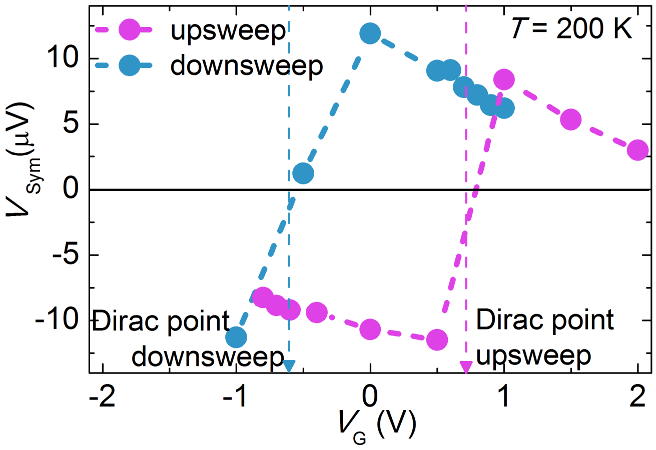

Figure 3-10. The polarization process of the ionic liquid for the voltage upsweep (from negative to positive V_G) and downsweep (from positive to negative V_G) was different, resulting in $V_{DP}^{up} \neq V_{DP}^{down}$. Switching of the voltage sign generated under FMR occurred at the Dirac point for both the upsweep and downsweep. The position of the Dirac point in the upsweep V_{DP}^{up} and downsweep $V_{DP}^{down}$was determined from the I_D-V_G measurements at T = 250 K. During the FMR measurements, an external magnetic field was applied in the θ_H = 180° direction. Dashed lines are a guide to the eye.

In figure 3-11(a) the gate voltage dependence of V_{Sym} for two external magnetic field $\boldsymbol{H}$ directions $\theta_H = 0°$ (purple filled circles) and $\theta_H = 180°$ (blue filled circles) is shown. Using the resistance determined from the I_D-V_G measurements and the detected voltage V_{Sym}, the author extracted the charge current I generated in the YIG/SLG system. Contributions to the spin-charge conversion current from holes and electrons have opposite polarities. Hence, the charge current generated in the SLG was described by the following relation: $I = I_S(n_h - n_e)/(n_h + n_e)$, where $I_S = \lim_{V_G \to -\infty} I(V_G)$ is the charge current when the Fermi level is tuned far below Dirac point. Under the assumption that the carrier type is switched from holes to electrons at the Dirac point, the dependence of the carrier type n_{Type} on the gate voltage is described by $n_{\mathrm{Type}} = -\,\mathrm{sgn}(V_G - V_{DP})$, where $n_{\mathrm{Type}} = 1$ corresponds to the hole carrier type and $n_{\mathrm{Type}} = -1$ corresponds to the electron carrier type. However, due to fluctuations of the Fermi level in devices, both electrons and holes are present near the Dirac point (phenomenon known as electron-hole puddles). To take into account presence of the electron-hole puddles near the Dirac point, the author assumed the following

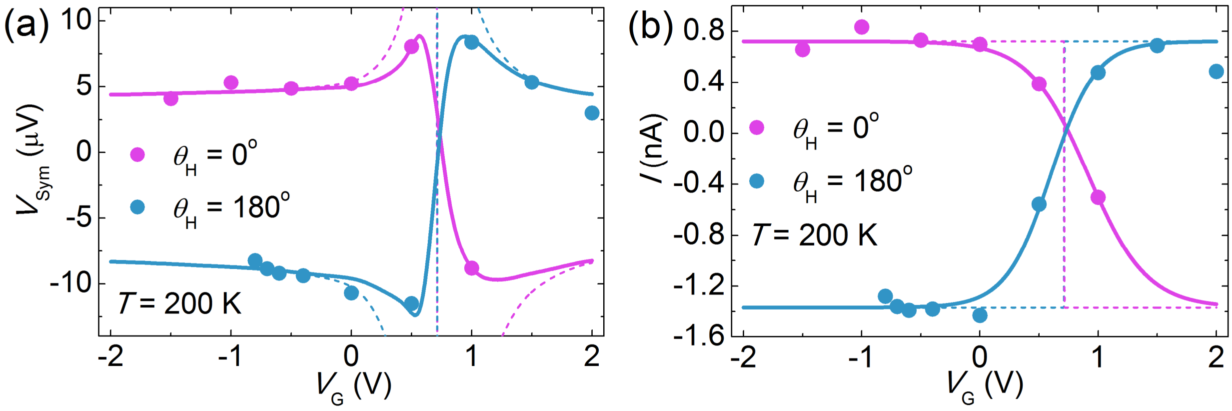

Figure 3-11. V_{Sym} **(a)** and spin-charge conversion current **(b)** dependence on the gate voltage V_G for the direction of the external magnetic field $\boldsymbol{H}$ $\theta_H = 0°$ (black filled circles) and $\theta_H = 180°$ (red filled circles). Lines show the fitting that takes into account the presence of the electron-hole puddles near the Dirac point (solid lines) and the fitting using a simple one carrier type model (dashed lines).

distribution of the normalized electron and hole carrier densities near the Dirac point: $\frac{n_\mathrm{h}}{n_\mathrm{h}+n_\mathrm{e}} = \frac{1}{e^{(V_\mathrm{G}-V_\mathrm{DP})/a}+1}$ and $\frac{n_\mathrm{e}}{n_\mathrm{h}+n_\mathrm{e}} = \frac{e^{(V_\mathrm{G}-V_\mathrm{DP})/a}}{e^{(V_\mathrm{G}-V_\mathrm{DP})/a}+1}$. The generated charge current consisted of two components: the contribution from the spin pumping I_S, which reverses its sign at the reversal of the external magnetic field from $\theta_H = 0°$ to $\theta_H = 180°$, and thermal component I_Th from the heating effects, which was independent of the magnetic field direction. The parameters (V_DP, a), dependent on ionic-gating, can vary to some extent in different sweeps of the gate voltage (for $\theta_H = 0°$ and $\theta_H = 180°$) due to structural changes in the electric double layer of the ionic liquid. However, the charge current parameters, I_S and I_Th, are independent of the ionic-gate sweep, because they are determined by the spin pumping efficiency, which is independent of V_G. From the fitting of the experimental data the author obtained values $I_\mathrm{S} = 1.05$ nA, $I_\mathrm{Th} = 0.32$ nA, $V_\mathrm{DP}^{\theta_\mathrm{H}=0°} = 0.9$ V, $a^{\theta_H=0°} = 0.25$ V, $V_\mathrm{DP}^{\theta_H=180°} = 0.6$ V, and $a^{\theta_H=180°} = 0.19$ V. Figures 3-11(a) and 3-11(b) shows experimental data fitting by model with the switching of the single carrier type at the Dirac point (dashed lines) and model with electron-hole puddle transition (solid lines).

3.4.3.5 Back gate voltage measurements of conductivity

Cu wire with diameter 100 μm—that was used to apply top gate voltage in YIG/SLG/Ionic liquid system—acted as a second capacitor in series. Since it has small capacity that author can't estimate precisely, the Fermi level position cannot be determined directly from the applied top gate voltage. The author applied back gate voltage measurements to calculate Fermi level position as a function of conductivity for the SLG samples used in the author's. SLG was transferred on top of $d_\mathrm{SiO2} = 300$ nm thick SiO$_2$ layer with sheet capacitance $C_{\mathrm{SiO}_2} = \frac{\epsilon_0\epsilon_{\mathrm{SiO}_2}}{d_{\mathrm{SiO}_2}} = 0.0115$ μF·cm^{-2}, where $\epsilon_{\mathrm{SiO}_2} = 3.9$ is relative permittivity of SiO$_2$, and $\epsilon_0 = 8.85\times10^{-12}$ F·m^{-1} is vacuum permittivity. Figure 3-12(a) shows dependence of the sheet conductance σ_S of the SLG under the back gate voltage V_BG sweep from -30 to 30 V. Quantum capacitance of the SLG, which is connected in series to C_{SiO_2}, can be estimated as $C_\mathrm{Q} = \mathrm{e}^2\left(\frac{dn_\mathrm{S}}{dE}\right)_{E=E_F}$, where e = 1.6×10^{-19} C is elementary charge. Sheet carrier density in SLG is given by $n_\mathrm{S}\,(\eta_\mathrm{F}) = \frac{2(k_\mathrm{B}T)^2}{\pi(\hbar v_\mathrm{F})^2}\Gamma(2)(F_1(\eta_\mathrm{F}) - F_1(-\eta_\mathrm{F}))$, where $F_S(\eta_\mathrm{F}) = \frac{1}{\Gamma(s+1)}\int_0^\infty \frac{\varepsilon^S d\varepsilon}{1+\exp(\varepsilon-\eta_\mathrm{F})}$ is the complete Fermi-Dirac integral, $\eta_\mathrm{F} = \frac{E_\mathrm{F}}{k_\mathrm{B}T}$, $\epsilon = \frac{E}{k_\mathrm{B}T}$, E_F—Fermi level position, $k_\mathrm{B} = 1.38\times10^{23}$ J·K^{-1}—Boltzmann constant, $\hbar = 1.06\times10^{-34}$ J·s—reduced Planck constant, $v_\mathrm{F} = 10^6$ m·s^{-1}—Fermi velocity, Γ—the gamma function. Using the above, the author estimated lower bound for quantum capacitance of SLG $C_Q = \frac{2k_B T e^2}{\pi(\hbar v_F)^2}\Gamma(2)(F_0(\eta_F) + F_0(-\eta_F))$ to be $C_Q = 0.827$ µF·cm^{-2} at $E_F = 0$ eV, which is almost two orders larger than $C_{SiO_2} = 0.0115$ µF·cm^{-2}. At E_F = 0.1 eV difference is even more pronounced with $C_Q = 2.37$ µF·cm^{-2}. Thus, one can safely neglect quantum capacitance, and convert applied back gate voltage V_{BG} into the sheet carrier density $n_S = \frac{C_{SiO_2}}{e}(V_{BG} - V_{DP})$. Far from the Dirac point sheet conductance of the SLG in the diffusive regime can be calculated in the zero temperature approximation: $\sigma_S = \frac{2e^2}{h}\frac{2|E_F|}{\pi\hbar v_F}\lambda$, where $E_F = \mathrm{sign}(n_S)\hbar v_F\sqrt{\pi n_S}$, and λ is the mean free path. Figures 3-12(a) and 3-12(b) show experimentally measured (blue filled circles) and calculated (purple line) sheet conductance of the SLG, with $\lambda = 27.3$ nm obtained from the fitting. From $|E_F| = \frac{h}{2e^2}\frac{\sigma_S \pi\hbar v_F}{2\lambda}$ the author estimated that Fermi level was changed from – 0.11 eV to 0.11 eV range under the application of top gate voltage from – 1.5 V to 2.0 V.

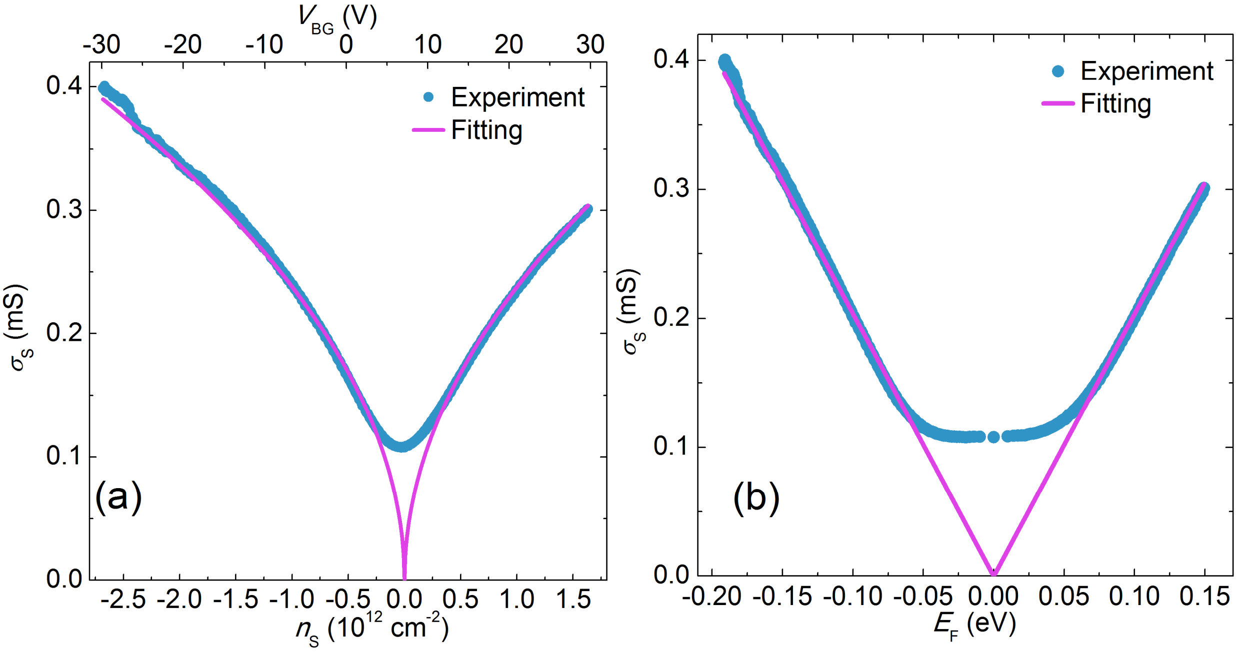

Figure 3-12. Dependence of the sheet conductance of the SLG of the Si/SiO$_2$/SLG sample on the **(a)** back gate voltage, **(b)** Fermi level position. Blue filled circles are experimental data, purple lines show theoretically estimated sheet conductance as described in the section 3.4.3.5.

3.4.4 Heating due to microwave absorption and nonlinear effects of FMR in YIG

Thermoelectric contribution can be present in YIG/single layer graphene system at FMR. If there is a thermal gradient along YIG substrate in the direction from one gold electrode to the other, then voltage generated by Seebeck effect in graphene would be measured along with ISHE electromotive force. Moreover, both effects change sign with carrier type. To separate two contributions the author reversed direction of the external magnetic field from $\theta_H = 0^{\mathrm{o}}$ to $\theta_H = 180^{\mathrm{o}}$. Under magnetic field reversal ISHE switches its sign, while thermoelectric voltage generated by Seebeck effect should remain unchanged. Figures 3-6(b) and 3-6(c) show switching of the voltage sign under magnetic field reversal (blue filled circles for $V_{\mathrm{G}} = 0.5$ V and purple filled circles for $V_{\mathrm{G}} = 1.0$ V). It indicates that in the studied by the author system electromotive force originates from ISHE, and not thermoelectric effect. In Fig. 3-8 the author excluded contributions independent of magnetic field by subtracting voltage for the opposite directions of external magnetic field: $(V(\theta_H = 0^{\mathrm{o}}) - V(\theta_H = 180^{\mathrm{o}}))/2$ ($V_{\mathrm{G}} = 0.5$ V—purple filled circles, $V_{\mathrm{G}} = 1.0$ V—blue filled circles). After subtraction procedure thermoelectric signal was removed from the voltage data, and large symmetrical shape of the signal means that ISHE in the studied system was dominant over other contributions.

Additionally—for any FMR-generated thermoelectric effect—time for which sample stays under the FMR affect total heat generated in the system. Thus, temperature gradient, along with generated voltage due to thermoelectric effects, will be changed with the sweeping rate of the magnetic field. The author didn't find any FMR or electromotive force dependence on the external magnetic field sweeping rate from 0.003 mT/s to 0.5 mT/s (Figs. 3-13(a) and 3-13(b)). Sample was under FMR condition ($\mu_0 H_{\mathrm{FMR}} \pm 0.5$ mT) from $t = 2$ s to $t = 360$ s (measurements were in the order from the shortest to longest sweeping time). Temperature dependence of saturation magnetization $\mu_0 M$ is described by Neel's two-sublattice model[133]. The FMR field H_{FMR} is related to the saturation magnetization of YIG layer by Kittel equation, and, thus, also temperature dependent. Using FMR field at 180 K and 220 K ($\mu_0 H_{\mathrm{FMR}}^{180\,\mathrm{K}} = 230.4$ mT and $\mu_0 H_{\mathrm{FMR}}^{220\,\mathrm{K}} = 235.0$ mT, respectively) the author estimated temperature derivative of FMR field at 200 K to be $\left.\frac{\partial H_{FMR}}{\partial T}\right|_{T=200\,\mathrm{K}} = 0.12$ mTK^{-1}. The author converted shift of the FMR field with changing sweeping time t_{sweep} into temperature difference: $\Delta T(\mathrm{t}_{\mathrm{sweep}}) = \left(H_{\mathrm{FMR}}\big|_{t_{\mathrm{sweep}}=10\,\mathrm{s}} - H_{\mathrm{FMR}}(t_{\mathrm{sweep}})\right) \Big/ \left(\left.\frac{\partial H_{\mathrm{FMR}}}{\partial T}\right|_{T=200\,\mathrm{K}}\right)$ (Fig. 3-13(c)). Temperature of the sample didn't increase together with sweeping time. Small decrease in the temperature of ΔT = 0.2 K at large sweeping times is within measurements error.

For the measurements the author used small microwave power of 4 mW (while usual microwave

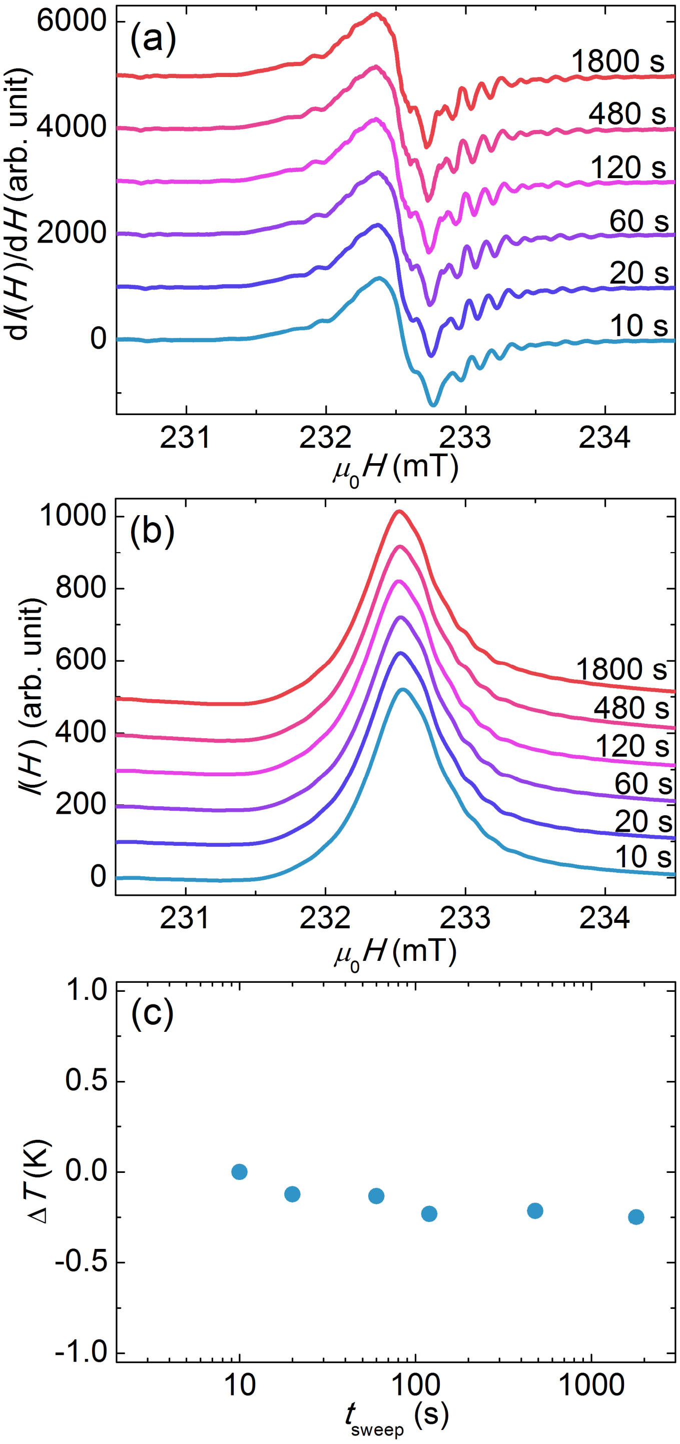

Figure 3-13. Sweep time dependence of the **(a)** derivative FMR dI(H)/dH and **(b)** FMR spectrum. **(c)** Temperature difference between the measurements with different sweeping time estimated from the shift of the FMR field.

powers in spin pumping experiments are on the order of hundreds mW) to avoid heating of the YIG substrate and dominance of the thermoelectric effects. Figure 3-14 shows power dependence of the FMR spectrum at $T = 200$ K. Linear dependence of the squared FMR amplitude on the microwave power shows that FMR was measured below power level for any saturation effects. Figure 3-15 shows FMR data from the sweep of external magnetic field from 0 to 300 mT. Single FMR peak without microwave absorbance at the half of the resonance field $H_{\mathrm{FMR}}/2$ confirms absence of the nonlinear parametric excitation and three-magnon splitting in the YIG layer. Finally, all measurements were performed under controlled temperature using nitrogen flow cooling, which should have effectively carried away any heat generated in the system.

3.4.5 Estimation of the spin Hall angle of single-layer graphene

The author prepared reference YIG/Pt sample and carried out inverse spin Hall effect measurements under the same conditions with YIG/SLG layer. Electromotive force was measured for the opposite directions of external magnetic field $\theta_{\mathrm{H}} = 0°$ and $\theta_{\mathrm{H}} = 180°$, and fitted using Lorentzian fitting function (see section 3.4.3.2 Electromotive force fitting). Inverse spin Hall effect voltage was calculated as $V_{\mathrm{ISHE}} = (V_{\mathrm{ISHE}}(\theta_H = 0°) - V_{\mathrm{ISHE}}(\theta_H = 180°))/2$. Following calculations in the[43,125], the author estimated spin Hall angle of SLG to be:

$$\theta_{\mathrm{SLG}} = \theta_{\mathrm{Pt}} \frac{V_{\mathrm{SLG}}\left(1 + \Gamma_{\mathrm{SLG}}^2 \tanh^2 \frac{d_{\mathrm{SLG}}}{\tilde{\lambda}_{\mathrm{SLG}}}\right)}{V_{\mathrm{Pt}}\left(1 + \Gamma_{\mathrm{Pt}}^2 \tanh^2 \frac{d_{\mathrm{Pt}}}{\lambda_{\mathrm{Pt}}}\right)} \frac{\frac{l_{\mathrm{Pt}}}{d_{\mathrm{Pt}}} \tanh \frac{d_{\mathrm{Pt}}}{\lambda_{\mathrm{Pt}}} \tanh \frac{d_{\mathrm{Pt}}}{2\lambda_{\mathrm{Pt}}}}{\frac{l_{\mathrm{SLG}}}{d_{\mathrm{SLG}}} \tanh \frac{d_{\mathrm{SLG}}}{\tilde{\lambda}_{\mathrm{SLG}}} \tanh \frac{d_{\mathrm{SLG}}}{2\tilde{\lambda}_{\mathrm{SLG}}}} = 3.5 \times 10^{-6},$$

where $V_{\mathrm{SLG}} = 2.0$ μV—inverse spin Hall effect voltage measured under 1 mW microwave power excitation in YIG/SLG sample, $d_{\mathrm{SLG}} = 0.34$ nm—thickness of the SLG layer, $l_{\mathrm{SLG}} = 2.0$ mm—distance between contacts in YIG/SLG sample, $\tilde{\lambda}_{\mathrm{SLG}} = \lambda_{\mathrm{SLG}}/a = 0.37$ nm—where $\lambda_{\mathrm{S}} = 1.4$ μm is the spin diffusion length under $V_{\mathrm{G}} = 0$ V for the CVD-grown SLG[89] used in the author's study and $a = 3.8 \times 10^3$ is the conductivity anisotropy in graphite[138], factor Γ was estimated to be $\Gamma_{\mathrm{Pt}} \sim 20$ for YIG/Pt system[43,139] and $\Gamma_{\mathrm{SLG}} \ll 1$ for YIG/SLG system[125], $V_{\mathrm{Pt}} = 1.6$ μV—inverse spin Hall effect voltage measured under 1 mW microwave power excitation in YIG/Pt sample, $\theta_{\mathrm{Pt}} = 0.04$—spin Hall angle of Pt[26], $d_{\mathrm{Pt}} = 10$ nm—thickness of the Pt layer, $\lambda_{\mathrm{Pt}} = 7$ nm—spin diffusion length in Pt[34,37], $l_{\mathrm{Pt}} = 0.75$ mm—distance between contacts in

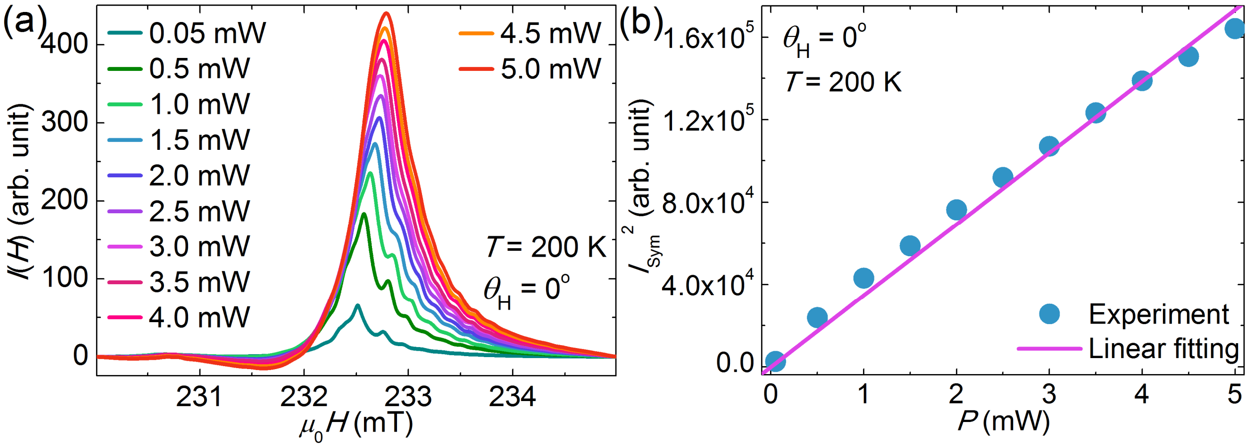

Figure 3-14. (a) FMR spectrum power dependence measured at T = 200 K, and direction of external magnetic field θ_H = 0° **(b)** Microwave power dependence of the squared amplitude of the FMR signal. Blue filled circles are experimental data, purple line is linear fitting.

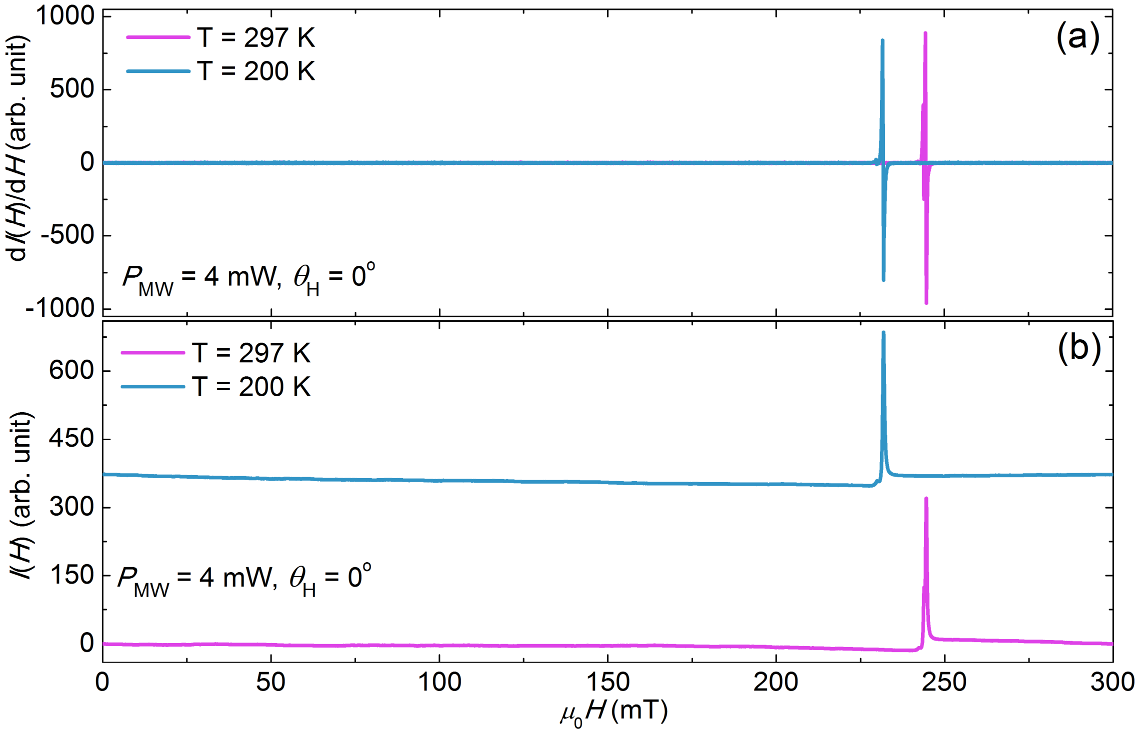

Figure 3-15. External magnetic field $\boldsymbol{H}$ sweep in the range 0-300 mT under microwave power P = 4 mW; T = 200 K and T = 297 K (blue and purple lines, respectively). **(a)** Derivative microwave absorbance spectrum dI(H)/dH, **(b)** microwave absorbance spectrum I(H).

YIG/Pt sample. However, the author notes that the spin diffusion length and spin Hall angle in Pt is still a matter of debate, and their estimation span over a wide range. The author estimated spin Hall angle of the SLG for all possible values of θ_{Pt} and λ_{Pt} reported in the literature. All calculated θ_{SLG} were of the same order of magnitude and lay within range from 1.0×10^{-6} to 8.6×10^{-6}.

3.4.6 Estimation of the type and strength of spin-orbit interaction in single-layer graphene

Finally, the author considered the origin of the spin-charge conversion mechanism in SLG in the studied system. The intrinsic SOI of graphene is responsible for the inverse spin Hall effect, and is present even when reflection symmetry with respect to graphene plane is not broken. The Rashba SOI, which arises in the presence of the electric field E perpendicular to the surface of the graphene layer and broken reflection symmetry, is responsible for the spin-charge conversion via the inverse Rashba-Edelstein effect. There is no agreement in the literature whether the intrinsic-like SOI or the Rashba-like SOI (in the range of commonly applied electric fields 10^{8}-10^{9} V/m) is dominant in pristine graphene, and estimations for both of them span over a wide range of 10^{-3}-10^{1} meV, 4 orders of magnitude[140–144]. The issue is non-trivial for future graphene-based applications: the intrinsic-like SOI leads to the opening of a topological gap at the K point, giving an effective mass to carriers and turning graphene into a quantum spin Hall insulator[143]. In contrast, the Rashba-like SOI interaction prevents the gap from opening[141,143] but can be used for spin control in spin transport experiments[145]. The Rashba SOI parameter α_R depends linearly on the electric field E induced by the gate voltage: $\alpha_{\mathrm{R}} \propto Ee\xi$, where ξ is the strength of the atomic SOI [140,141,146]. Amplitude of the charge current generated by the inverse Rashba-Edelstein effect linearly depends on the applied gate voltage. In contrast, the author observed a constant amplitude of the current I_{S} = 1.05 nA, which was independent of the gate voltage V_{G} far from the Dirac point, and switched polarity in the vicinity of V_{DP} (Fig. 3-11(b)). It indicates that contribution of the Rashba SOI in graphene is negligibly small, and rules out the inverse Rashba-Edelstein effect as a spin-charge conversion mechanism. Thus, the inverse spin Hall effect is the most probable mechanism for spin-charge conversion in the YIG/SLG system. Following calculation in refs.[43,125] and using YIG/Pt sample the author estimated spin Hall angle of SLG to be 3.5×10^{-6} (see section 3.4.5). The author notes that in calculations he used spin Hall angle θ_{Pt} and spin diffusion length λ_{Pt} of Pt—reported values for which varies in the literature. Thus, estimation of the spin Hall angle in SLG depends on these parameters. The author carried out estimation using all values of λ_{Pt} and θ_{Pt} reported in the literature: calculated θ_{SLG} was of the same order of magnitude and lay within range from 1.0×10^{-6} to 8.6×10^{-6}. Sign of the spin Hall angle was positive, i.e., voltage polarity (for electron carriers) was the same with metals with more than half-filled d electron orbital (Pd, Pt, Au). The spin Hall angle is proportional to the strength of SOI. While SOI depends on the number of electrons in the outermost shell, for the elements within the same group in the periodic table it was shown to follow Z^4 dependence[37,91]. C and Ge both belong to the group 14 and have external shelf $2s^2p^2$ and $4s^24p^2$, respectively. The Spin Hall angle of Ge was measured to be $\theta_{\mathrm{Ge}} = 10^{-3}$ [40,41]. Thus, in SLG spin Hall angle is expected to be on the order of $\theta_{\mathrm{SLG}} = \left(\frac{Z_{\mathrm{C}}}{Z_{\mathrm{Ge}}}\right)^4 \left(\frac{n_{\mathrm{Ge}}}{n_{\mathrm{C}}}\right)^3 \theta_{\mathrm{Ge}} = 1.6\times10^{-6}$, where n is the number of the outermost shell and Z is the atomic number. This is in good agreement with the author's result $\theta_{\mathrm{SLG}} = 3.5\times10^{-6}$. Using strength of SOI in Ge (290 meV), the author estimated SOI in the studied SLG to be $\frac{3.5\times10^{-6}}{10^{-3}}\times290$ meV = 1.0 meV. Since the Elliott-Yafet spin relaxation mechanism is dominant in SLG[147], one can also estimate strength of the SOI using the equation $|E_{\mathrm{F}}|\sqrt{\tau/\tau_{\mathrm{S}}}$, where E_{F} is the Fermi energy, τ and τ_{S} are the momentum and spin relaxation time, respectively[148,149]. Using equations $\lambda = \sqrt{D\tau}$ and $\lambda = \frac{h^2 v_{\mathrm{F}} \sigma_{\mathrm{S}}}{8e^2|E_{\mathrm{F}}|}$ (see section 3.4.3.5 for details), the author found $|E_{\mathrm{F}}|\sqrt{\frac{\tau}{\tau_{\mathrm{S}}}} = \frac{|E_{\mathrm{F}}|\lambda}{\lambda_{\mathrm{S}}} = \frac{h^2 v_{\mathrm{F}} \sigma_{\mathrm{S}}}{8e^2\lambda_{\mathrm{S}}} = 1.7$ meV, where $h = 6.6\times10^{-34}$ J·s—Planck constant, $v_{\mathrm{F}} = 10^6$ m·s^{-1}—Fermi velocity, $\sigma_{\mathrm{S}} = 0.18$ mS—measured sheet conductance of the SLG at $V_{\mathrm{G}} = 0$ V, $e = 1.6\times10^{-19}$ C—elementary charge, $\lambda_{\mathrm{S}} = 1.4$ μm—the spin diffusion length under $V_{\mathrm{G}} = 0$ V for the CVD-grown SLG[89] used in the author's study. Thus, both methods give strength of SOI in the studied SLG to be ~1 meV.

Recent studies on graphene heavily decorated with adatoms reported that the skew scattering can lead to the large intrinsic-like SOI and inverse spin Hall effect[126,150]. However, skew scattering mechanism of spin-charge conversion, which originated from the presence of Cu clusters in CVD-grown SLG [126], is not applicable in the author's case. In that study, density of Cu clusters (with average diameter of 40 nm and height more than 10 nm) in SLG was measured to be 0.6×10^{10} cm^{-2}. Thus, number of Cu clusters was ~60 per 1 μm×1 μm area and ~1500 per 5 μm×5 μm area. Figure 3-16 shows characteristic atomic force microscopy images of 1 μm×1 μm (Fig. 3-16(a)) and 5 μm×5 μm (Figs. 3-16(b) and 3-16(c)) areas of YIG/SLG samples used in the author's study. The author didn't find any Cu clusters left from

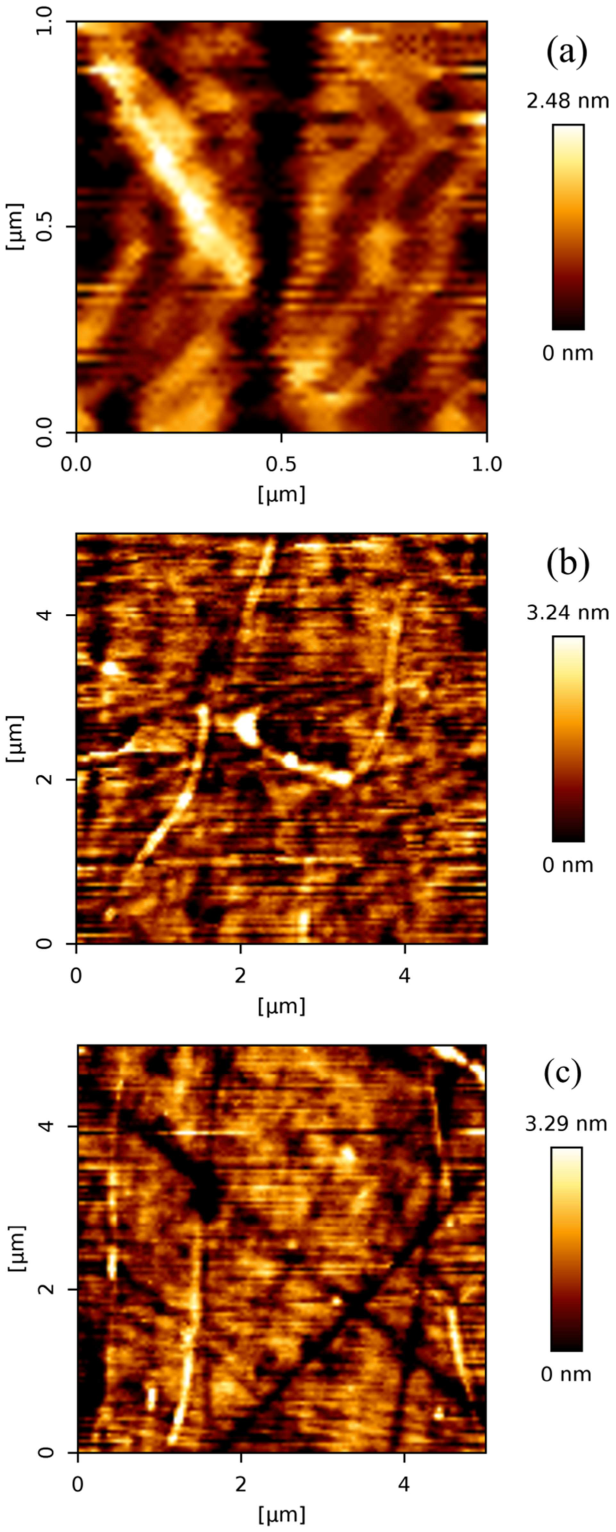

Figure 3-16. Atomic force microscopy images of YIG/SLG samples: **(a)** 1 μm×1 μm area, **(b,c)** 5 μm×5 μm areas. Scratches-like lines in the images are present due to the roughness of the YIG/SLG surface, as a result of the polishing of the YIG interface with alumina suspension.

the fabrication procedure (color scales bar in all images are below 5 nm). Scratches-like light and dark lines in the atomic force microscopy images are due to the polishing of the YIG substrate with alumina polishing suspension. While some Cu particles can be present in graphene grown on Cu foil, they are usually removed during the etching process. Such difference in the Cu cluster density between the author's and previous study[126] may arise from difference in the etching procedure, especially, etching time. Additionally, instead of Cu foil, in the author's study the epitaxial Cu(111) film grown on top of sapphire substrate was used[129]. Higher crystallinity of Cu(111) compared with Cu foil also reduces number of the produced Cu leftover.

The author's estimation of the intrinsic-like SOI strength in pristine SLG is three orders higher than 1 μeV predicted by early theoretical studies that used mixing of the σ-π orbitals in their calculations[140,141]. However, the later studies showed that dominant contribution to the intrinsic-like SOI comes from the nominally unfilled d orbitals, and the intrinsic SOI can be > 0.1 meV, if one also takes into account ripples in the graphene due to substrate roughness[144,151]. These first principal calculations also predicted dominance of the intrinsic SOI over Rashba SOI for transverse electric field $E = 10^9$ V/m, which is in agreement with the author's result[144].

3.5 Conclusion

In summary, the author experimentally clarified that the intrinsic-like SOI is dominant over the Rashba-like SOI in the SLG in the range of commonly applied electric fields (10^8-10^9 V/m). Strength of the intrinsic-like SOI in SLG was estimated to be ~1 meV. The author showed that the inverse spin Hall effect is the dominant spin-charge conversion mechanism in SLG, and that polarity of the spin-charge conversion current can be switched by gate voltage application.

Chapter 4. Ferromagnetic resonance and spin pumping efficiency for inverse spin-Hall effect normalization in yttrium-iron-garnet-based systems

4.1 Abstract

To pursue goal of the temperature investigation of the spin-charge conversion in the yttrium iron garnet/single-layer graphene system, author first studied temperature behavior of the spin pumping in yttrium iron garnet-based systems. In this chapter, the author presented an analysis of yttrium-iron-garnet-based systems, highly exploited in spin pumping experiments, and demonstrated proper normalization procedure for the inverse spin Hall effect in such systems. The author's results explained the discrepancy between experiment and theory recently observed in spin pumping experiments. Thus, the author's result finally allowed for quantitative analysis of the ISHE in various YIG-based experiments, including temperature dependent measurements.

Results presented in this chapter were published in the paper:

S. Dushenko, Y. Higuchi, Y. Ando, T. Shinjo, and M. Shiraishi, Ferromagnetic resonance and spin pumping efficiency for inverse spin-Hall effect normalization in yttrium-iron-garnet-based systems, Appl. Phys. Express **8**, 103002 (2015).

4.2 Introduction and motivation

Currently, spintronics is a blooming field with multiple applications and novel effects. For spintronics applications, however, efficient spin injection is of utmost importance, and the hunt for better spin injection materials is still ongoing. Devices with common metallic ferromagnetic materials suffer from the conductance mismatch problem and are in need of costly tunnel barriers to improve spin injection efficiency. A major step forward was made when spin pumping was shown to overcome the conductance mismatch problem[100]. Since then, spin pumping has been successfully used to realize spin injection and spin transport in various systems, including semiconductors[127,152], single-layer graphene[89] and semiconducting conjugated polymers[90]. However, recently, it was shown that in spin pumping experiments, metallic ferromagnets give rise to multiple spurious effects[51,52], which are hard to separate from the measured signals. The solution to this problem was found in the insulating ferrimagnet Yttrium Iron Garnet (chemical structure $Y_3Fe_2(FeO_4)_3$, YIG). YIG has a large band gap of 2.7 eV at room temperature, low magnetic damping and high Curie temperature (560 K), which makes it the perfect material for spintronics applications. It was anticipated that YIG would resolve yet another infamous problem of spintronics, namely, the large discrepancy in the values of the spin Hall angle θ_{SHA} of materials, with multiple studies being performed over the last few years[57,153,154]. The spin Hall effect (SHE)[7,11] and inverse spin Hall effect (ISHE)[21,22] enable interconversion between electric and spin current due to the spin-orbit interaction, thus allowing the integration of spintronics into modern electronics. The spin Hall angle describes the efficiency with which a spin current is converted into a charge current and vice versa. Unfortunately, the spin Hall angle values for the same material extracted from different experiments can scale more than one order of magnitude. Uncertainty in the spin Hall angle values impeded quantitative analysis in spin-charge conversion experiments and slowed down the progress of the entire field. Thus, it became an issue of the utmost importance to develop a method for the precise estimation of the spin Hall angle. Spin pumping experiments using YIG were expected to finally eliminate the spin Hall angle discrepancy. A new way to estimate the spin Hall angle using a single YIG/metal sample, eliminating the need of preparing multiple samples with various thicknesses, was recently proposed[108]. However, in that study, the experimental results could not be described by the theory even in the ultra-low (<1 nm) or ultra-large (>100 nm) limit for the spin diffusion length in Pt. Thus, quantitate formalism for YIG-based spin pumping experiments has yet to be developed.

In this chapter, the author demonstrated the correct normalization procedure for ISHE voltages in spin pumping experiments in YIG/metal systems. The author highlighted the factors that may lead to the incorrect analysis of ISHE in the previous studies and suggested a way to conduct proper analysis of the ferromagnetic resonance (FMR) and ISHE data in YIG-based systems.

4.3 Experimental details

YIG layers were grown on top of Gadolinium Gallium Garnet ($Gd_3Ga_5O_{12}$) substrates via liquid phase epitaxy. There were 3 types of samples with different thickness of the YIG layer: 40 nm, 2 µm and 10 µm. Samples with sizes of 10 µm × 2 mm × 5 mm and 2 µm × 1.5 mm × 4 mm (GRANOPT Co, Ltd., Akita, Japan) were polished using agglomerate-free alumina polishing suspension, with a 0.05-µm particle diameter size. After polishing, samples were annealed in an air atmosphere at 800°C for 2 hours. Samples with sizes of 40 nm × 2 mm × 5 mm (Murata Manufacturing Co, Ltd., Japan) were post-annealed in an oxygen atmosphere at 850°C for 2 hours. The Pt layer in the samples for ISHE measurements, YIG/Pt (d_{YIG} = 2 µm), was produced using an electron beam evaporation system. For FMR measurements, samples were mounted inside a TE_{011} cavity of the JES-FA200 electron spin resonance spectrometer (JEOL, Ltd., Tokyo, Japan) with a microwave frequency f = 9.12 GHz. Microwave power P_{MW} was applied in the range from 0 to 3 mW. Static external magnetic field H was applied along the short side of the plane of the samples. Electromotive force from the YIG/Pt samples was detected using a Keithly 2182A Nanovoltmeter; contacts were made using silver paste and Cu wire.

4.4 Experimental results and discussion

4.4.1 Spin wave resonances in the YIG ferromagnetic resonance spectrum

The author now proceeds to the experimental results and discussion. Inside of the YIG layer, dynamical coupling of the rf microwave magnetic field h to the YIG magnetization drove it into precession and excited spin wave resonances. Due to the low damping parameters of YIG, a fundamental uniform mode with wave vector k close to zero was excited by an applied microwave field at external magnetic field $H = H_{\mathrm{FMR}}$, along with additional spin wave resonances. The spin wave resonances in the

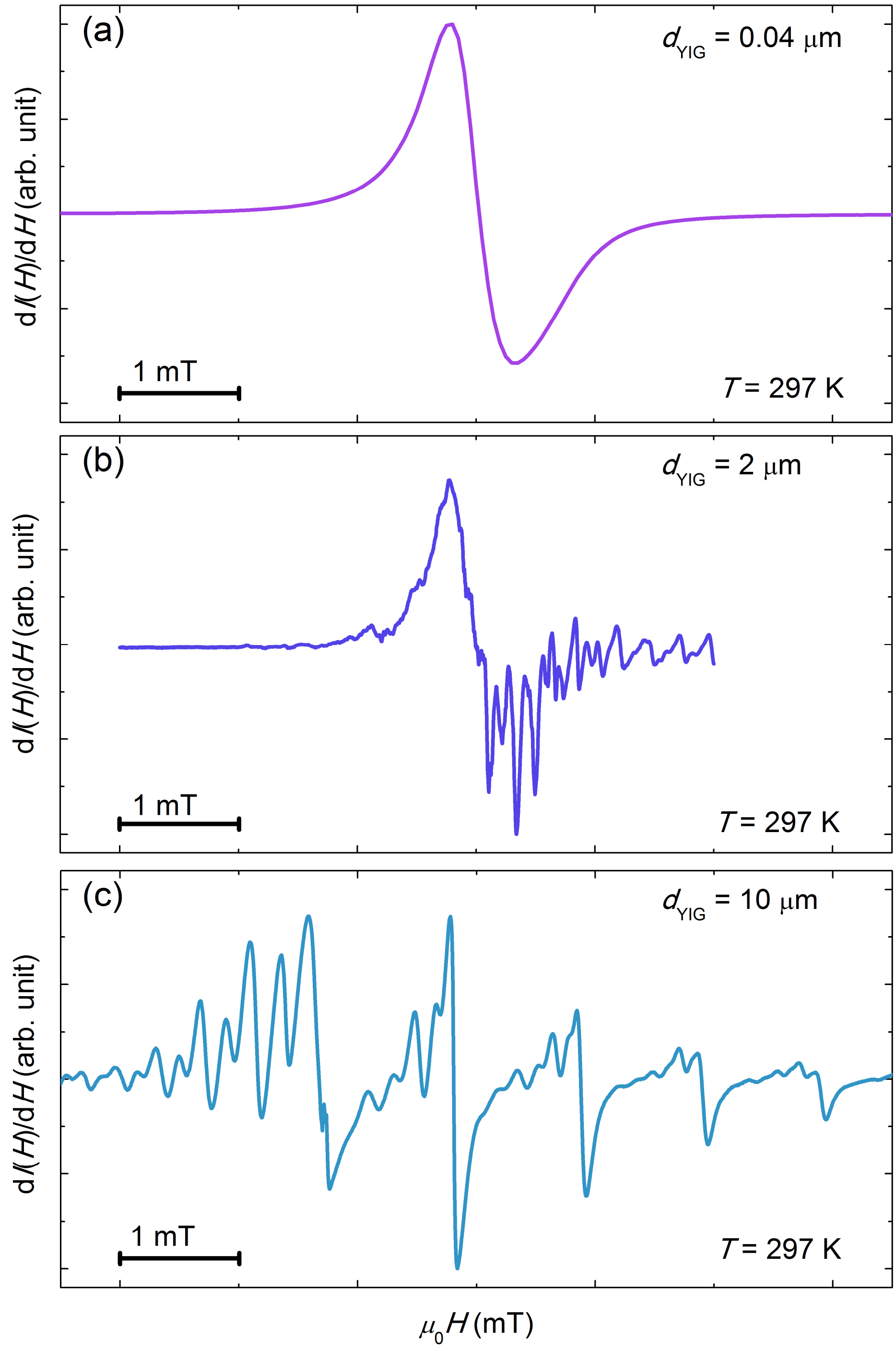

Figure 4-1. Derivative absorbance FMR spectra of YIG layers with thickness **(a)** d_{YIG} = 40 nm, **(b)** d_{YIG} = 2 µm and **(c)** d_{YIG} = 10 µm at T = 297 K for the in-plane static external magnetic field configuration.

in-plane magnetic field configuration were caused by the magnetostatic surface waves at $H < H_{\mathrm{FMR}}$ and magnetostatic backward volume waves at $H > H_{\mathrm{FMR}}$[131,132], described by the dispersion relations derived by Damon and Eshbach[155]. Figures 4-1(a,b,c) show an increase in the number of spin wave resonances as the thickness of the YIG layer d_{YIG} increased. At d_{YIG} = 40 nm, only the uniform mode was present in the derivative FMR spectrum (Fig. 4-1(a)); at d_{YIG} = 2 μm, the shape of the uniform FMR mode was distorted by the presence of the magnetostatic backward volume waves (Fig. 4-1(b)); at d_{YIG} = 10 μm, the uniform FMR mode could not be distinguished in the derivative FMR spectrum (Fig. 4-1(c)). However, the spin injection efficiency in the spin pumping experiments from the YIG into the adjacent layer driven by FMR is different between the uniform mode at H_{FMR} and additional spin wave resonances and depends on the wave vector k[53,59]. The author first discuss the FMR properties of the uniform mode, which gives a dominant contribution to the ISHE, and then shows the importance of the separation of the uniform mode from additional spin wave resonances in the spin pumping experiments for the proper quantitative analysis.

4.4.2 Power dependence of the uniform mode of ferromagnetic resonance

The FMR absorbance spectrum has a Lorentzian peak shape, with the center at the H_{FMR}. Figure 4-2(a) shows a power dependence of the FMR absorbance spectrum of the YIG (d_{YIG} = 40 nm) sample. A clear Lorentzian shape was observed, and the fitting function:

$$I(H) == I_{\mathrm{Sym}}\frac{G^2}{\mu_0^2(H-H_{\mathrm{FMR}})^2+G^2}+I_{\mathrm{Asym}}\frac{-2G\mu_0(H-H_{\mathrm{FMR}})}{\mu_0^2(H-H_{\mathrm{FMR}})^2+G^2}+a\mu_0(H-H_{\mathrm{FMR}})+b$$

was used to extract the amplitude of the FMR spectrum I and damping constant β, which is related to the FMR full width at half maximum $\Delta H_{\mathrm{FWHM}} = 2G$. While the FMR full width at half maximum ΔH_{FWHM} only slightly increased with increasing power (Fig. 4-2(b)), FMR amplitude I showed a square root power dependence, thus making $I^2 \propto P_{\mathrm{MW}}$. Figure 4-2(c) shows linear fitting of the I^2 versus microwave power P_{MW}. Linear proportionality of the FMR amplitude to the square root of microwave power is not specific to a YIG material, but a property of any ferromagnetic system (see fig. 4-3 for $I(P_{\mathrm{MW}})$ for Py). In the electron spin resonance system, microwaves were reflected from the cavity with the sample and converted into an electric voltage signal via rectenna, which consisted of a dipole antenna and Schottky diode. The microwaves induced an ac voltage in the antenna such that $P_{\mathrm{MW}} \propto P_{\mathrm{El}} \propto \mathrm{V}^2$. The voltage was rectified

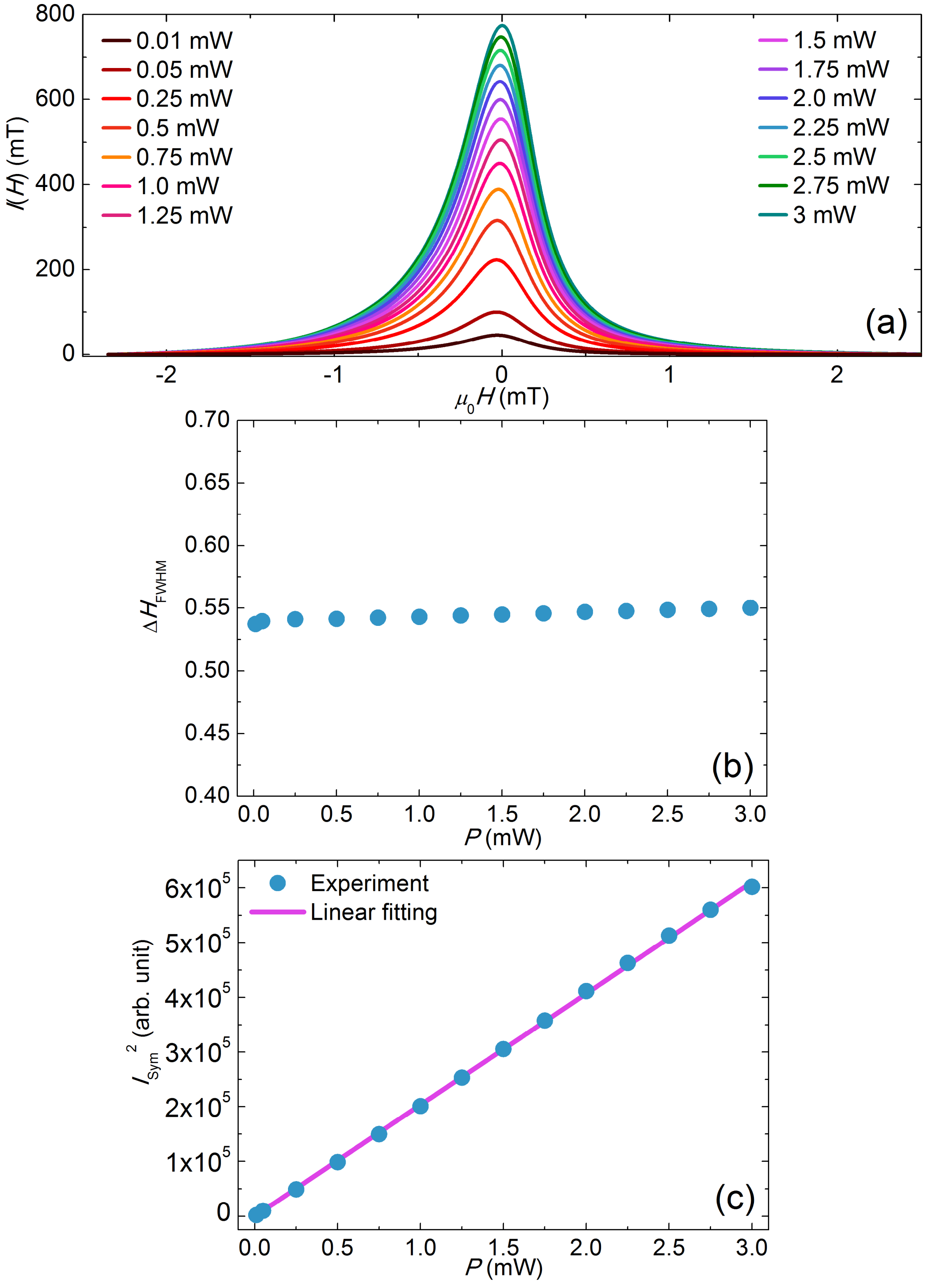

Figure 4-2. Power dependence of the **(a)** FMR absorbance spectrum $I(H)$, **(b)** FMR full width at half maximum ΔH_{FWHM} and **(c)** FMR square amplitude $I_{\mathrm{Sym}}{}^2$ for the d_{YIG} = 40 nm YIG layer. In (c) the experimental data are represented by blue filled circles and linear fitting—by purple line.

by the diode working in the linear regime. Thus, the detector current output was proportional to the square root of the microwave power. It is important to measure FMR below the power, where $I(P_{MW}^{1/2})$ deviates from linearity. At high power levels (i.e., large magnetization precession angles), parametric Suhl instabilities lead to FMR saturation[156]. In that case, spin waves will be excited parametrically and draw energy from the uniform mode, which complicates quantitative analysis.

4.4.3 Power dependence of the electromotive force generated due to ISHE under ferromagnetic resonance

When spin pumping is used as the spin injection method, magnetization precession under the FMR condition drives pure spin current from the ferromagnetic layer into the adjacent layer[44,48].

It has been theoretically predicted and experimentally confirmed by many studies that electric voltage generated by the ISHE is proportional to the square amplitude of the rf microwave magnetic field h, which makes it linearly proportional to the applied microwave power P_{MW}[38,100]. Voltage generated by the ISHE is proportional to the generated spin current, which is maximized at the FMR resonance field H_{FMR}. Hence, the ISHE voltage generated by spin pumping under the FMR condition takes the Lorentzian shape

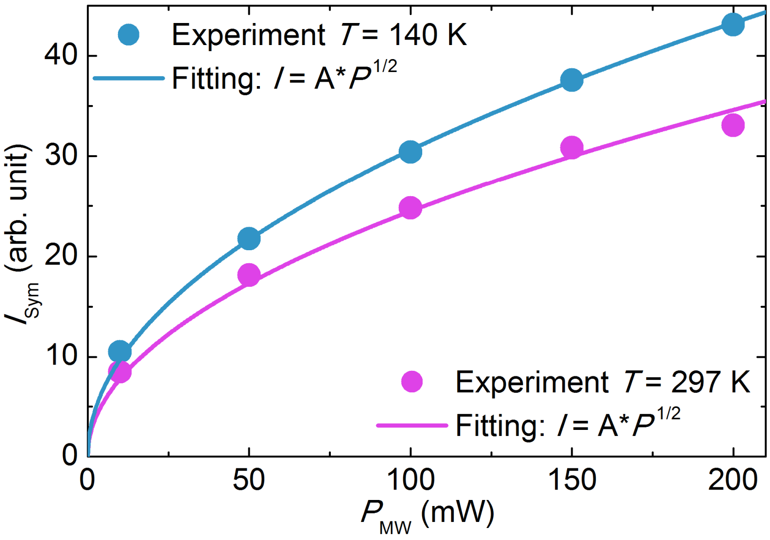

Figure 4-3. Power dependence of the FMR amplitude I of SiO_2/Py structure at 297 K (blue) and 140 K (purple). Solid circles are experimental data, solid lines are fitting by the square root of microwave power.

and is fitted by the same fitting function $I(H)$ as the FMR absorbance signal:

$$V(H; H_{\mathrm{FMR}}, G, V_{\mathrm{ISHE}}) = V_{\mathrm{ISHE}} \frac{G^2}{\mu_0^2(H - H_{\mathrm{FMR}})^2 + G^2} + V_{\mathrm{Asym}} \frac{-2G\mu_0(H - H_{\mathrm{FMR}})}{\mu_0^2(H - H_{\mathrm{FMR}})^2 + G^2} +$$

$$+\mathrm{a}\mu_0(H - H_{\mathrm{FMR}}) + \mathrm{b}$$

where the FMR amplitude I_{Sym} was substituted by the ISHE voltage amplitude V_{ISHE}[20]. To take into account differences in the absorbed microwave power between different measurements, many studies have used the normalization of V_{ISHE} by the amplitude I of the FMR absorbance signal[52,108]. For example, $V_{\mathrm{ISHE}}^{\mathrm{norm}}(T)=V_{\mathrm{ISHE}}(T)/(I(T)/I(300\ \mathrm{K}))$ was used to extract the temperature dependence of the Pt spin diffusion length $\lambda_{\mathrm{Pt}}(T)$[108]. The normalization itself is an important procedure to properly extract the spin-orbit interaction-dependent parameters of the materials ($\theta_{\mathrm{SHA}}(T)$ or $\lambda(T)$) from the ISHE spin pumping measurements. However, the generated spin current density is proportional to the area of magnetization trajectory, i.e., $S \propto \Theta^2$, where $\Theta = 2h/\Delta H_{\mathrm{FWHM}}$ is the magnetization precession cone angle[57]. In contrast, the FMR amplitude is linearly proportional to $\sqrt{P_{\mathrm{MW}}}$ (Figs. 4-2(c) and 4-3). Thus, V_{ISHE} should be normalized by the I^2, which is proportional to the absorbed power and generated spin current ($\propto S \propto h^2 \propto P_{\mathrm{MW}}$), rather than by the amplitude I of the FMR spectrum ($h \propto \sqrt{P_{\mathrm{MW}}}$). This may be one of the reasons for the discrepancy between the theory and experimental results reported in the recent study of the temperature evolution of the electromotive force in the YIG/Pt system[108]. Because the FMR signal reduced with decreasing temperature, normalization by I instead of I^2 resulted in the overestimation of the generated spin current at low temperatures. In that case, the theoretically estimated V_{ISHE} would be larger than the experimentally measured V_{ISHE}. In agreement with this, even V_{ISHE} calculated in the ultra large limit $\lambda_{\mathrm{Pt}} > 100$ nm was larger than the experimentally observed V_{ISHE}. This illustrates the importance of the normalization procedure—which the author proposed in this chapter—for the proper extraction of the spin dependent parameters of the system.

4.4.4 FMR and electromotive force generated in the YIG/Pt systems with spin wave resonances

Now the author proceeds to the discussion of the YIG-based systems with thick YIG layers, where additional spin wave resonances are present (Fig. 4-1(b)) and (Fig. 4-1(c)). Figure 4-4(a) shows the temperature dependence of the derivative absorbance FMR spectrum of the YIG/Pt sample with $d_{\mathrm{YIG}} = 2$

µm and d_{Pt} = 10 nm. In the absorbance FMR spectrum at T = 297 K (Fig. 4-4(b), orange line), two clear peaks were present (represented by the intersections with the zero level in the derivative absorbance FMR spectrum (Fig. 4-4(a)) correspondingly). Interestingly, the spin injection efficiency for Peak 1, located at the smaller external magnetic field H_{Peak1}, was much higher than the spin injection efficiency for Peak 2, which was located at the higher external magnetic field H_{Peak2}. Figure 4-4(c) shows the electromotive force generated in the Pt layer via spin pumping and ISHE. Although the amplitudes of the FMR signals for Peak 1 and Peak 2 were comparable (125 and 86 arb. unit, respectively), at H_{Peak1} (indicated by black arrows in Figs. 4-4(b,c)), a large symmetrical in shape electromotive force (5.27 µV) was detected from the Pt layer; in contrast, a more than one order of magnitude smaller electromotive force contribution <0.4 µV was present at H_{Peak2}. The possible origin of this was the higher spin injection efficiency for the

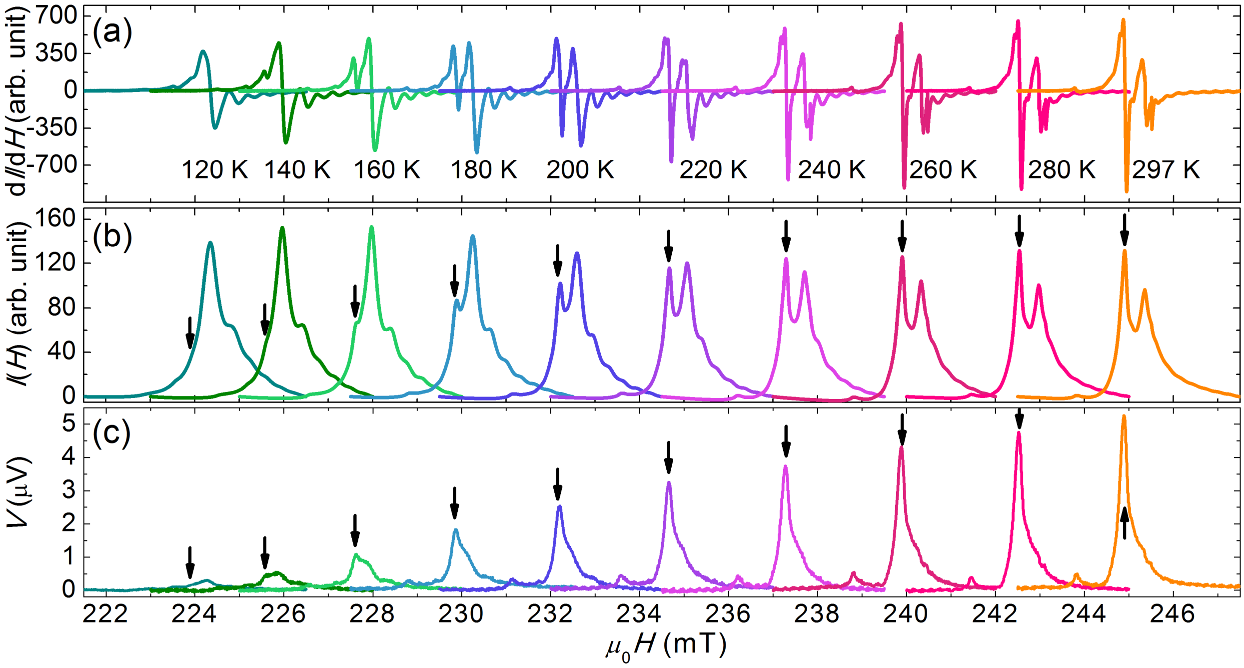

Figure 4-4. (a) Temperature evolution of the derivative FMR absorbance spectrum of the YIG/Pt structure. **(b)** Temperature evolution of the FMR absorbance spectrum of the YIG/Pt structure. Absorbance spectrum consisted of two separated peaks. Peak responsible for the spin pumping marked with a black arrow. **(c)** Temperature evolution of the electromotive force detected from the Pt layer in the YIG/Pt structure under the FMR. Microwave power was set to 1 mW. Thickness of the layers were d_{YIG} = 2 µm and d_{Pt} = 10 nm.

magnetostatic surface waves and uniform mode compared to the magnetostatic backward volume waves, which are located at higher external magnetic fields[53,59]. Contributions to the FMR spectrum from Peak 1 and Peak 2 were separated by the fitting function

$$I'(H) = I_{\mathrm{Peak1}} \frac{{\beta_{\mathrm{Peak1}}}^2}{\mu_0^2 (H - H_{\mathrm{Peak1}})^2 + {\beta_{\mathrm{Peak1}}}^2} + I_{\mathrm{Peak2}} \frac{{\beta_{\mathrm{Peak2}}}^2}{\mu_0^2 (H - H_{\mathrm{Peak2}})^2 + {\beta_{\mathrm{Peak2}}}^2} - $$

$$-I'_{\mathrm{Peak2}} \frac{2\beta_{\mathrm{Peak2}} \mu_0 (H - H_{\mathrm{Peak2}})}{\mu_0^2 (H - H_{\mathrm{Peak2}})^2 + {\beta_{\mathrm{Peak2}}}^2},$$

where the first term represents the contribution to the FMR spectrum from Peak 1, and the second and third terms represent the contribution to the FMR spectrum from Peak 2, in which case both symmetrical and asymmetrical parts are present due to the nature of the dispersion relations for the spin waves.

Interestingly, Peak 1 and Peak 2 showed opposite temperature dependence. Amplitude I_{Peak2} increased, while amplitude I_{Peak1} decreased, with decreasing temperature, until $T < 180$ K, at which it could not be unambiguously extracted from the FMR absorbance signal (Figs. 4-4(b) and 4-5(b)). In agreement with the I_{Peak1} behavior, the electromotive force decreased with decreasing temperature, confirming the dominance of the Peak 1 contribution to the spin pumping in the YIG/Pt sample. Figures 4-5(a,d) show the power dependence of the Peak 1 FMR signal (see the purple dashed lines in Fig. 4-5(e) and 4-5(f) for fitting examples using $I'(H)$ function at low P = 0.05 mW and high P = 3 mW microwave power, respectively). Full width at half maximum ΔH_{FWHM} (Fig. 4-5(c)) exhibited a small increase with increasing temperature similar to the behavior observed from the 40 nm YIG samples. Fitting function $a \cdot P^B$ yielded $B = 0.50 \pm 0.01$ for $I_{\mathrm{Peak1}}(P)$ (Fig. 4-5(d)), supporting the $\sqrt{P}$ behavior of the spin pumping part of the FMR signal discussed above. In addition, V_{ISHE} for the dominant voltage peak (extracted using a three-peak Lorentz fitting function) showed a linear dependence on the microwave power (Fig. 4-6(d)). The position and number of spin wave resonances in the FMR spectrum differ from sample to sample depending on the interface conditions, sizes of the YIG layer, etc. In the samples where the spin pumping peak in the FMR signal was not field-resolved from the additional spin wave resonances, one will measure $I_{\mathrm{Peak1}}+I_{\mathrm{Peak2}}$ as the amplitude of the spin pumping signal instead of I_{Peak1}. In contrast to the I_{Peak1} strong temperature dependence, $I_{\mathrm{Peak1}}+I_{\mathrm{Peak2}}$ stayed constant regardless of the temperature (204 ± 14 arb. unit). Figure 4-7 shows the effect of the normalization procedure on the $V_{\mathrm{ISHE}}(\mathrm{T})$ estimation, where the FMR amplitude factor $I^{\mathrm{norm}} = I(T)/I(297\ \mathrm{K})$. Normalization using $(I_{\mathrm{Peak1}}+I_{\mathrm{Peak2}})^{\mathrm{norm}}$ or ${I_{\mathrm{Peak1}}}^{\mathrm{norm}}$,

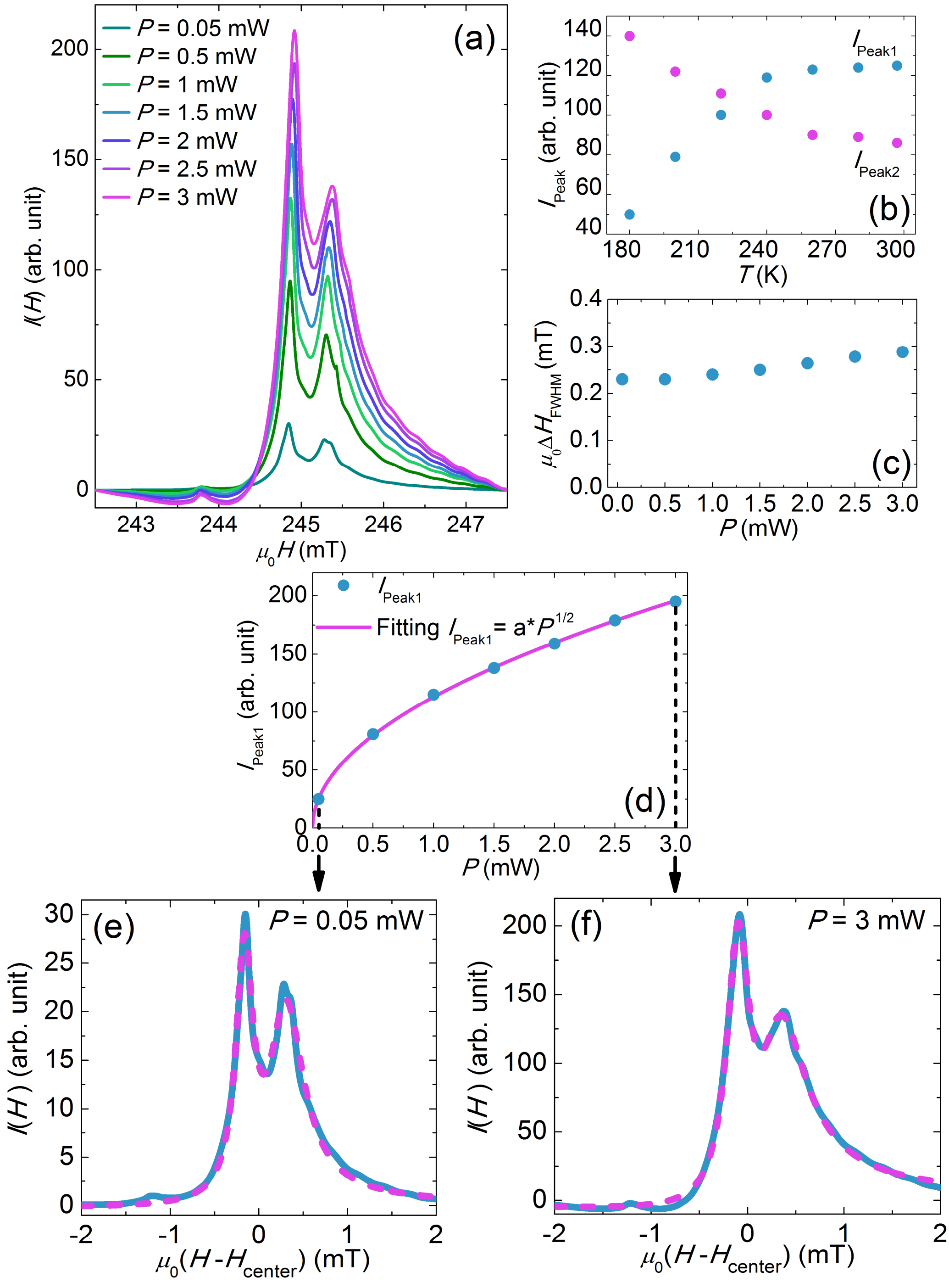

Figure 4-5. (a) Power dependence of absorbance FMR spectrum. **(b)** Temperature dependence of the FMR amplitudes I_{Peak1} (blue filled circles) and I_{Peak2} (purple filled circles) calculated using fitting function $I'(H)$. Two peaks showed opposite temperature dependence. **(c)** Power dependence of the FMR full width at half maximum ΔH_{FWHM}. **(d)** Power dependence of the I_{Peak1} (blue filled circles) and fitting by the square root (purple line). Examples of the fitting using function $I'(H)$ at P = 0.05 mW **(e)** and P = 3 mW **(f)**. Blue lines are experimental data, dashed purple lines are the fitting by the $I'(H)$ function described in the section 4.4.4.

instead of $(I_{\mathrm{Peak1}}^{\mathrm{norm}})^2$ resulted in the underestimation of V_{ISHE} at low temperatures. An improper normalization procedure would lead to misinterpretation of the decreasing electromotive force as the decrease of the spin Hall angle or/and increase of the spin diffusion length of material with decreasing temperature. Indeed, in the study[108] where the FMR spectrum quasi-uniform mode was not field-resolved from the additional spin wave resonances, even $\lambda_{\mathrm{Pt}} > 100$ nm could not explain the experimental data at low temperatures. Previously, it was shown that the spin pumping efficiency $\eta = V_{\mathrm{ISHE}}/I$ of the magnetostatic surface waves (due to their localization at the interface) is superior to the uniform mode or the magnetostatic backward volume waves and increases with the mode number[53]. In contrast, for the magnetostatic backward volume waves η is independent of mode number. However, the FMR spectrum is dominated by waves with small wave vector k and constant η because of their large FMR amplitude I. Thus, $V_{\mathrm{ISHE}} = \eta I$ is determined by the low k modes and takes the shape of the FMR spectrum despite low spin pumping efficiency η. The author showed for the first time that even for dominant FMR contributions with k close to 0, spin pumping efficiency η can be different by up to a factor of 10 (Figs. 4-4(b,c)). Moreover, the author demonstrated that these contributions can have opposite temperature dependence (Fig. 4-5(b)). Thus, author's result provided crucial information for the proper ISHE analysis in YIG-based systems.

4.5 Conclusion

In summary, in this chapter the author pointed out the importance of the normalization procedure and isolation of the spin pumping contribution from additional spin wave resonances in a YIG-based system. The author's study explained the discrepancy between experiment and theory recently observed in spin pumping experiments. Thus, the author's result may finally allow for quantitative analysis of the ISHE in various YIG-based experiments, including temperature dependent measurements, opening a route for the estimation of the spin diffusion length and the spin Hall angle from single samples. Additionally, it made possible the comparison of the spin Hall angle and spin diffusion length to the values obtained from other methods, such as weak anti-localization measurements, which are only available at low temperature.

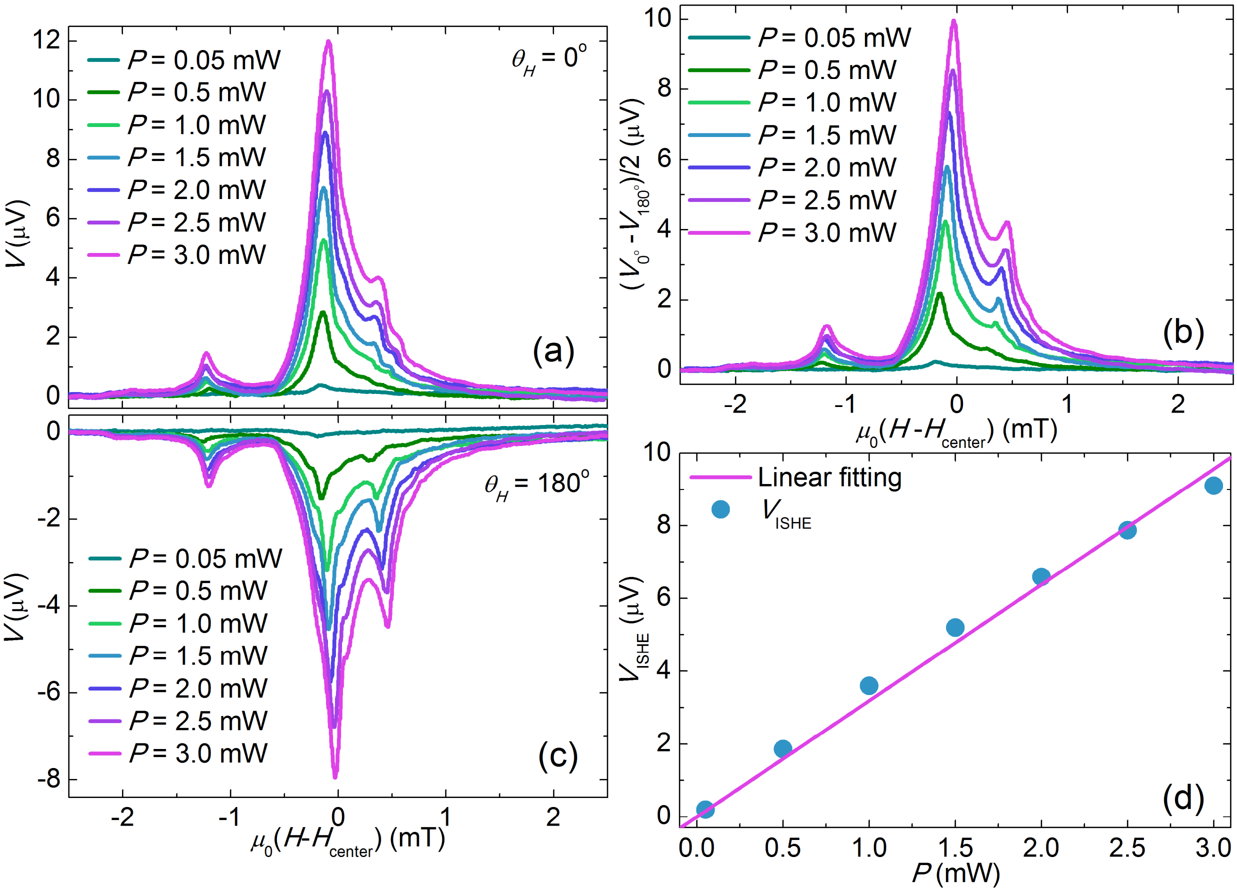

Figure 4-6. Power dependence of the electromotive force detected from the YIG (2 μm)/Pt (10 nm) sample under FMR for the external magnetic field ***H*** applied in the **(a)** $\theta_H = 0°$ and **(b)** $\theta_H = 180°$. (c) ISHE voltage at different microwave power levels.. **(d)** Power dependence of the V_{ISHE} for the dominant voltage peak (blue filled circles). The purple line shows linear fitting.

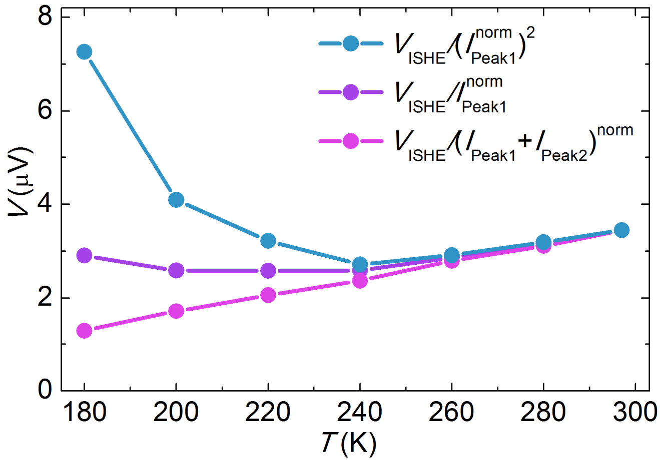

Figure 4-7. Temperature dependence of the V_{ISHE} normalized with different normalization procedures as described in the section 4.4.4.

Chapter 5. Conclusion

In this study the author focused on two elements from Group 14 of periodic table: C and Ge. Using spin pumping as the spin injection method and the inverse spin Hall effect as the spin detection method the author answered two previously unresolved problems: room-temperature spin transport in Ge and origin of spin-orbit interaction in the single-layer graphene.

In the second chapter the author was the first to directly demonstrate spin transport at room temperature in epitaxial n-Ge with a doping concentration of $\sim 1.0\times10^{19}$ cm^{-3} using a spin pumping method and the inverse spin Hall effect. The author estimated the spin diffusion length in Ge at room temperature to be $\lambda_{\text{n-Ge}} = 660 \pm 200$ nm, which is comparable to the reported values for Si channels with similar doping concentration, however, spin diffusion length can be further increased with improving quality of the Ge channel. Additionally, author showed that the spin relaxation time increased with decreasing temperature, in agreement with recently proposed theory of donor-driven spin relaxation in multivalley semiconductors. As a result of the author’s study, room-temperature Ge spintronics was established.

In the third chapter the author experimentally clarified that the intrinsic-like spin-orbit interaction is dominant over the Rashba-like spin-orbit interaction in the single-layer graphene. The author estimated strength of the intrinsic-like spin-orbit interaction in single-layer graphene to be ~1 meV. Using electric top gate via ionic liquid the author showed that the inverse spin Hall effect is the dominant spin-charge conversion mechanism in single-layer graphene, and that polarity of the spin-charge conversion current can be switched by gate voltage application.

In the fourth chapter—as a preparation for the study of temperature dependence of the spin-charge conversion in the yttrium iron garnet/single-layer graphene system—the author studied temperature dependence of the inverse spin Hall effect in the yttrium iron garnet/Pt system. The author pointed out the importance of the normalization procedure and isolation of the spin pumping contribution from additional spin wave resonances in the yttrium iron garnet-based systems. The author’s study explained the discrepancy between experiment and theory recently observed in spin pumping experiments, and paved a way for precise analysis of the inverse spin Hall effect in yttrium iron garnet-based experiments.

Bibliography

1. *Spin Dependent Transport in Magnetic Nanostructures*. **20021209,** (CRC Press, 2002).
2. *Modern Aspects of Spin Physics*. **712,** (Springer Berlin Heidelberg, 2007).
3. M. I. Dyakonov. *Springer Series In Solid-State Sciences 157 : Spin Physics in Semiconductors*. (2008).
4. J. Parkinson & D. J. J. Farnell. *An Introduction to Quantum Spin Systems*. **816,** (Springer Berlin Heidelberg, 2010).
5. *Spin Current*. (Oxford University Press, 2012). doi:10.1093/acprof:oso/9780199600380.001.0001
6. *Handbook of Spintronics*. (Springer Netherlands, 2016). doi:10.1007/978-94-007-6892-5
7. Y. K. Kato, R. C. Myers, A. C. Gossard & D. D. Awschalom. Observation of the Spin Hall Effect in Semiconductors. *Science (80-.).* **306,** 1910–1913 (2004).
8. J. E. Hirsch. Spin Hall Effect. *Phys. Rev. Lett.* **83,** 1834–1837 (1999).
9. N. F. Mott. The Scattering of Fast Electrons by Atomic Nuclei. *Proc. R. Soc. A Math. Phys. Eng. Sci.* **124,** 425–442 (1929).
10. J.-B. Michel, Y. K. Shen, A. P. Aiden, A. Veres, M. K. Gray, J. P. Pickett, D. Hoiberg, D. Clancy, P. Norvig, J. Orwant, S. Pinker, M. A. Nowak & E. L. Aiden. Quantitative Analysis of Culture Using Millions of Digitized Books. *Science (80-.).* **331,** 176–182 (2011).
11. M. I. Dyakonov & V. I. Perel. Current-induced spin orientation of electrons in semiconductors. *Phys. Lett. A* **35,** 459–460 (1971).
12. M. I. Dyakonov & V. I. Perel. Possibility of orienting electron spins with current. *JETP Letters* **13,** 467–469 (1971).
13. J. Wunderlich, B. Kaestner, J. Sinova & T. Jungwirth. Experimental Observation of the Spin-Hall Effect in a Two-Dimensional Spin-Orbit Coupled Semiconductor System. *Phys. Rev. Lett.* **94,** 047204 (2005).
14. V. Sih, R. C. Myers, Y. K. Kato, W. H. Lau, a. C. Gossard & D. D. Awschalom. Spatial imaging of the spin Hall effect and current-induced polarization in two-dimensional electron gases. *Nat. Phys.* **1,** 31–35 (2005).
15. K. Nomura, J. Wunderlich, J. Sinova, B. Kaestner, A. H. MacDonald & T. Jungwirth. Edge-spin

accumulation in semiconductor two-dimensional hole gases. *Phys. Rev. B* **72,** 245330 (2005).

16. N. P. Stern, S. Ghosh, G. Xiang, M. Zhu, N. Samarth & D. D. Awschalom. Current-Induced Polarization and the Spin Hall Effect at Room Temperature. *Phys. Rev. Lett.* **97,** 126603 (2006).
17. S. O. Valenzuela & M. Tinkham. Direct electronic measurement of the spin Hall effect. *Nature* **442,** 176–179 (2006).
18. L. Vila, T. Kimura & Y. Otani. Evolution of the Spin Hall Effect in Pt Nanowires: Size and Temperature Effects. *Phys. Rev. Lett.* **99,** 226604 (2007).
19. T. Kimura, Y. Otani, T. Sato, S. Takahashi & S. Maekawa. Room-Temperature Reversible Spin Hall Effect. *Phys. Rev. Lett.* **98,** 156601 (2007).
20. E. Saitoh, M. Ueda, H. Miyajima & G. Tatara. Conversion of spin current into charge current at room temperature: Inverse spin-Hall effect. *Appl. Phys. Lett.* **88,** 182509 (2006).
21. N. S. Averkiev & M. I. Dyakonov. Fiz. Tekh. Poluprov. *Sov. Phys. Semicond.* **17,** 393 (1983).
22. A. A. Bakun, B. P. Zakharchenya, A. A. Rogachev, M. N. Tkachuk & V. G. Fleisher. Observation of a surface photocurrent caused by optical orientaion of electrons in a semiconductor. *JETP Lett.* **40,** 1293–1295 (1984).
23. K. Ando, Y. Kajiwara, S. Takahashi, S. Maekawa, K. Takemoto, M. Takatsu & E. Saitoh. Angular dependence of inverse spin–Hall effect induced by spin pumping investigated in a Ni81Fe19/Pt thin film. *Phys. Rev. B* **78,** 014413 (2008).
24. O. Mosendz, V. Vlaminck, J. E. Pearson, F. Y. Fradin, G. E. W. Bauer, S. D. Bader & A. Hoffmann. Detection and quantification of inverse spin Hall effect from spin pumping in permalloy/normal metal bilayers. *Phys. Rev. B* **82,** 214403 (2010).
25. O. Mosendz, J. E. Pearson, F. Y. Fradin, G. E. W. Bauer, S. D. Bader & A. Hoffmann. Quantifying Spin Hall Angles from Spin Pumping: Experiments and Theory. *Phys. Rev. Lett.* **104,** 046601 (2010).
26. K. Ando, S. Takahashi, J. Ieda, Y. Kajiwara, H. Nakayama, T. Yoshino, K. Harii, Y. Fujikawa, M. Matsuo, S. Maekawa & E. Saitoh. Inverse spin-Hall effect induced by spin pumping in metallic system. *J. Appl. Phys.* **109,** 103913 (2011).
27. A. Azevedo, L. H. Vilela-Leão, R. L. Rodríguez-Suárez, A. F. Lacerda Santos & S. M. Rezende. Spin pumping and anisotropic magnetoresistance voltages in magnetic bilayers: Theory and

experiment. *Phys. Rev. B* **83,** 144402 (2011).

28. L. H. Vilela-Leão, G. L. da Silva, C. Salvador, S. M. Rezende & A. Azevedo. Direct current voltage generated in metallic layers by spin pumping. *J. Appl. Phys.* **109,** 07C910 (2011).
29. V. Castel, N. Vlietstra, B. J. van Wees & J. Ben Youssef. Frequency and power dependence of spin-current emission by spin pumping in a thin-film YIG/Pt system. *Phys. Rev. B* **86,** 134419 (2012).
30. V. Castel, N. Vlietstra, J. Ben Youssef & B. J. van Wees. Platinum thickness dependence of the inverse spin-Hall voltage from spin pumping in a hybrid yttrium iron garnet/platinum system. *Appl. Phys. Lett.* **101,** 132414 (2012).
31. Z. Feng, J. Hu, L. Sun, B. You, D. Wu, J. Du, W. Zhang, A. Hu, Y. Yang, D. M. Tang, B. S. Zhang & H. F. Ding. Spin Hall angle quantification from spin pumping and microwave photoresistance. *Phys. Rev. B* **85,** 214423 (2012).
32. K. Kondou, H. Sukegawa, S. Mitani, K. Tsukagoshi & S. Kasai. Evaluation of Spin Hall Angle and Spin Diffusion Length by Using Spin Current-Induced Ferromagnetic Resonance. *Appl. Phys. Express* **5,** 073002 (2012).
33. L. Liu, C.-F. Pai, Y. Li, H. W. Tseng, D. C. Ralph & R. A. Buhrman. Spin-Torque Switching with the Giant Spin Hall Effect of Tantalum. *Science (80-.).* **336,** 555–558 (2012).
34. H. Nakayama, K. Ando, K. Harii, T. Yoshino, R. Takahashi, Y. Kajiwara, K. Uchida, Y. Fujikawa & E. Saitoh. Geometry dependence on inverse spin Hall effect induced by spin pumping in Ni81Fe19/Pt films. *Phys. Rev. B* **85,** 144408 (2012).
35. J.-C. Rojas-Sánchez, N. Reyren, P. Laczkowski, W. Savero, J.-P. Attané, C. Deranlot, M. Jamet, J.-M. George, L. Vila & H. Jaffrès. Spin Pumping and Inverse Spin Hall Effect in Platinum: The Essential Role of Spin-Memory Loss at Metallic Interfaces. *Phys. Rev. Lett.* **112,** 106602 (2014).
36. W. Zhang, V. Vlaminck, J. E. Pearson, R. Divan, S. D. Bader & A. Hoffmann. Determination of the Pt spin diffusion length by spin-pumping and spin Hall effect. *Appl. Phys. Lett.* **103,** 242414 (2013).
37. H. L. Wang, C. H. Du, Y. Pu, R. Adur, P. C. Hammel & F. Y. Yang. Scaling of spin hall angle in 3d, 4d, and 5d metals from $Y_3Fe_5O_{12}$/metal spin pumping. *Phys. Rev. Lett.* **112,** 197201 (2014).
38. K. Ando & E. Saitoh. Inverse spin-Hall effect in palladium at room temperature. *J. Appl. Phys.*

108, 113925 (2010).

39. K. Ando & E. Saitoh. Observation of the inverse spin Hall effect in silicon. *Nat. Commun.* **3,** 629 (2012).

40. M. Koike, E. Shikoh, Y. Ando, T. Shinjo, S. Yamada, K. Hamaya & M. Shiraishi. Dynamical Spin Injection into p-Type Germanium at Room Temperature. *Appl. Phys. Express* **6,** 023001 (2013).

41. J.-C. Rojas-Sánchez, M. Cubukcu, A. Jain, C. Vergnaud, C. Portemont, C. Ducruet, A. Barski, A. Marty, L. Vila, J.-P. Attané, E. Augendre, G. Desfonds, S. Gambarelli, H. Jaffrès, J.-M. George & M. Jamet. Spin pumping and inverse spin Hall effect in germanium. *Phys. Rev. B* **88,** 064403 (2013).

42. L. Chen, F. Matsukura & H. Ohno. Direct-current voltages in (Ga,Mn)As structures induced by ferromagnetic resonance. *Nat. Commun.* **4,** 2055 (2013).

43. K. Ando, S. Watanabe, S. Mooser, E. Saitoh & H. Sirringhaus. Solution-processed organic spin–charge converter. *Nat. Mater.* **12,** 622–627 (2013).

44. Y. Tserkovnyak, A. Brataas & G. E. W. Bauer. Enhanced Gilbert Damping in Thin Ferromagnetic Films. *Phys. Rev. Lett.* **88,** 117601 (2002).

45. Y. Tserkovnyak, A. Brataas & G. E. W. Bauer. Spin pumping and magnetization dynamics in metallic multilayers. *Phys. Rev. B* **66,** 224403 (2002).

46. S. Mizukami, Y. Ando & T. Miyazaki. The Study on Ferromagnetic Resonance Linewidth for NM/80NiFe/NM (NM=Cu, Ta, Pd and Pt) Films. *Jpn. J. Appl. Phys.* **40,** 580–585 (2001).

47. S. Mizukami, Y. Ando & T. Miyazaki. Ferromagnetic resonance linewidth for NM/80NiFe/NM films (NM=Cu, Ta, Pd and Pt). *J. Magn. Magn. Mater.* **226-230,** 1640–1642 (2001).

48. S. Mizukami, Y. Ando & T. Miyazaki. Effect of spin diffusion on Gilbert damping for a very thin permalloy layer in Cu/permalloy/Cu/Pt films. *Phys. Rev. B* **66,** 104413 (2002).

49. Y. Ohno, D. K. Young, B. Beschoten, F. Matsukura, H. Ohno & D. D. Awschalom. Electrical spin injection in a ferromagnetic semiconductor heterostructure. *Nature* **402,** 790–792 (1999).

50. B. F. Miao, S. Y. Huang, D. Qu & C. L. Chien. Inverse Spin Hall Effect in a Ferromagnetic Metal. *Phys. Rev. Lett.* **111,** 066602 (2013).

51. A. Tsukahara, Y. Ando, Y. Kitamura, H. Emoto, E. Shikoh, M. P. Delmo, T. Shinjo & M. Shiraishi. Self-induced inverse spin Hall effect in permalloy at room temperature. *Phys. Rev. B* **89,**

235317 (2014).

52. L. Chen, S. Ikeda, F. Matsukura & H. Ohno. DC voltages in Py and Py/Pt under ferromagnetic resonance. *Appl. Phys. Express* **7,** 013002 (2014).

53. C. W. Sandweg, Y. Kajiwara, K. Ando, E. Saitoh & B. Hillebrands. Enhancement of the spin pumping efficiency by spin wave mode selection. *Appl. Phys. Lett.* **97,** 252504 (2010).

54. C. W. Sandweg, Y. Kajiwara, a. V. Chumak, a. a. Serga, V. I. Vasyuchka, M. B. Jungfleisch, E. Saitoh & B. Hillebrands. Spin Pumping by Parametrically Excited Exchange Magnons. *Phys. Rev. Lett.* **106,** 216601 (2011).

55. K. Harii, T. An, Y. Kajiwara, K. Ando, H. Nakayama, T. Yoshino & E. Saitoh. Frequency dependence of spin pumping in Pt/Y3Fe5O12 film. *J. Appl. Phys.* **109,** 116105 (2011).

56. B. Heinrich, C. Burrowes, E. Montoya, B. Kardasz, E. Girt, Y.-Y. Song, Y. Sun & M. Wu. Spin Pumping at the Magnetic Insulator (YIG)/Normal Metal (Au) Interfaces. *Phys. Rev. Lett.* **107,** 066604 (2011).

57. L. H. Vilela-Leão, C. Salvador, A. Azevedo & S. M. Rezende. Unidirectional anisotropy in the spin pumping voltage in yttrium iron garnet/platinum bilayers. *Appl. Phys. Lett.* **99,** 102505 (2011).

58. O. d'Allivy Kelly, A. Anane, R. Bernard, J. Ben Youssef, C. Hahn, A. H. Molpeceres, C. Carrétéro, E. Jacquet, C. Deranlot, P. Bortolotti, R. Lebourgeois, J.-C. Mage, G. de Loubens, O. Klein, V. Cros & A. Fert. Inverse spin Hall effect in nanometer-thick yttrium iron garnet/Pt system. *Appl. Phys. Lett.* **103,** 082408 (2013).

59. A. Kapelrud & A. Brataas. Spin Pumping and Enhanced Gilbert Damping in Thin Magnetic Insulator Films. *Phys. Rev. Lett.* **111,** 097602 (2013).

60. H. Wang, C. Du, P. Chris Hammel & F. Yang. Spin current and inverse spin Hall effect in ferromagnetic metals probed by $Y_3Fe_5O_{12}$-based spin pumping. *Appl. Phys. Lett.* **104,** 3–7 (2014).

61. M. I. Dyakonov & V. I. Perel. Spin Orientation of Electrons Associated with the Interband Absorption of Light in Semiconductors. *Sov. physics, JETP* **33,** 1053–1059 (1971).

62. S. M. Sze & J. C. Irvin. Resistivity, mobility and impurity levels in GaAs, Ge, and Si at 300°K. *Solid. State. Electron.* **11,** 599–602 (1968).

63. K. Morii, T. Iwasaki, R. Nakane, M. Takenaka & S. Takagi. High-Performance GeO2/Ge nMOSFETs With Source/Drain Junctions Formed by Gas-Phase Doping. *IEEE Electron Device*

Lett. **31,** 1092–1094 (2010).

64. G. Feher, D. K. Wilson & E. A. Gere. Electron spin resonance experiments on shallow donors in germanium. *Phys. Rev. Lett.* **3,** 25–28 (1959).

65. D. K. Wilson. Electron spin resonance experiments on shallow donors in germanium. *Phys. Rev.* **134,** A265–A286 (1964).

66. R. E. Pontinen & T. M. Sanders. Electron-Spin-Resonance Experiments on Antimony-Dped Germanium. *Phys. Rev.* **152,** 850–857 (1966).

67. E. Gershenzon. Electron Spin Resonance in As-Doped Ge in a Wide Range of Impurity Concentration. *Phys. Status Solidi* **49,** 411–421 (1972).

68. A. I. Veinger, T. V. Zabrodskii, T. V Tisnek & S. I. Goloshchapov. Electron spin resonance of interacting spins in n-Ge. 1. The spectrum and g factor. *Semiconductors* **41,** 790–798 (2007).

69. A. I. Veinger, T. V. Zabrodskii, T. V Tisnek & S. I. Goloshchapov. Electron spin resonance of interacting spins in n-Ge: II. Change in the width and shape of lines. *Semiconductors* **42,** 1274–1281 (2008).

70. C. Hautmann, B. Surrer & M. Betz. Ultrafast optical orientation and coherent Larmor precession of electron and hole spins in bulk germanium. *Phys. Rev. B* **83,** 161203 (2011).

71. C. Guite & V. Venkataraman. Measurement of Electron Spin Lifetime and Optical Orientation Efficiency in Germanium Using Electrical Detection of Radio Frequency Modulated Spin Polarization. *Phys. Rev. Lett.* **107,** 166603 (2011).

72. E. J. Loren, J. Rioux, C. Lange, J. E. Sipe, H. M. van Driel & A. L. Smirl. Hole spin relaxation and intervalley electron scattering in germanium. *Phys. Rev. B* **84,** 214307 (2011).

73. F. Pezzoli, F. Bottegoni, D. Trivedi, F. Ciccacci, A. Giorgioni, P. Li, S. Cecchi, E. Grilli, Y. Song, M. Guzzi, H. Dery & G. Isella. Optical Spin Injection and Spin Lifetime in Ge Heterostructures. *Phys. Rev. Lett.* **108,** 156603 (2012).

74. Y. Zhou, W. Han, L.-T. Chang, F. Xiu, M. Wang, M. Oehme, I. A. Fischer, J. Schulze, R. K. Kawakami & K. L. Wang. Electrical spin injection and transport in germanium. *Phys. Rev. B* **84,** 125323 (2011).

75. L.-T. Chang, W. Han, Y. Zhou, J. Tang, I. A. Fischer, M. Oehme, J. Schulze, R. K. Kawakami & K. L. Wang. Comparison of spin lifetimes in n -Ge characterized between three-terminal and four-

terminal nonlocal Hanle measurements. *Semicond. Sci. Technol.* **28,** 015018 (2013).

76. K. Kasahara, Y. Fujita, S. Yamada, K. Sawano, M. Miyao & K. Hamaya. Greatly enhanced generation efficiency of pure spin currents in Ge using Heusler compound Co2FeSi electrodes. *Appl. Phys. Express* **7,** 033002 (2014).
77. C. Shen, T. Trypiniotis, K. Y. Lee, S. N. Holmes, R. Mansell, M. Husain, V. Shah, X. V. Li, H. Kurebayashi, I. Farrer, C. H. de Groot, D. R. Leadley, G. Bell, E. H. C. Parker, T. Whall, D. A. Ritchie & C. H. W. Barnes. Spin transport in germanium at room temperature. *Appl. Phys. Lett.* **97,** 162104 (2010).
78. K.-R. Jeon, B.-C. Min, Y.-H. Jo, H.-S. Lee, I.-J. Shin, C.-Y. Park, S.-Y. Park & S.-C. Shin. Electrical spin injection and accumulation in CoFe/MgO/Ge contacts at room temperature. *Phys. Rev. B* **84,** 165315 (2011).
79. A. T. Hanbicki, S.-F. Cheng, R. Goswami, O. M. J. van ‘t Erve & B. T. Jonker. Electrical injection and detection of spin accumulation in Ge at room temperature. *Solid State Commun.* **152,** 244–248 (2012).
80. Y. Aoki, M. Kameno, Y. Ando, E. Shikoh, Y. Suzuki, T. Shinjo, M. Shiraishi, T. Sasaki, T. Oikawa & T. Suzuki. Investigation of the inverted Hanle effect in highly doped Si. *Phys. Rev. B* **86,** 081201 (2012).
81. T. Uemura, K. Kondo, J. Fujisawa, K. Matsuda & M. Yamamoto. Critical effect of spin-dependent transport in a tunnel barrier on enhanced Hanle-type signals observed in three-terminal geometry. *Appl. Phys. Lett.* **101,** 132411 (2012).
82. O. Txoperena, M. Gobbi, A. Bedoya-Pinto, F. Golmar, X. Sun, L. E. Hueso & F. Casanova. How reliable are Hanle measurements in metals in a three-terminal geometry? *Appl. Phys. Lett.* **102,** 192406 (2013).
83. H. N. Tinkey, P. Li & I. Appelbaum. Inelastic electron tunneling spectroscopy of local ‘spin accumulation’ devices. *Appl. Phys. Lett.* **104,** 232410 (2014).
84. A. G. Swartz, S. Harashima, Y. Xie, D. Lu, B. Kim, C. Bell, Y. Hikita & H. Y. Hwang. Spin-dependent transport across Co/LaAlO3/SrTiO3 heterojunctions. *Appl. Phys. Lett.* **105,** 032406 (2014).
85. Y. Song & H. Dery. Magnetic-Field-Modulated Resonant Tunneling in Ferromagnetic-Insulator-

Nonmagnetic Junctions. *Phys. Rev. Lett.* **113,** 047205 (2014).

86. O. Txoperena, Y. Song, L. Qing, M. Gobbi, L. E. Hueso, H. Dery & F. Casanova. Impurity-Assisted Tunneling Magnetoresistance under a Weak Magnetic Field. *Phys. Rev. Lett.* **113,** 146601 (2014).

87. Y. Tserkovnyak, A. Brataas, G. E. W. Bauer & B. I. Halperin. Nonlocal Magnetization Dynamics in Ferromagnetic Hybrid Nanostructures. *Rev. Mod. Phys.* **77,** 1375–1421 (2005).

88. A. Brataas, Y. Tserkovnyak, G. E. W. Bauer & P. J. Kelly. Spin Pumping and Spin Transfer. 1–30 (2011). doi:arXiv:1108.0385v3

89. Z. Tang, E. Shikoh, H. Ago, K. Kawahara, Y. Ando, T. Shinjo & M. Shiraishi. Dynamically generated pure spin current in single-layer graphene. *Phys. Rev. B* **87,** 140401 (2013).

90. S. Watanabe, K. Ando, K. Kang, S. Mooser, Y. Vaynzof, H. Kurebayashi, E. Saitoh & H. Sirringhaus. Polaron spin current transport in organic semiconductors. *Nat. Phys.* **10,** 308–313 (2014).

91. T. Tanaka, H. Kontani, M. Naito, T. Naito, D. S. Hirashima, K. Yamada & J. Inoue. Intrinsic spin Hall effect and orbital Hall effect in 4d and 5d transition metals. *Phys. Rev. B* **77,** 165117 (2008).

92. M. Morota, Y. Niimi, K. Ohnishi, D. H. Wei, T. Tanaka, H. Kontani, T. Kimura & Y. Otani. Indication of intrinsic spin Hall effect in 4d and 5d transition metals. *Phys. Rev. B* **83,** 174405 (2011).

93. D. Choi, Y. Ge, J. S. Harris, J. Cagnon & S. Stemmer. Low surface roughness and threading dislocation density Ge growth on Si (0 0 1). *J. Cryst. Growth* **310,** 4273–4279 (2008).

94. V. A. Shah, A. Dobbie, M. Myronov & D. R. Leadley. Effect of layer thickness on structural quality of Ge epilayers grown directly on Si(001). *Thin Solid Films* **519,** 7911–7917 (2011).

95. Y. Yamamoto, P. Zaumseil, T. Arguirov, M. Kittler & B. Tillack. Low threading dislocation density Ge deposited on Si (100) using RPCVD. *Solid. State. Electron.* **60,** 2–6 (2011).

96. V. Huy Nguyen, A. Dobbie, M. Myronov & D. R. Leadley. High quality relaxed germanium layers grown on (110) and (111) silicon substrates with reduced stacking fault formation. *J. Appl. Phys.* **114,** 154306 (2013).

97. Y. Ishikawa, K. Wada, D. D. Cannon, J. Liu, H. C. Luan & L. C. Kimerling. Strain-induced band gap shrinkage in Ge grown on Si substrate. *Appl. Phys. Lett.* **82,** 2044–2046 (2003).

98. J. M. Hartmann. Reduced pressure–chemical vapor deposition of Ge thick layers on Si(001) for 1.3–1.55-μm photodetection. *J. Appl. Phys.* **95,** 5905 (2004).

99. V. A. Shah, A. Dobbie, M. Myronov & D. R. Leadley. High quality relaxed Ge layers grown directly on a Si(001) substrate. *Solid. State. Electron.* **62,** 189–194 (2011).

100. K. Ando, S. Takahashi, J. Ieda, H. Kurebayashi, T. Trypiniotis, C. H. W. Barnes, S. Maekawa & E. Saitoh. Electrically tunable spin injector free from the impedance mismatch problem. *Nat. Mater.* **10,** 655–659 (2011).

101. C. Kittel. On the Theory of Ferromagnetic Resonance Absorption. *Phys. Rev.* **73,** 155–161 (1948).

102. J. Foros, G. Woltersdorf, B. Heinrich & A. Brataas. Scattering of spin current injected in Pd(001). *J. Appl. Phys.* **97,** 10A714 (2005).

103. W. A. Beck & J. R. Anderson. Determination of electrical transport properties using a novel magnetic field-dependent Hall technique. *J. Appl. Phys.* **62,** 541 (1987).

104. S. Kiatgamolchai, M. Myronov, O. A. Mironov, V. G. Kantser, E. H. C. Parker & T. E. Whall. Mobility spectrum computational analysis using a maximum entropy approach. *Phys. Rev. E* **66,** 036705 (2002).

105. R. J. Elliott. Theory of the effect of spin-orbit coupling on magnetic resonance in some semiconductors. *Phys. Rev.* **96,** 266–279 (1954).

106. Y. Yafet. *Solid State Physics 14*. (Academic, 1963).

107. S. R. Marmion, M. Ali, M. McLaren, D. A. Williams & B. J. Hickey. Temperature dependence of spin Hall magnetoresistance in thin YIG/Pt films. *Phys. Rev. B* **89,** 220404 (2014).

108. R. Ohshima, H. Emoto, T. Shinjo, Y. Ando & M. Shiraishi. Temperature evolution of electromotive force from Pt on yttrium-iron-garnet under ferromagnetic resonance. *J. Appl. Phys.* **117,** 17D136 (2015).

109. S. M. Sze & K. K. Ng. *Physics of Semiconductor Devices*. (John Wiley & Sons, Inc., 2006). doi:10.1002/0470068329

110. B. J. Baliga. *Fundamentals of Power Semiconductor Devices*. (Springer US, 2008). doi:10.1007/978-0-387-47314-7

111. P. Li, Y. Song & H. Dery. Intrinsic spin lifetime of conduction electrons in germanium. *Phys. Rev. B* **86,** 085202 (2012).

112. Y. Song, O. Chalaev & H. Dery. Donor-Driven Spin Relaxation in Multivalley Semiconductors. *Phys. Rev. Lett.* **113,** 167201 (2014).

113. P. Li, J. Li, L. Qing, H. Dery & I. Appelbaum. Anisotropy-Driven Spin Relaxation in Germanium. *Phys. Rev. Lett.* **111,** 257204 (2013).

114. J.-M. Tang, B. T. Collins & M. E. Flatté. Electron spin-phonon interaction symmetries and tunable spin relaxation in silicon and germanium. *Phys. Rev. B* **85,** 045202 (2012).

115. T. Suzuki, T. Sasaki, T. Oikawa, M. Shiraishi, Y. Suzuki & K. Noguchi. Room-Temperature Electron Spin Transport in a Highly Doped Si Channel. *Appl. Phys. Express* **4,** 023003 (2011).

116. K. S. Novoselov, A. K. Geim, S. V. Morozov, D. Jiang, M. I. Katsnelson, I. V. Grigorieva, S. V. Dubonos & A. A. Firsov. Two-dimensional gas of massless Dirac fermions in graphene. *Nature* **438,** 197–200 (2005).

117. N. Tombros, C. Jozsa, M. Popinciuc, H. T. Jonkman & B. J. van Wees. Electronic spin transport and spin precession in single graphene layers at room temperature. *Nature* **448,** 571–574 (2007).

118. W. Han, R. K. Kawakami, M. Gmitra & J. Fabian. Graphene spintronics. *Nat. Nanotechnol.* **9,** 794–807 (2014).

119. W. Han, K. Pi, K. M. McCreary, Y. Li, J. J. I. Wong, A. G. Swartz & R. K. Kawakami. Tunneling Spin Injection into Single Layer Graphene. *Phys. Rev. Lett.* **105,** 167202 (2010).

120. J. C. R. Sánchez, L. Vila, G. Desfonds, S. Gambarelli, J. P. Attané, J. M. De Teresa, C. Magén & A. Fert. Spin-to-charge conversion using Rashba coupling at the interface between non-magnetic materials. *Nat. Commun.* **4,** 2944 (2013).

121. K. Shen, G. Vignale & R. Raimondi. Microscopic Theory of the Inverse Edelstein Effect. *Phys. Rev. Lett.* **112,** 096601 (2014).

122. A. G. Aronov & Y. B. Lyanda-Geller. Nuclear electric resonance and orientation of carrier spins by an electric field. *JETP Lett.* **50,** 431–434 (1989).

123. V. M. Edelstein. Spin polarization of conduction electrons induced by electric current in two-dimensional asymmetric electron systems. *Solid State Commun.* **73,** 233–235 (1990).

124. Y. K. Kato, R. C. Myers, A. C. Gossard & D. D. Awschalom. Current-Induced Spin Polarization in Strained Semiconductors. *Phys. Rev. Lett.* **93,** 176601 (2004).

125. R. Ohshima, A. Sakai, Y. Ando, T. Shinjo, K. Kawahara, H. Ago & M. Shiraishi. Observation of

spin-charge conversion in chemical-vapor-deposition-grown single-layer graphene. *Appl. Phys. Lett.* **105,** 162410 (2014).

126. J. Balakrishnan, G. K. W. Koon, A. Avsar, Y. Ho, J. H. Lee, M. Jaiswal, S.-J. Baeck, J.-H. Ahn, A. Ferreira, M. A. Cazalilla, A. H. C. Neto & B. Özyilmaz. Giant spin Hall effect in graphene grown by chemical vapour deposition. *Nat. Commun.* **5,** 4748 (2014).
127. S. Dushenko, M. Koike, Y. Ando, T. Shinjo, M. Myronov & M. Shiraishi. Experimental demonstration of room-temperature spin transport in n-type Germanium epilayers. *Phys. Rev. Lett.* **114,** 196602 (2015).
128. F. S. M. Guimaraes, A. T. Costa, R. B. Muniz & M. S. Ferreira. Graphene-based spin-pumping transistor. *Phys. Rev. B* **81,** 233402 (2010).
129. H. Ago, K. Kawahara, Y. Ogawa, S. Tanoue, M. A. Bissett, M. Tsuji, H. Sakaguchi, R. J. Koch, F. Fromm, T. Seyller, K. Komatsu & K. Tsukagoshi. Epitaxial Growth and Electronic Properties of Large Hexagonal Graphene Domains on Cu(111) Thin Film. *Appl. Phys. Express* **6,** 075101 (2013).
130. S. Dushenko, Y. Higuchi, Y. Ando, T. Shinjo & M. Shiraishi. Ferromagnetic resonance and spin pumping efficiency for inverse spin-Hall effect normalization in yttrium-iron-garnet-based systems. *Appl. Phys. Express* **8,** 103002 (2015).
131. J. Barak & U. Lachish. Study of the excitation of magnetostatic modes in yttrium-iron-garnet films by a microstrip line. *J. Appl. Phys.* **65,** 1652–1658 (1989).
132. I. Laulicht, J. T. Suss & J. Barak. The temperature dependence of the ferromagnetic and paramagnetic resonance spectra in thin yttrium-iron-garnet films. *J. Appl. Phys.* **70,** 2251–2258 (1991).
133. E. E. Anderson. Molecular Field Model and the Magnetization of YIG. *Phys. Rev.* **134,** A1581–A1585 (1964).
134. J. Lustikova, Y. Shiomi, Z. Qiu, T. Kikkawa, R. Iguchi, K. Uchida & E. Saitoh. Spin current generation from sputtered $Y_3Fe_5O_{12}$ films. *J. Appl. Phys.* **116,** 153902 (2014).
135. Z. Wang, C. Tang, R. Sachs, Y. Barlas & J. Shi. Proximity-Induced Ferromagnetism in Graphene Revealed by the Anomalous Hall Effect. *Phys. Rev. Lett.* **114,** 016603 (2015).
136. K. Motobayashi, K. Minami, N. Nishi, T. Sakka & M. Osawa. Hysteresis of potential-dependent

changes in ion density and structure of an ionic liquid on a gold electrode: In situ observation by surface-enhanced infrared absorption spectroscopy. *J. Phys. Chem. Lett.* **4,** 3110–3114 (2013).

137. A. Uysal, H. Zhou, G. Feng, S. S. Lee, S. Li, P. Fenter, P. T. Cummings, P. F. Fulvio, S. Dai, J. K. McDonough & Y. Gogotsi. Structural origins of potential dependent hysteresis at the electrified graphene/ionic liquid interface. *J. Phys. Chem. C* **118,** 569–574 (2014).

138. T. Banerjee, W. G. van der Wiel & R. Jansen. Spin injection and perpendicular spin transport in graphite nanostructures. *Phys. Rev. B* **81,** 214409 (2010).

139. Y. Kajiwara, K. Harii, S. Takahashi, J. Ohe, K. Uchida, M. Mizuguchi, H. Umezawa, H. Kawai, K. Ando, K. Takanashi, S. Maekawa & E. Saitoh. Transmission of electrical signals by spin-wave interconversion in a magnetic insulator. *Nature* **464,** 262–266 (2010).

140. D. Huertas-Hernando, F. Guinea & A. Brataas. Spin-orbit coupling in curved graphene, fullerenes, nanotubes, and nanotube caps. *Phys. Rev. B* **74,** 155426 (2006).

141. H. Min, J. E. Hill, N. A. Sinitsyn, B. R. Sahu, L. Kleinman & A. H. MacDonald. Intrinsic and Rashba spin-orbit interactions in graphene sheets. *Phys. Rev. B* **74,** 165310 (2006).

142. A. Avsar, J. Y. Tan, T. Taychatanapat, J. Balakrishnan, G. K. W. Koon, Y. Yeo, J. Lahiri, A. Carvalho, A. S. Rodin, E. C. T. O’Farrell, G. Eda, A. H. Castro Neto & B. Özyilmaz. Spin–orbit proximity effect in graphene. *Nat. Commun.* **5,** 4875 (2014).

143. C. L. Kane & E. J. Mele. Quantum Spin Hall Effect in Graphene. *Phys. Rev. Lett.* **95,** 226801 (2005).

144. M. Gmitra, S. Konschuh, C. Ertler, C. Ambrosch-Draxl & J. Fabian. Band-structure topologies of graphene: Spin-orbit coupling effects from first principles. *Phys. Rev. B* **80,** 235431 (2009).

145. S. Datta & B. Das. Electronic analog of the electro-optic modulator. *Appl. Phys. Lett.* **56,** 665–667 (1990).

146. J. Nitta, T. Akazaki, H. Takayanagi & T. Enoki. Gate Control of Spin-Orbit Interaction in an Inverted In0.53Ga0.47As/In0.52Al0.48As Heterostructure. *Phys. Rev. Lett.* **78,** 1335–1338 (1997).

147. W. Han & R. K. Kawakami. Spin Relaxation in Single-Layer and Bilayer Graphene. *Phys. Rev. Lett.* **107,** 047207 (2011).

148. D. Huertas-Hernando, F. Guinea & A. Brataas. Spin-Orbit-Mediated Spin Relaxation in Graphene. *Phys. Rev. Lett.* **103,** 146801 (2009).

149. H. Ochoa, A. H. Castro Neto & F. Guinea. Elliot-Yafet Mechanism in Graphene. *Phys. Rev. Lett.* **108,** 206808 (2012).

150. A. Ferreira, T. G. Rappoport, M. A. Cazalilla & A. H. Castro Neto. Extrinsic Spin Hall Effect Induced by Resonant Skew Scattering in Graphene. *Phys. Rev. Lett.* **112,** 066601 (2014).

151. J. C. Boettger & S. B. Trickey. First-principles calculation of the spin-orbit splitting in graphene. *Phys. Rev. B* **75,** 121402 (2007).

152. E. Shikoh, K. Ando, K. Kubo, E. Saitoh, T. Shinjo & M. Shiraishi. Spin-Pump-Induced Spin Transport in p-Type Si at Room Temperature. *Phys. Rev. Lett.* **110,** 127201 (2013).

153. Z. Qiu, T. An, K. Uchida, D. Hou, Y. Shiomi, Y. Fujikawa & E. Saitoh. Experimental investigation of spin Hall effect in indium tin oxide thin film. *Appl. Phys. Lett.* **103,** 2013–2016 (2013).

154. M. Haidar, M. Ranjbar, M. Balinsky, R. K. Dumas, S. Khartsev & J. Åkerman. Thickness- and temperature-dependent magnetodynamic properties of yttrium iron garnet thin films. *J. Appl. Phys.* **117,** 17D119 (2015).

155. R. W. Damon & J. R. Eshbach. Magnetostatic modes of a ferromagnet slab. *J. Phys. Chem. Solids* **19,** 308–320 (1961).

156. H. Suhl. The theory of ferromagnetic resonance at high signal powers. *Physic. Chem. Solids* **1,** 209–227 (1957).

List of publications

5.1 Publications related to the thesis

5.1.1 Papers in the peer-reviewed journals

[1] **S. Dushenko**, M. Koike, Y. Ando, T. Shinjo, M. Myronov, and M. Shiraishi, Experimental Demonstration of Room-Temperature Spin Transport in n-Type Germanium Epilayers, Phys. Rev. Lett. **114**, 196602 (2015).

[2] **S. Dushenko**, Y. Higuchi, Y. Ando, T. Shinjo, and M. Shiraishi, Ferromagnetic resonance and spin pumping efficiency for inverse spin-Hall effect normalization in yttrium-iron-garnet-based systems, Appl. Phys. Express **8**, 103002 (2015).

[3] **S. Dushenko**, H. Ago, K. Kawahara, T. Tsuda, S. Kuwabata, T. Takenobu, T. Shinjo, Y. Ando, and M. Shiraishi, Gate-tunable spin-charge conversion and a role of spin-orbit interaction in graphene, Phys. Rev Lett, submitted.

5.1.2 Abstracts at the international conferences

[A1] **S. Dushenko**, M. Koike, Y. Ando, M. Myronov, and M. Shiraishi, Demonstration of spin transport in n-type Germanium epilayers at room temperature, Book of Abstracts 59th Annual Conference on Magnetism and Magnetic Materials, FB-05, p.566, Honolulu, Hawaii, USA, November 3-7 2014.

[A2] **S. Dushenko**, M. Koike, Y. Ando, T. Shinjo, M. Myronov, and M. Shiraishi, Experimental demonstration of Elliott-Yafet spin relaxation mechanism and room-temperature spin transport in highly-doped n-type Ge epilayers, Book of Abstracts 20th International Conference on Magnetism, Mo.D-P04, p.794, Barcelona, Spain, July 5-10 2015.

5.1.3 Abstracts at the domestic conferences

[A3] **S. Dushenko**, E. Shikoh, Y. Ando, T. Shinjo, and M. Shiraishi, Estimation of the spin diffusion length in p-type Si from the length dependence of lateral spin channel, The 74th Japan Society of Applied Physics (JSAP) Autumn Meeting, Kyoto, Japan, 16-20 September 2013.

[A4] **S. Dushenko**, E. Shikoh, Y. Ando, T. Shinjo, and M. Shiraishi, Spin diffusion length evaluation using channel length in lateral spin transport experiments, The 18th Symposium on the Physics and

Applications of Spin-related Phenomena in Semiconductors (PASPS), Program and Abstracts, p.37, Osaka University, Japan, 9-10 December 2013.

[A5] **S. Dushenko**, M. Koike, Y. Ando, M. Myronov, and M. Shiraishi, Spin transport in n-type Germanium epilayers at room temperature, The 75th Japan Society of Applied Physics (JSAP) Autumn Meeting, Sapporo, Japan, 17-20 September 2014.

[A6] **S. Dushenko**, M. Koike, Y. Ando, T. Shinjo, M. Myronov, and M. Shiraishi, An experimental demonstration of room-temperature spin transport and Elliott-Yafet spin relaxation mechanism in n-type Germanium epilayers, Nano Spin Conversion meeting, Kyoto University ROHM Plaza (Katsura Campus), Kyoto, Japan, 3-4 March 2015.

[A7] **S. Dushenko**, M. Koike, Y. Ando, T. Shinjo, M. Myronov, and M. Shiraishi, Spin transport at room temperature and spin relaxation mechanism in Germanium, Kansai Area Spintronics Joint Seminar, P26, Osaka, Japan, 1 September 2015.

(Original title in Japanese: **S. Dushenko**, M. Koike, Y. Ando, T. Shinjo, M. Myronov, and M. Shiraishi, Spin transport at room temperature and spin relaxation mechanism in Germanium, 関西地区スピントロニク研究室合同ゼミナール, P26, Osaka, Japan, 1 September 2015)

[A8] **S. Dushenko**, M. Koike, Y. Ando, T. Shinjo, M. Myronov, and M. Shiraishi, Experimental determination of the spin relaxation mechanism in highly-doped n-type germanium epilayers, The 76th Japan Society of Applied Physics (JSAP) Autumn Meeting, 14p-2J-14, Nagoya, Japan, 13-16 September 2015.

[A9] **S. Dushenko**, H. Ago, K. Kawahara, T. Tsuda, S. Kuwabata, T. Takenobu, T. Shinjo, Y. Ando, M. Shiraishi, Spin-charge conversion modulation via ionic liquid gate in a single-layer graphene, The 76th Japan Society of Applied Physics (JSAP) Autumn Meeting, 14p-2J-15, Nagoya, Japan, 13-16 September 2015.

[A10] **S. Dushenko**, H. Ago, K. Kawahara, T. Tsuda, S. Kuwabata, T. Takenobu, T. Shinjo, Y. Ando, M. Shiraishi, Gate tunable spin-charge conversion in a single-layer graphene, The Physical Society of Japan (JPS) 2015 Autumn Meeting, 17pCG-3, Osaka, Japan, 16-19 September 2015.

[A11] **S. Dushenko**, M. Koike, Y. Ando, T. Shinjo, M. Myronov, and M. Shiraishi, Spin relaxation mechanism in n-type Germanium, The Physical Society of Japan (JPS) 2015 Autumn Meeting, 17pCG-4, Osaka, Japan, 16-19 September 2015.

5.2 Other publications

5.2.1 Papers in the peer-reviewed journals

[4] I.O. Dzhun, **S.A. Dushenko**, N.G. Chechenin, E.A. Konstantinova, Temperature dependence of exchange bias in Co/FeMn-structure induced by heating and cooling in magnetic field, J. Phys. Conf. Ser. **303**, 012103 (2011).

[5] I.O. Dzhun, **S.A. Dushenko**, N.G. Chechenin, E.A. Konstantinova, The dependence of magnetic properties of Co/FeMn bilayer structure on the magnitude of magnetic field applied during the layer deposition, J. Phys. Conf. Ser. **303**, 012104 (2011).

[6] I.O. Dzhun, N.G. Chechenin, **S.A. Dushenko** and E.A. Konstantinova, Exchange bias in Co/FeMn and Co/IrMn structures induced by deposition in presence of magnetic field, Solid State Phenom. **190**, 93 (2012).

[7] N.G. Chechenin, I.O. Dzhun, **S.A. Dushenko** and E.A. Konstantinova, Exchange Bias Induced in Polycrystalline Co/FeMn-Structures by Magnetic Field Cooling, Solid State Phenom. **190**, 81 (2012).

[8] N.G. Chechenin, P.N. Chernykh, **S.A. Dushenko**, I.O. Dzhun, A.Y. Goikhman, V.V. Rodionova, Asymmetry of Magnetization Reversal of Pinned Layer in NiFe/Cu/NiFe/IrMn Spin-Valve Structure, J. Supercond. Nov. Magn. **27**, 1547 (2014).

5.2.2 Abstracts at the international conferences

[A12] I.O. Dzhun, **S.A. Dushenko**, N.G. Chechenin, E.A. Konstantinova, Temperature dependence of exchange bias in Co/FeMn-structure induced by heating and cooling in magnetic field, Joint European Magnetic Symposia (JEMS) 2010 Programme Abstracts, p.190, Krakow, Poland, 23-28 August 2010.

[A13] I.O. Dzhun, **S.A. Dushenko**, N.G. Chechenin, E.A. Konstantinova, Dependence of magnetic properties of Co/FeMn structure on magnetic field applied during the deposition, Joint European Magnetic Symposia (JEMS) 2010 Programme Abstracts, p.191, Krakow, Poland, 23-28 August 2010.

[A14] N.G. Chechenin, I.O. Dzhun, **S.A. Dushenko**, E.A. Konstantinova, Exchange bias induced in polycrystalline Co/FeMn-structures by magnetic field cooling, Book of Abstracts Moscow International Symposium on Magnetism (MISM), p.143, Moscow, Russian Federation, 21-25 August 2011.

[A15] I.O. Dzhun, N.G. Chechenin, **S.A. Dushenko**, E.A. Konstantinova, Exchange bias in Co/IrMn and NiFe/IrMn structures induced by deposition in presence of magnetic field, Book of Abstracts Moscow International Symposium on Magnetism (MISM), p.672, Moscow, Russian Federation, 21-25 August 2011.

[A16] **S.A. Dushenko**, N.G. Chechenin, P.N. Chernykh, I.O. Dzhun, Giant magnetoresistance in NiFe/IrMn/Cu/NiFe-based spin-valve structures, Book of Abstracts Moscow International Symposium on Magnetism (MISM), p.673, Moscow, Russian Federation, 21-25 August 2011.

[A17] S. Medvedeva, I. Dzhun, **S. Dushenko**, Study of angular dependence of coercivity force and exchange bias field in Co/IrMn, FeNi/IrMn and NiFe/Cu/NiFe/IrMn structures, Book of abstracts International Baltic School on solid state and magnetism phenomena, p.32, Kaliningrad, Russian Federation, 11-18 August 2012.

[A18] **S. Dushenko**, N. Chechenin, S. Medvedeva, A. Goikhman, V. Rodionova, Spacer thickness effects on GMR, exchange bias and coercivity in spin-valve structures, Book of Abstracts Joint European Magnetic Symposia (JEMS) 2012, p.86, Parma, Italy, 9-14 September 2012.

5.2.3 Abstracts at the domestic conferences

[A19] **S.A. Dushenko**, I.O. Dzhun, Uniaxial and unidirectional anisotropy in system FeMn/Co, Materials of the XVII International conference of students and young scientists Lomonosov, Moscow, Russian Federation, 12-15 April 2010.

(Original title in Russian: **С.А. Душенко**, И.О. Джунь, Одноосная и однонаправленная анизотропия в системе FeMn/Co, Материалы докладов XVII Международной конференции студентов, аспирантов и молодых ученых Ломоносов, Москва, Российская Федерация, 12-15 апреля 2010)

[A20] I.O. Dzhun, **S.A. Dushenko**, N.G. Chechenin, Features of the exchange bias effect on the ferromagnetic/antiferromagnetic interface, Scientific conference Lomonosov Readings, Moscow, Russian Federation, April 2010.

(Original title in Russian: И.О. Джунь, **С.А. Душенко**, Н.Г. Чеченин, Особенности проявления эффекта обменного смещения на интерфейсе ферромагнетик/антиферромагнетик, Научная конференция Ломоносовские чтения, Москва, Российская Федерация, апрель 2010)

[A21] I.O. Dzhun, **S.A. Dushenko**, N.G. Chechenin, Temperature dependence of exchange bias in system Co/FeMn induced by thermal annealing followed by cooling in presence of magnetic field, Abstracts of the School of young scientists on the physics of nanostructured and crystalline materials, p.77, Nizhny Novgorod, Russian Federation, 21-23 October 2010.

(Original title in Russian: И.О. Джунь, **С.А. Душенко**, Н.Г. Чеченин, Температурная зависимость обменного смещения в структуре Co/FeMn, индуцированного методом термического отжига с последующим остыванием в присутствии магнитного поля, Конспекты лекций и тезисы докладов Школы молодых ученых по физике наноструктурированных и кристаллических материалов, с.77, Нижний Новгород, Российская Федерация, 21-23 октября 2010)

[A22] I.O. Dzhun, **S.A. Dushenko**, N.G. Chechenin, Dependence of the magnetic properties of bilayer structures of Co/FeMn from the magnetic field amplitude applied during the deposition, Abstracts of the School of Young Scientists on the Physics of nanostructured and crystalline materials, p.81, Nizhny Novgorod, Russian Federation, 21-23 October 2010.

(Original title in Russian: И.О. Джунь, **С.А. Душенко**, Н.Г. Чеченин, Зависимость магнитных свойств двуслойных структур Co/FeMn от величины магнитного поля, приложенного при осаждении, Конспекты лекций и тезисы докладов Школы молодых ученых по физике наноструктурированных и кристаллических материалов, с.81, Нижний Новгород, Российская Федерация, 21-23 октября 2010)

[A23] **S.A. Dushenko**, I.O. Dzhun, Exchange bias in system FeMn/Co induced by annealing in presence of magnetic field, Materials of the XVIII International conference of students and young scientists Lomonosov, Moscow, Russian Federation, 11-15 April 2011.

(Original title in Russian: **С.А. Душенко**, И.О. Джунь, Обменное смещение в системе FeMn/Co, наведённое при помощи отжига в магнитном поле, Материалы докладов XVIII Международной конференции студентов, аспирантов и молодых ученых Ломоносов, Москва, Российская Федерация, 11-15 апреля 2011)

[A24] I.O. Dzhun, **S.A. Dushenko**, N.G. Chechenin, Exchange bias in Co/IrMn and NiFe/IrMn structures induced by deposition in presence of magnetic field, Abstracts of the School of young scientists on the physics of nanostructured and crystalline materials, p.90, Nizhny Novgorod, Russian Federation, 19-21 May 2011.

(Original title in Russian: И.О. Джунь, **С.А. Душенко**, Н.Г. Чеченин, Обменное смещение в структурах Co/IrMn и NiFe/IrMn, наведённое методом осаждения в присутствии магнитного поля, Конспекты лекций и тезисы докладов Школы молодых ученых по физике наноструктурированных и кристаллических материалов, с.90, Нижний Новгород, Российская Федерация, 19-21 мая 2011)

[A25] **S.A. Dushenko**, I.O. Dzhun, N.G. Chechenin, P.N. Chernykh, The study of the effect of giant magnetoresistance in spin-valve structures with an active region NiFe/IrMn/Cu/NiFe, Abstracts of the School of young scientists on the physics of nanostructured and crystalline materials, p.96, Nizhny Novgorod, Russian Federation, 19-21 May 2011.

(Original title in Russian: **С.А. Душенко**, И.О. Джунь, Н.Г. Чеченин, П.Н. Черных, Исследование эффекта гигантского магнетосопротивления в спин-диодных структурах с активной областью NiFe/IrMn/Cu/NiFe, Конспекты лекций и тезисы докладов Школы молодых ученых по физике наноструктурированных и кристаллических материалов, с.96, Нижний Новгород, Российская Федерация, 19-21 мая 2011)

[A26] I.O. Dzhun, **S.A. Dushenko**, N.G. Chechenin, Anisotropy of the exchange bias in thin polycrystalline ferromagnetic/antiferromagnetic films, Scientific conference Lomonosov Readings, Moscow, Russian Federation, November 2011.

(Original title in Russian: И.О. Джунь, **С.А. Душенко**, Н.Г. Чеченин, Анизотропия обменного взаимодействия в тонких поликристаллических пленках типа ферромагнетик/антиферромагнетик, Научная конференция Ломоносовские чтения, Москва, Российская Федерация, ноябрь 2011)

[A27] **S.A. Dushenko**, I.O. Dzhun, Giant magnetoresistance in NiFe/Cu/NiFe/IrMn-based structures with different thicknesses of the Cu spacer layer, Materials of the XIX International conference of students and young scientists Lomonosov, Moscow, Russian Federation, 9-13 April 2012.

(Original title in Russian: **С.А. Душенко**, И.О. Джунь, Эффект гигантского магнитосопротивления в системе NiFe/Cu/NiFe/IrMn с изменяющейся толщиной разделительного медного слоя, Материалы докладов XIX Международной конференции студентов, аспирантов и молодых ученых Ломоносов, Москва, Российская Федерация, 9-13 апреля 2012)

[A29] **S.A. Dushenko**, P.N. Chernykh, N.G. Chechenin, Effect of the Giant Magnetoresistance in system NiFe/Cu/NiFe/IrMn, Scientific conference Lomonosov Readings, Moscow, Russian Federation, April 2012.

(Original title in Russian: **С.А. Душенко**, П.Н. Черных, Н.Г. Чеченин, Эффект гигантского магнитосопротивления в системе NiFe/Cu/NiFe/IrMn, Научная конференция Ломоносовские чтения, Москва, Российская Федерация, апрель 2012)

[A30] E. Shikoh, K. Kubo, **S. Dushenko**, Y. Ando, T. Shinjo, M. Shiraishi, Temperature dependence of the spin-coherence in p-type silicon, The 37th Annual Conference on MAGNETICS in Japan, Sapporo, Japan, 3-6 September 2013.

[A31] M. Shiraishi, Yu. Ando, G. Eguchi, **S. Dushenko**, H. Emoto, T. Shinjo, Yo. Ando, A. Kimura, E. Shikoh, T. Uemura, Electrical Spin Detection in Semiconductors, Semimetals and Topological Insulators, Nano Spin Conversion meeting, O-4, Kyoto University ROHM Plaza Katsura Campus, Kyoto, Japan, 3-4 March 2015.

(Original title in Japanese: 白石　誠司、安藤　裕一郎、江口　学、**Dushenko Sergey**、江本　裕行、新庄　輝也、安藤　陽一、木村　昭夫、仕幸　英治、植村　哲也，半導体・半金属・トポロジカル絶縁体における電気的スピン検出，Nano Spin Conversion meeting, O-4, Kyoto University ROHM Plaza Katsura Campus, Kyoto, Japan, 3-4 March 2015)

[A32] E. Shigematsu, Y. Ando, R. Ohshima, **S. Dushenko**, Y. Higuchi, H.J. von Bardeleben, M. Shiraishi, Suppression of spin pumping efficiency at low temperature in Pt/YIG thin films, The 76th Japan Society of Applied Physics (JSAP) Autumn Meeting, 14p-2J-16, Nagoya, Japan, 13-16 September 2015.

[A33] E. Shigematsu, H. Nagano, **S. Dushenko**, Y. Ando, T. Tsuda, S. Kuwabata, T. Takenobu, T. Tanaka, H. Kataura, T. Shinjo, and M. Shiraishi, Spin to charge conversion in metal/semiconductor single-walled carbon nanotubes, The 20th Symposium on the Physics and Applications of Spin-related Phenomena in Semiconductors (PASPS), F-1, Sendai, Japan, 3-4 December 2015.

[A 34] M. Matsushima, **S. Dushenko**, R. Ohshima, Y. Ando, T. Shinjo, and M. Shiraishi, Observation of inverse Rashba-Edelstein effect in Bi/Ag and Ag/Bi interfaces with ferromagnetic insulator, Nano Spin Conversion meeting, PS-13, Tohoku University Advanced Institute for Materials Research, Sendai, Japan, 7-8 January 2016.

[A 35] E. Shigematsu, H. Nagano, **S. Dushenko**, Y. Ando, T. Tsuda, S. Kuwabata, T. Takenobu, T. Tanaka, H. Kataura, T. Shinjo, and M. Shiraishi, Spin to charge conversion in metallic and semiconducting single-walled carbon nanotubes, Nano Spin Conversion meeting, PS-11, Tohoku University Advanced Institute for Materials Research, Sendai, Japan, 7-8 January 2016.

Acknowledgment

I’m deeply grateful to Prof. M. Shiraishi for accepting me as a doctoral course student, and for all his guidance, support and kindness. I am lucky to have supervisor who is not only a great scientist, but also is a wonderful person. While, probably, falling in the same trap of the self-deception, as did character of Robert Frost’s famous poem,—I do not regret the roads not taken and I enjoyed the chosen path. Study in Japan was my dream and I’m happy person to live through this dream.

I deeply thank Ministry of Education, Culture, Sports, Science and Technology of Japan and Embassy of Japan in Moscow for choosing me for Japanese Government Scholarship (MONBUKAGAKUSHO: MEXT). Without this scholarship my doctoral study in Japan would be impossible.

I’m grateful to Prof. Hamaya for accepting me as a member of his laboratory and his kind help during preparation of doctoral dissertation.

I thank Prof. Y. Ando for his kind support and insightful discussions. Also, I thank staff and students of Shiraishi-laboratory for their help and delightful time spent together during my doctoral course study.

I deeply thank Prof. H. Ago and K. Kawahara for providing single-layer graphene, Dr. M. Myronov for providing Si/Ge substrates, Y. Higuchi for providing 40 nm-thick yttrium-iron-garnet, Prof. T. Tsuda and Prof. S. Kuwabata for providing ionic liquid.

I’m grateful to Marubun Research Promotion Foundation and NEC C&C Foundation for travel grants that allowed me to present my research at international conferences.

Research presented in this dissertation was supported in part by MEXT (Innovative Area “Nano Spin Conversion Science” KAKENHI No. 26103003), Grant-in-Aid for Challenging Exploratory Research (No.25630148), Research Grant from Izumi Science and Technology Foundation, PRESTO-JST, EPSRC-funded “Spintronic device physics in Si/Ge Heterostructures” EP/J003263/1 and “Platform Grant” EP/J001074/1 projects.